Spring 2021

Thermophysical properties of nominally phase pure boride ceramics

Austin D. Stanfield

Department: Materials Science and Engineering

THERMOPHYSICAL PROPERTIES OF NOMINALLY PHASE PURE

BORIDE CERAMICS

by

AUSTIN DAVID STANFIELD

A DISSERTATION

Presented to the Graduate Faculty of the

MISSOURI UNIVERSITY OF SCIENCE AND TECHNOLOGY

In Partial Fulfillment of the Requirements for the Degree

DOCTOR OF PHILOSOPHY

in

MATERIALS SCIENCE AND ENGINEERING

2021

Approved by:

William Fahrenholtz, Advisor
Gregory Hilmas
Wayne Huebner
David Lipke
Yew San Hor

PUBLICATION DISSERTATION OPTION

This dissertation consists of the following four articles, formatted in the style used by the Missouri University of Science and Technology:

Effects of Ti, Y and Hf Adddditions on the Thermal Properties of ZrB_2, found on pages 23-41, has been published in the *Journal of the European Ceramic Society*.

Measurement of the Melting Temperature of ZrB_2 as Determined by Laser Heating and Spectrometric Analysis, found on pages 42-64, has been accepted for publication in the *Journal of the American Ceramic Society*.

Final Stage Densification Kinetics of Direct Current Sintered ZrB_2, found on pages 65-83, has been submitted to the *Journal of the American Ceramic Society*.

Yttrium Solubility in High Entropy Boride Ceramics, found on pages 84-101, has been submitted to the *Journal of the European Ceramic Society*.

ABSTRACT

This research focusses on the thermophysical properties of nominally phase pure boride ceramics. As interest in ultra high temperature ceramics increases due to a renewed interest in hypersonic flight vehicles and with the expanding materials design space accompanying interest in high entropy materials, it is imperative to understand the intrinsic properties of boride ceramics. By reducing Hf content in ZrB_2 from the natural abundance, ~1.75 at% in this case, to ~100 ppm, thermal conductivity increased from 88 W/m•K to 141 W/m•K. Removal of Hf allowed the thermal conductivity of ZrB_2 with small transition metal solute additions to be measured without being masked by Hf impurity effects. Additions of Ti and Y reduced thermal conductivity by 20% and 30% respectively. The melting temperatures of two different types of ZrB_2 were also studied. A commercially available grade of ZrB_2 (~1.75 at% Hf) had a melting temperature of 3280°C while a low Hf (100 ppm) ZrB_2 had a melting temperature of 3273°C. The kinetics of the final stage of densification was also studied for nominally phase pure ZrB_2. Dislocation motion with an activation energy of 162 kJ/mol was determined to be the dominant mechanism in the absence of competing mechanisms such as grain pinning or solute drag caused by secondary phases and impurity soute atoms. The effect of configurational entropy on the solubility of yttrium in high entropy borides was investigated. No significant difference in yttrium solubility was found between nominally pure ZrB_2 and a four component high entropy boride $(Ti,Zr,Nb,Hf)B_2$. Mitigation of impurity atoms and secondary phases minimized extrinsic effect and elucidated intrinsic properties of boride ceramics.

ACKNOWLEDGMENTS

This work, of course, was not possible without the help and support of many people. I would like to first thank my advisor Dr. Bill Fahrenholtz for his guidance, patience, and wisdom. Much of my growth as a scientist and technical communicator is owed to Bill. I would also thank my co-advisor Dr. Greg Hilmas to whom I credit much of my growth in the past 8 years as an engineer. This work would not be possible without funding and support from the Office of Naval Research and the National Science Foundation. Specifically, I must thank Dr. Eric Wuchina from ONR for giving me so many opportunities to both present my work to and network with the materials community at so many conferences. I cannot thank Dr. Jeremy Watts enough for all that he has taught me about furnaces, electricity, hydraulics, and machining, but also for letting me steal his electricity and shop space. I want to thank the general MSE graduate and undergraduate population for making the department as supportive as it is. Special thanks is due to Teneke Hill, Denise Eddings, Jennifer Pratt, Patty Smith, Dr. Eric Bohannan, Dr. Clarissa Wisner, and the McNutt 307 group.

I am eternally grateful to my parents Heidi and David for fostering my curiosity from a young age and allowing me to grow and learn by making mistakes. I cannot thank my sister, Emma, enough for all the love and support she has given me but also for showing me what hard work and perseverance really look like.

Most importantly, none of this would have been possible without the eternal support, patience, and love of my wife, Anna.

TABLE OF CONTENTS

LIST OF ILLUSTRATIONS

PAPER II

PAPER III

PAPER IV

LIST OF TABLES

1. INTRODUCTION

Zirconium diboride (ZrB_2) is classified as an ultra-high temperature ceramic (UHTC) due to its melting temperature of 3250°C making it a candidate material for extreme environment applications (1–3). Particularly, high thermal conductivity (up to ~141 W/m•K) and elevated temperature strength (~200 MPa at 2300°C) make ZrB_2 a candidate material for hypersonic wing leading edges (4–6). However, other properties such as hardness (>30 GPa) make ZrB_2 a candidate material for high speed cutting tools and wear surface coatings (7,8). With a low electrical resistivity of 6 μΩ•cm, zirconium diboride has also been considered for high temperature electrodes (9,10).

Despite extensive studies dating back to the 1960s citing this UHTC as a candidate material for extreme environment applications, ZrB_2 is not widely used (2,11,12). One explanation for this is a disparity in material property data reported in literature. For example, ZrB_2 is considered a good thermal conductor, but room temperature values of thermal conductivity range from 55-141 W/m•K (4,13). Recent work has provided evidence that this range in property data can be traced to impurities including secondary phases, such as oxides and carbides, or solute atoms, such as W, Fe, or Hf (4,14–17). In some cases, these impurities have a drastic effect on thermal properties such as 3 at% W in ZrB_2 decreasing thermal conductivity by 50% as reported by McClane (16). However, other cases no measurable effect (such as 3 at% Ti or Y in ZrB_2) (16). This seems counter-intuitive that some additions can be so detrimental while other have no effect.

Hf is an impurity of particular interest to applications in the nuclear industry. Metallic zirconium is widely used in nuclear applications due to its low neutron absorption cross section (0.185 b), but is unusable unless stripped of its natural abundance of Hf (1-3 wt%) due to the high neutron absorption cross section of Hf (104 b) (18). Refining Zr to the required purity (<100 ppm Hf) involves a toxic and costly process which simply isn't necessary for most Zr applications (19). Lonergan studied the effect of Hf removal from ZrB_2 on thermal properties of zirconium diboride and reported an increase of 40% in the thermal conductivity by utilizing reactor grade Zr source powder(4). However, this effect on other properties has not been quantified.

While McClane's work focused on pinpointing the solute atoms that most affect thermal properties of ZrB_2 and the underlying causes of that effect, his work also provided a foundation for tailoring thermal properties of transition metal diborides through solids solutions of borides. Soon after a new class of UHTCs was introduced as high entropy borides (as well as high entropy oxides and carbides, and preceded by high entropy alloys). High entropy boride are substitutional solid solutions of the diborides that have increase configurational entropy and, potentially, increased thermal and thermodynamic stability through entropy stabilization (20,21). While the initial study was successful in synthesizing 6 single phase 5-component borides, it also produced a failed composition containing two distinct diboride phases with the AlB_2 structure. In addition, all of their materials contained substantial contents of secondary phases, which affected the compositions and properties of the constituent phases. As more studies focus on high entropy materials, no work to date has studied why certain species tend to phase separate in high entropy borides when they are predicted to remain in solution.

The focus of this dissertation was to investigate the thermophysical properties of nominally phase pure boride ceramics. Primarily, this work focusses on zirconium diboride and how utilizing reactor grade Zr sources in the synthesis of high purity ZrB_2 affects properties such as thermal conductivity and melting temperature. Synthesis of high purity, single phase ZrB_2 also allowed the intrinsic densification kinetics in the final stage of sintering to be studied without extrinsic effects such as grain pinning or solute drag masking the dominant mechanisms. Finally, high purity raw materials were used to synthesize single phase, nominally phase pure high entropy borides that were used to investigate the effect of entropy stabilization on the solubility of yttrium in boride ceramics.

With these considerations, this work has been guided by four principle questions:

- Does the presence of other transition metal additions affect the thermal properties of nominally phase pure ZrB_2?
- What is the melting temperature of high purity ZrB_2?
- What is the mechanism of final stage sintering in phase pure ZrB_2?
- How does entropy stabilization affect solubility of yttrium in boride ceramics?

Knowledge of the intrinsic thermal properties may enable wider us of boride ceramcs in extreme environmants.

2. LITERATURE REVIEW

2.1. ZIRCONIUM DIBORIDE

Zirconium diboride belongs to the class of materials known as ultra-high temperature ceramics (UHTCs). UHTCs are generally classified as transition metal borides, carbides and nitrides with melting temperatures greater than 3000°C (22). Tucker and Moody were the first to synthesize ZrB_2 in 1901 by reacting elemental zirconium and boron (23). However, the compound was not thoroughly investigated until the space race led to new-found interest in materials that could withstand the extreme environments required by space flight. Beginning in the 1950s, the National Advisory Committee for Aeronautics (NACA), which would soon be incorporated into a newly formed National Aeronautics and Space Administration (NASA), recognized the need to expand materials capabilities and began a search for candidate materials for applications such as rocket motors and thermal protection systems (11,12). In the 1960s the U.S. Air Force funded studies investigating processing, properties, oxidation, and phase equilibria of transition metal carbides and borides. The comprehensive work published through these studies forms the fundamental knowledge we have of UHTCs.

2.1.1. Melting Temperature. In 1931, Agte was the first to measure the melting temperature of ZrB2 and reported it to be 3050°C (1). Agte utilized a new test method developed by Pirani and Alterthum in which the temperature of a specimen bar was monitored via a pyrometer sited in a black body cavity machined into the specimen. The specimen was then directly resistively heated in an environmentally controlled furnace and the time point and associated temperature was recorded at which liquid formed in the cavity (1,24). Unfortunately, Agte reported little further characterization of the specimen and only claims the composition was a zirconium boride of unknown stoichiometry as the compositional analysis was flawed. Under commission of the U.S. Air Force, Rudy utilized the same technique in extensive phase equilibria studies of the 1960s, and measured the melting temperature of ZrB2 to be 3245 ± 25°C (2).

2.1.2. Hafnium Separation. Zircon ($ZrSiO_4$) is the primary raw material used in the refinement of Zr metal and Zr-containing ceramics, and it naturally contains 1-3 wt% Hf (25). As a result of the difficulty in separating Hf and Zr, most commercial materials containing Zr have the natural abundance of Hf present. The separation on Hf from Zr is primarily motivated by the needs of the nuclear industry as it uses ~85% of the world's supply of Zr (25). Due to its low neutron cross section, Zr is used as a fuel cladding. In contrast, hafnium is a neutron absorber and must be limited to no more than 100 ppm in reactor grades of Zr and Zr compounds (26). However, the separation of the Zr and Hf is difficult due to their chemical and physical similarities such as identical valence state and atomic radii (1.45 Å and 1.44 Å respectively).

Separation of Zr and Hf occurs after carbochlorination of ore produces zirconium tetrachloride. Fractional crystallization and solvent extraction, primarily methyl isobutyl ketone (MIBK) extraction and tributyl phosphate (TBP) extraction, are the primary commercial methods for Zr-Hf separation (19). Fractional crystallization was industrially used in Russia during the cold war and relied upon the difference in solubility of K_2ZrF_6 and K_2HfF_6 in aqueous KF and HF solutions (27,28). The MIBK process dissolves $ZrCl_4$ in an HCl solution with ammonium thiocyanates and MIBK. Hafnium thiocyanates preferentially dissolve in the organic phase and are extracted. The MIBK process consists of 12-15 stages of separation and is capable of producing Zr with Hf content less than 25 ppm and Hf with Zr content less than 1 at% (19). The TBP process is fundamentally similar, but dissolves zirconium tetrachloride in nitric acid, uses TBP as the organic extraction solvent, and targets the Zr as the extracted metal (25,27,29).

2.1.3. Crystallography and Bonding. Group IV, V, and VI transition metal diborides (TMB_2s) form the hexagonal AlB_2 structure belonging to the space group 191(P6/mmm) (30). The structure is characterized by alternating basal planes of close packed transition metal atoms and graphite-like boron rings. The transition metal atoms are metallically bound together, making TMB_2s good electrical conductors. For example, ZrB_2 has an electrical conductivity of 1.6 x 10^7 S/m which is comparable to Ni or W (1.4 x 10^7 S/m and 1.9 x 10^7 S/m respectively) (15,31). Alternatively, the sp^2 covalent bonds in the B rings stiffens the unit cell leading to properties such as high Young's modulus (>500 GPa for Group IV and V TMB_2s) and melting temperature (32–35). The basal planes are iono-covalently bonded (33).

2.1.4. Densification. Densification is the process by which particles in a powder compact or green body coalesce and is associated with a thermally induced volumetric shrinkage of the bulk article. Microscopically it is associated with the removal of porosity, with a fully dense ceramic having no pores (36,37). Solid state sintering relies on diffusional processes for densification.

Diffusion is the periodic movement of atoms from one favorable energy site to another within the lattice. There are a number of diffusional mechanisms, or specific means for atomic movement, such as those presented in Figure 2.1. For an atom to move between energy sites, it must overcome an energy barrier known as the activation energy.

Each mechanism for diffusion has a characteristic activation energy associated with it for a given material. Generally mechanisms with higher activation energies will be dominant at higher temperatures compared to lower activation energy mechanisms that dominate at lower temperatures (38).

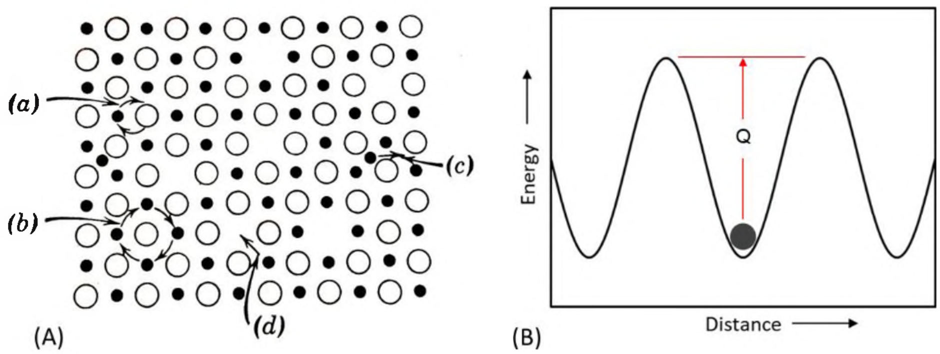

Figure 2.1: Mechanisms for Diffusion. (A) possible atomic diffusion mechanisms (a) exchange, (b) ring rotation (theoretically possible but not seen in real systems), (c) interstitial, and (d) vacancy (36). (B) Representation of activation energy (Q) required for atomic movement from one favorable energy site to another.

The driving force of densification is minimization of the free energy of the system. Primarily this is achieved by the reduction of surface free energy. Surface free energy can be represented by Equations 1-3 for an idealized system of uniform spherical particles consisting of an isotropic material (38).

$$N = \frac{3M}{4\pi a^3 \rho} = \frac{3V_m}{4\pi a^3} \tag{1}$$

Equation 1 describes the number of particles (N) for a mole of material with radii a, density ρ, molar volume V_m. and molar weight (M). The surface area (S_A) can be written as Equation 2, and the surface free energy (E_S) can be written as a function of specific solid-vapor interfacial energy (γ_{SV}), molar volume, and particle radii (Equation 3).

If molar volume is material property and specific surface energy is considered to be invariant then the only variable is the particle radii, and maximizing radii minimizes surface free energy (38). This driving force is present in all porous systems

$$S_A = 4\pi a^2 = \frac{3V_m}{a} \tag{2}$$

$$E_S = \frac{3\gamma_{SV} V_m}{a} \tag{3}$$

Externally applied pressure (P_a) can assist the densification by doing work (W) on the system approximated by Equation 4 (38).

$$W = P_a V_m \tag{4}$$

The Coble and Nabarro-Herring diffusion models describe this phenomenon in more detail. The Nabarro-Herring model assesses stress-directed vacancy diffusion by evaluating the movement of vacancies from crystal faces in tension to crystal faces in compression and the counter-diffusion of atoms from a crystal face in compression to a crystal face in tension (Figure 2.2: Atomic diffusion currents within grains due to applied stresses (36).2) (39,40). This model is also known as vacancy creep and can be used to describe lattice diffusion for pressure assisted sintering techniques such as hot pressing (HP), direct current sintering (DCS), and hot isostatic pressing (HIP) (41–43). Equation 5 describes the model

$$\dot{\varepsilon}_l = N_l \frac{D_l \Omega P_a}{G^2 kT} \tag{5}$$

where $\dot{\varepsilon}$ is the strain rate, N_l is the lattice diffusion constant, D_l is the lattice diffusion coefficient, Ω is the unit cell volume, P_a is applied stress, G is grain size, k is the Boltzmann constant, and T is absolute temperature.

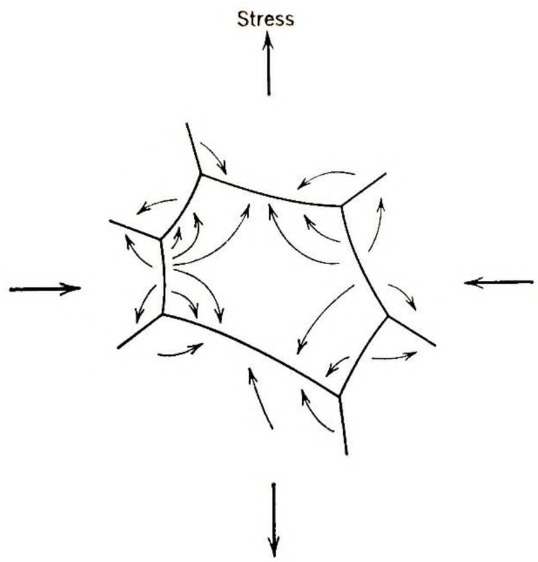

Figure 2.2: Atomic diffusion currents within grains due to applied stresses (36).

The Coble model is also based upon stress-directed diffusion, but instead describes diffusion of atoms along grain boundaries. Because it is derived from Nabarro and Herring's work, it is similar but the grain size term is cubed and takes into account the width of the grain boundary (δ_{gb}) (44,45). Equation 6 describes the model.

$$\dot{\varepsilon}_{gb} = N_{gb} \frac{D_{gb}\delta_{gb}\Omega P_a}{G^3 kT} \quad (6)$$

Kalish and Clougherty were among the first to apply the Nabarro-Herring model to diborides. Studying high pressure (800 MPa) hot pressed HfB_2, they reported an activation energy of 96 kJ/mol in the final stage of densification ($\rho_{relative} > 90\%$) and hypothesized the dominant mechanism was either interstitial diffusion of boron or grain boundary diffusion of Hf (41). Several studies have investigated the dominant mechanisms associated with the intermediate stage of densification ($\sim 65\% < \rho_{relative} < 90\%$) in ZrB_2. The reported activation energies range from 140 to 695 kJ/mol for either grain boundary diffusion (associated with lower activation energies) or lattice diffusion (associated with high activation energies) as the dominant mechanism (46–49). Finer initial particle sizes and increased applied pressures were credited with reduction of activation energy, although activation energy should only be dependent on densification mechanism. Lonergan was able to clarify the disparate data. Lonergan determined that grain boundary diffusion was dominant up to ~2000°C with an activation energy of 241 kJ/mol. Above ~2000°C lattice diffusion was dominant with an activation energy of 695 kJ/mol (42). To date, no studies have addressed the mechanisms active in the final stage of sintering of ZrB_2.

2.1.5. Pressure Assisted Sintering. Due to strong covalent bonding and low self-diffusion coefficients, diboride ceramics are difficult to densify without sintering aids and/or the application of external pressure. Pressure assisted techniques such as hot pressing and direct current sintering are able to fully densify ZrB_2, but generally require temperatures above 1800°C and pressures of 32 MPa (14,47,50,51). While sintering aids such as B_4C, WC, SiC, or $MoSi_2$ can be used to reduce sintering temperatures, these additives can also be the source of impurities that form either solid solutions or secondary phases (43,43,52–56).

Reaction based methods such as reactive hot pressing (RHP) and reactive DCS (RDCS) have been used to produce high relative density ZrB_2 at temperatures lower than traditional HP while also reducing the amount secondary phases present (47,50,57). Lonergan densified ZrB_2 to 98.2% at 1800°C without the use of sintering aids by RHP (47). Likewise, Guo was able to densify ZrB_2 to 95% at 1750°C by RDCS without sintering aids (50). None of these studies examined the mechanisms in the final stage of densification.

2.1.6. Thermal Conductivity. Thermal conductivity (k) is the ability of a material to transfer heat, and can be defined as the heat flux (q) through a material over a temperature gradient (ΔT) (Equation 7) (58).

$$k = \frac{-q}{\Delta T} \tag{7}$$

In solid matter, heat can be transferred by photons, phonons and electrons, and the total thermal conductivity of a material can be defined as the sum of the contribution by each of these mechanisms in Equation 8 (13)

$$k = k_{pt} + k_p + k_e \tag{8}$$

where k_{pt} is the photon conduction, k_p is the phonon conduction, and k_e is the electron conduction. The photonic contribution is not generally considered in dense opaque ceramics.

Thermal conductivity can be directly measured by the guarded hot plate method (ASTM E1225), hot wire method (ASTM C1113), comparative flow method (ASTM C518) (59–61). While measurement of k appears to be straightforward, these experimental methods are subject to several sources of error such as the difficulty in establishing and maintaining a steady-state temperature gradient through the specimens or unaccounted heat loss through specimen perimeters. Due to these complications, thermal conductivity is often be calculated from thermal diffusivity (D), constant pressure heat capacity (C_p), and density (ρ) as seen in Equation 9.

$$k = DC_p\rho \tag{9}$$

Reported thermal conductivity of fully dense ZrB_2 ranges from 55-141 W/m•K (4,15,17,62–67). In part, the disparity in reported values stems from contaminants from processing methods such as Fe and WC contamination from milling media erosion, secondary phases, and impurities in initial powder (4,68–71). In particular, Lonergan studied the effect of reducing Hf content on the thermal conductivity of ZrB_2 and reported increasing thermal conductivity from 100 to 141 W/m•K by decreasing Hf content from 0.33 at% to 0.01 at% (4). McClane studied the effect of Ti, V, Cr, Y, Nb, Mo, Hf, Ta, W, and Re solid solution additions (3 at%) on ZrB_2 thermal conductivity. While some additions such as Ti and Y had no measurable effect on thermal conductivity, most additions significantly reduced thermal conductivity. For example, additions of W and Cr decreased the thermal conductivity to 34 W/m•K and 28 W/m•K at 25°C respectively (67,72).

2.1.7. Phonon Conduction. Phonons are elastic vibrations of the lattice producing quantized amounts of energy associated with wave-like solutions to equations defining the motion of the atoms. These solutions define the fundamental motion of atoms with respect to their neighbors in the lattice and are called modes. Normal modes are specific vibrations of the atoms in which all atoms share the same frequency, and all lattice vibrations can be described by superposition of these normal modes (36,73,74).

According to the classical gas model, phonon conductivity is proportional to the constant volume heat capacity (C_V), mean free path of the phonon (λ) and phonon velocity (v) (Equation 10) (75).

$$k \cong \frac{1}{3} C_V \lambda v \tag{10}$$

$$v = 0.87\sqrt{\frac{B}{\rho}} \tag{11}$$

The phonon velocity can be described by the bulk modulus (B) and density (ρ) as shown in Equation 11 (76).

Temperature significantly affects conductivity and can be described by four main regimes illustrated in Figure 2.3. At 0 K no heat can be transferred because lattice vibrations do not exist. At low temperatures above 0 K, phonons transfer heat proportional to cubed temperature (T^3). While phonons interact in this temperature regime, all interactions are elastic and there is no thermal resistance. In the intermediate temperature range, phonons carry enough energy to scatter inelastically by Umklapp processes. Umklapp scattering provides a mechanism for thermal resistance to occur, and phonon thermal conductivity begins to decay exponentially with temperature (Equation 12) where θ is the Debye temperature which is defined as the temperature at which all normal modes of vibration are active for a particular material (77).

$$k \cong e^{\frac{-\theta}{T}} \tag{12}$$

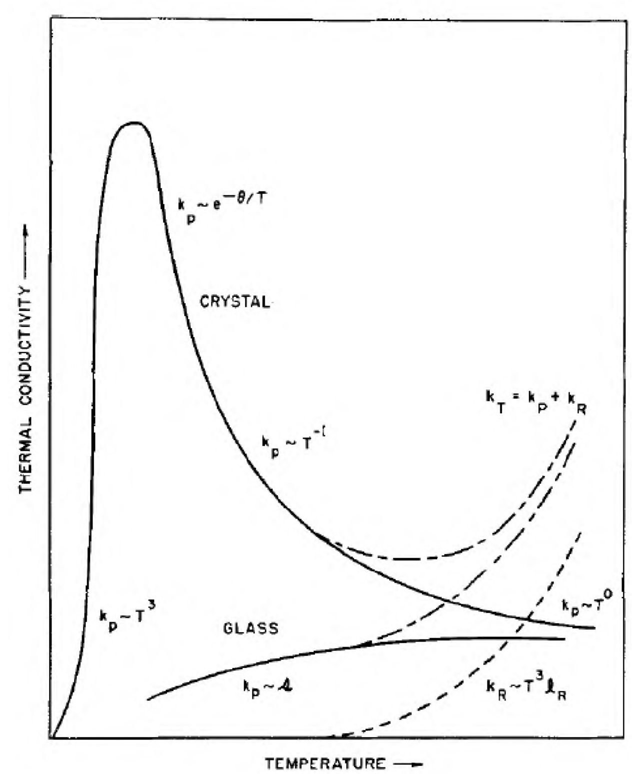

Figure 2.3: Thermal conductivity of phonons (77).

Above the Debye temperature, the conductivity decreases inversely proportional to the temperature. The final regime of phonon thermal conductivity is not temperature dependent (77).

$$\frac{1}{\lambda} = \frac{1}{\lambda_{solvent}} + \frac{1}{\lambda_{solute}} \tag{13}$$

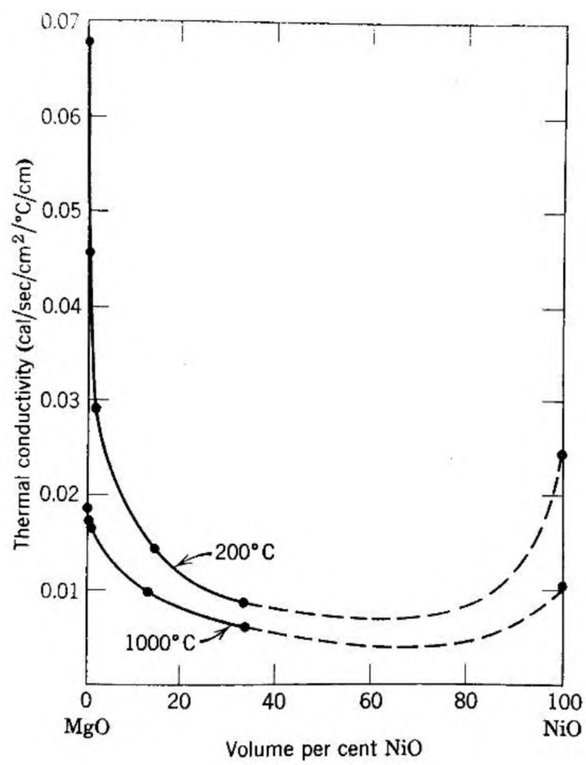

Figure 2.4: Thermal conductivity in the MgO-NiO system (36).

Point defects such as vacancies or substitutional solid solutions decrease phonon thermal conductivity by providing scattering sites. In the case of solid solutions, the inverse mean free paths are additive and equal to Equation 13 (36). The resulting decrease in k due to this phenomenon is exemplified by the MgO-NiO system (Figure 2.).

2.1.8. Electron Conduction. Electron conductivity is the transfer of energy by free electron motion and is proportional to the thermal conductivity of a material as described by the Wiedemann-Franz law (Equation 14), where k_e is the thermal conductivity due to electrons, L_0 is the theoretical Lorenz number (2.44 x 10^{-8} W•Ω/K^2) and σ is the electrical conductivity (75).

$$k_e = L_0 T\sigma \tag{14}$$

The electron thermal conductivity can also be described by the Fermi velocity (v_f), relaxation time, (τ) and constant volume heat capacity (C_V) (Equation 15) (75). The Fermi velocity is defined by Fermi energy (E_f) and the effective mass of the electron (m^*) (Equation 16) (75).

$$k_e = \frac{1}{3}v_f^2\tau C_V \tag{15}$$

$$v_f^2 = \frac{2E_f}{m^*} \tag{16}$$

2.1.9. Experimental Values. Room temperature values of ZrB_2 thermal conductivity range from 24 to 141 W/m•K in literature (4,78). Especially low values are attributed to low relative densities (85%) with the lowest values for fully dense ZrB_2 as low as 56 W/m•K (79). Among polycrystalline ceramics, grain size has no apparent correlation to thermal conductivity as values as low as 57 W/m•K and high as 107 W/m•K were reported for ZrB_2 with average grain sizes of ~10 µm (50,79–81). There is a similar range for samples with grain sizes reported above ~20 µm suggesting thermal resistance across grain boundaries is low (68,82). The effect of purity is more pronounced, with the highest reported k values resulting from studies utilizing reactive processes to synthesize ZrB_2 (4,50). Unfortunately, many studies do not provide compositional data. The highest reported k for ZrB_2 is 141 W/m•K and was produced by

RHP of reactor grade ZrH_2 (100 ppm Hf) and elemental B (4). The same study also proved that increasing Hf content led to a decrease in thermal conductivity with the Hf impurity atoms likely served as phonon scattering sites. Additions of only 0.33 at% Hf decreased k to 100 W/m•K. Figure 2.3 summarizes several representative thermal conductivity studies for ZrB_2.

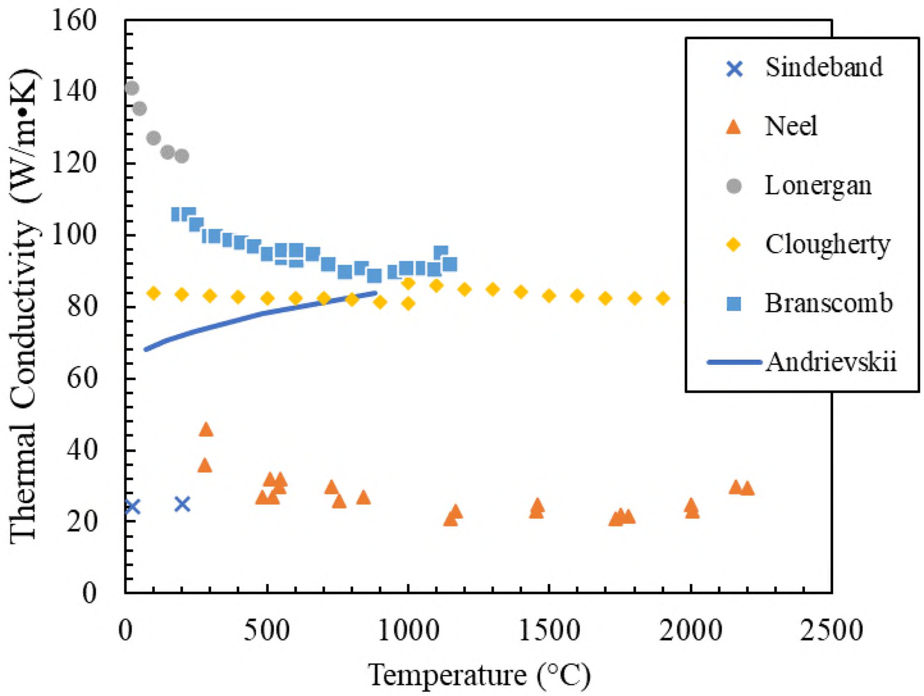

Figure 2.5: ZrB_2 thermal conductivity (4,62,64,65,78,83).

2.1.10. Thermal Diffusivity. Thermal diffusivity (*D*) is the ratio of a material's ability to conduct thermal energy to its ability to store thermal energy. Practically, *D* indicates how quickly a thermal gradient will equilibrate through a material. Unlike thermal conductivity, *D* is directly measured relatively easily. The laser flash method (ASTM E1461) is used to measure thermal diffusivity of flat specimens of a uniform composition (84). As indicated in Figure 2.6, the temperature on the specimen back face is monitored after the front face is exposed to an energy pulse over a very short time scale. Equation 17 is used to calculate the thermal diffusivity where L is the specimen thickness and $t_{1/2}$ is the half-rise time (84).

$$D = 0.13879L^2/t_{1/2} \tag{17}$$

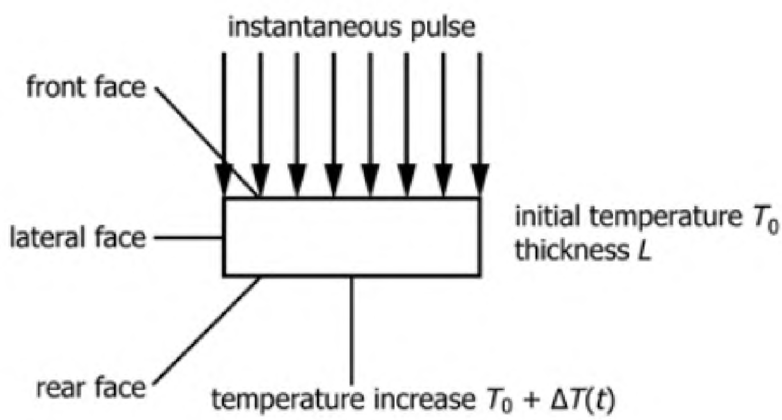

Figure 2.6: Schematic of the specimen in the laser flash method (84).

Because thermal diffusivity and thermal conductivity are intimately related, literature values of D vary greatly in the same manner as k. Typical room temperature values for ZrB_2 range from 0.18 to 0.33 cm^2/s with high values correlating to single phase ZrB_2 with natural abundance of Hf, and lower values corresponding to ZrB_2 with secondary phases (85,86). Diffusivity increases with decreasing Hf content. Lonergan measured diffusivity for ZrB_2 with 100 ppm Hf to be 0.47 cm^2/s (4).

2.2. HIGH ENTROPY CERAMICS

High entropy boride (HEB) ceramics have recently attracted attention as a new class of ultra-high temperature ceramics due to their potential for improved thermal stability, mechanical properties, oxidation resistance, radiation damage tolerance, and a generally broadened material design space compared to boride ceramics containing a single transition metal (20,21,87–93). In particular, one potential benefit of the entropy stabilization/high entropy approach is the stabilization of elements in a structure in which they are not thermodynamically stable in a conventional binary compound due to the increased configurational entropy (94). While several solid solutions and high entropy boride ceramics have been produced containing group IV-VI transition metals, no research to date has focused on the effect of entropy stabilization on the solubility of specific species in the boride lattice (4,17,21,86,95).

2.2.1. Theory. The guiding principle of high entropy materials is the reduction of the Gibbs' free energy (*G*) of the system by maximizing the entropy (*S*) as seen in Equation 18 where H is enthalpy and T is absolute temperature.

$$G = H - TS \tag{18}$$

This is achieved by increasing the configurational entropy by increasing the number of species (N) in the system as seen in Equation 19 where R is the universal gas constant (96,97).

$$S = R\ln N \tag{19}$$

While any additional species in the lattice will increase the entropy of mixing, current work in high entropy ceramics focus on increasing the number of transition metal species in the metal sublattice (21,98–100).

2.2.2. Entropy Stabilization. While increasing the configurational entropy is relatively straightforward, there has been debate over the entropy stabilization effect in high entropy materials (101–104). Rost et al. investigated the entropy stabilization effect in the (Mg,Co,Ni,Cu,Zn)O system and determined that the increased configurational entropy indeed stabilized a single oxide phase. Their study focused on oxide pairs that did not exhibit appreciable solid solubility such as MgO-ZnO and CuO-NiO and species were chosen that were not necessarily isostructural. Rost reported that the formation of a single solid solution phase unambiguously provided evidence for entropy stabilization and hypothesized the ionic character of the system aided in the stabilization (94). To the author's knowledge, no similar studies have reported this effect in HEBs.

2.2.3. Solid Solution Models. Through phase equilibria studies of binary alloys, Hume-Rothery formulated a set of guidelines to predict whether a binary system will exhibit infinite solid solubility (105,106):

- Metallic radii of solute and solvent atom may not differ by more than 15%
- Crystal structures of solute and solvent atoms must be similar
- Valence state of solute and solvent atoms must be similar
- Electronegativities of solute and solvent atoms must be similar

It is important to note that these are guidelines and are still scrutinized as even Hume-Rothery constantly revised the rules. For example, Hume-Rothery first predicted that the critical atomic radii difference was 13% before reviewing Pauling's studies of metallic radii and concluding 15% of the metallic radii was more accurate (105–107).

Vegard's law (Equation 20) states that the lattice parameter (a) of a binary solid solution of components A and B is given by the weighted averages based upon their molar fraction (x) (108). While deviation from Vegard's law is observed when non-ideal solution behavior is exhibited, it is generally considered a good approximation in isostructural binary systems (109).

$$a_{A_{(1-x)}B_x} = (1-x)a_A + x\,a_B \tag{20}$$

Both of these models are used in the selection of candidate constituents for HEB systems.

2.2.4. Current Efforts. A significant portion of the current work with HEBs is centered around synthesis and processing. The first study of HEBs utilized commercially available TMB_2 powders and contained secondary phases, particularly surface oxides present on starting powders or from contamination during comminution efforts involving high energy ball milling (HEBM) for 6 hours, and low relative densities (<92%) (21). Phase separation was also an issue with W containing samples forming $(Ti,W)B_2$. Despite these issues, the study produced 6 compositions with single boride phases: $(Hf,Zr,Ta,Nb,Ti)B_2$, $(Hf,Zr,Ta,Mo,Ti)B_2$, $(Hf,Zr,Mo,Nb,Ti)B_2$, $(Hf,Mo,Ta,Nb,Ti)B_2$, $(Mo,Zr,Ta,Nb,Ti)B_2$, and $(Hf,Zr,Ta,Cr,Ti)B_2$. To reduce oxide impurities and processing times, several groups have begun synthesizing their own HEBs via reactive processes, especially the borocarbothermal reduction (BCTR) of oxide precursors (91,110–113). The advantage of the BCTR method is that it produces high-purity, submicron HEB powders. Despite utilizing carbon, and oxide precursors, oxygen contamination can be mitigated resulting in O contents as low as 0.3 wt% while maintaining C levels of ~0.3 wt% (114). Generally the borocarbothermal reduction of oxides takes place during a isothermal hold between 1600-1650°C, but boride components may not fully dissolve without isothermal holds of ~2000°C (114). Self-propagating high temperature synthesis (SHS) has also been used successfully but to less extent (115,116).

Synthesis efforts have also benefitted the densification of HEBs. Powders synthesized by BCTR have been sintered to densities >99% by SPS utilizing pressures of 30-50 MPa and temperatures of 2000-2100°C (112,116,117). DCS is almost exclusively used, although one reported instance of HP at 1927°C and 50 MPa resulted in $(Hf_{0.2},Zr_{0.2},Ti_{0.2},Ta_{0.2},Nb_{0.2})B_2$ with a relative density of 98.7% (113).

Table 2.1: Hardness of selected HEBs and ZrB_2.

Composition	relative density (%)	grain size (μm)	HV (GPa)	HV force (kgf)	Reference
$(Hf_{0.25},Zr_{0.25},Ti_{0.25},Ta_{0.25})B_2$	100	13.9 ± 5.5	23.7 ± 0.3	0.2	(118)
$(Hf_{0.2},Zr_{0.2},Ti_{0.2},Ta_{0.2},Nb_{0.2})B_2$	99.5	5.2 ± 2.0	25.3 ± 0.6	0.2	(118)
$(Hf_{0.2},Zr_{0.2},Ti_{0.2},Ta_{0.2},Nb_{0.2})B_2$	99.2	8.6 ± 4.8	26.0 ± 1.5	0.2	(119)
$(Hf_{0.2},Zr_{0.2},W_{0.2},Ta_{0.2},Nb_{0.2})B_2$	98.1	14.8 ± 11.7	26.7 ± 1.1	0.2	(119)
$(Hf_{0.2},Zr_{0.2},Ti_{0.2},Ta_{0.2},Nb_{0.2})B_2$	97.9	41.2 ± 8.1	22.4 ± 0.6	0.2	(120)
ZrB_2	97.9	7.2	14.6	10	(121)
ZrB_2	83.7	--	15.4 ± 1.1	0.2	(21)

Thus far studies reporting properties of HEBs focus on hardness. HEBs exhibit higher hardness than single phase borides or predicted by rule of mixtures which is attributed to solid solution hardening (122). Table summarizes several HEBs and includes ZrB_2 for reference. One study has measured the thermal conductivity of 3 equimolar 5-component HEB compositions(91). Of those compositions, $(Hf,Zr,Ti,Ta,Nb)B_2$ had the highest thermal conductivity of 24.8 ± 5.1 W/m•K, and $(Hf,Zr,Ti,Ta,Cr)B_2$ had the lowest thermal conductivity of 12.6 ± 2.5 W/m•K . Thermal conductivity of HEBs are significantly lower than single component borides, and the study concluded this was due to increased phonon scattering. However, thermal conductivity was calculated utilizing heat capacity calculated by a rule of mixtures and assumed to be 2.5 $J/cm^3 \cdot K$ for all compositions. Also, discussion of the thermal conductivity did not analyze the individual phonon and electron contributions to thermal conductivity. There is a significant gap in the literature where only one study has reported values of thermal properties, heat capacity and electrical properties must also be measured to further understand why thermal conductivity of HEBs are lower than single component borides.

PAPER

I. EFFECTS OF TI, Y AND HF ADDITIONS ON THE THERMAL PROPERTIES OF ZrB_2

Austin D. Stanfield, Gregory E. Hilmas, William G. Fahrenholtz

Deparment of Materials Science and Engineering, Missouri University of Science and Technology, Rolla, MO 65409

ABSTRACT

Reactive hot pressing was utilized to synthesize and densify four ZrB_2 ceramics with impurity contents low enough to avoid obscuring the effects of dopants on thermal properties. Nominally pure ZrB_2 had a thermal conductivity of 141 ± 3 W/m•K at 25°C. Additions of 3 at% of Ti, Y, or Hf decreased the thermal conductivity by 20%, 30%, and 40%, respectively. The thermal conductivity of $(Zr,Hf)B_2$ was similar to ZrB_2 synthesized from commercial powders containing the natural abundance of Hf as an impurity. This is the first study to demonstrate that Ti and Y additions decrease the thermal conductivity of ZrB_2 ceramics and report intrinsic values for thermal conductivity and electrical resistivity of ZrB_2 containing transition metal additions. Previous studies were unable to detect these effects because the natural abundance of Hf present masked the effects of these additions.

1. INTRODUCTION

Zirconium diboride (ZrB_2) is an ultra-high temperature ceramic (UHTC) based on its melting temperature of more than 3000°C. ZrB_2 has a hexagonal crystal structure comprised of alternating layers of metallically bonded zirconium and covalently bonded boron with iono-covalent bonding between these planes (1). Interest in ZrB_2 ceramics is driven by properties such as strength (>500 MPa), hardness (>20 GPa), thermal conductivity (55-133 W/m•K) and chemical inertness (2-5). These properties make ZrB_2 based ceramics candidates for applications such as high speed cutting tools, high temperature electrodes, refractory lining and leading edges for hypersonic aerospace vehicles (6-9). For the latter application, higher thermal conductivity values increase performance by increasing the ability of the material to transport heat away from leading edges so that the heat can be dissipated elsewhere (10).

Due to strong covalent bonding and low self-diffusion coefficients, ZrB_2 ceramics are difficult to densify without sintering aids (11). Pressure assisted techniques such as hot pressing (HP) and spark plasma sintering (SPS) are able to achieve full densification, but only at temperatures above 2100°C and pressures of 32 MPa or higher (12). While sintering aids such as B_4C, WC, SiC, or $MoSi_2$ can be used to reduce sintering temperatures, these additives can also be the source of impurities that form either solid solutions or secondary phases (13-16).

Reaction-based methods such as reactive hot pressing (RHP) and reactive SPS have been used to produce high relative density ZrB_2 at temperatures lower than traditional HP while also reducing the amount of secondary phases present. Zhang densified ZrB_2 to 92.5% at 1900°C without the use of sintering aids by reactive SPS (17). Likewise, Guo was able to densify ZrB_2 to 95% at 1750°C by reactive SPS without sintering aids (4). One advantage of reactive processes is the potential to minimize transition metal (TM) impurities, which have been shown to decrease the thermal conductivity of ZrB_2 ceramics (18-20). In particular, Lonergan studied the effect of Hf content on the thermal conductivity of ZrB_2, and showed that decreasing the Hf content increased thermal conductivity from about 100 W/m•K for an Hf content of 0.33 at% to 141 W/m•K for an Hf content of 0.01 at%. Lonergan also measured the Hf content of a commonly used commercial ZrB_2 (Grade B, H.C. Starck Inc., Newton, USA) by inductively coupled mass spectrometry (ICP-MS) and found that it was ~1.7 at%. Lonergan attributed the decrease in thermal conductivity with increasing Hf content to the effect of impurity atoms on phonon transport in the ZrB_2 lattice (20). Yokota also measured Hf content of two commercial ZrB_2 powders (Nippon Shin Kinzoku, Tokyo, JPN; and Johnson Matthey, London, GBR) by inductively coupled plasma atomic emission spectrometry and reported Hf contents of 1.56 wt% and 1.67 wt% respectively (21).

McClane studied the effect of individual TM additions on the thermal conductivity of ZrB_2 ceramics (19). Those studies examined additions of 3 at% Hf, Nb, W, Ti, Y, Ta, Mo, Re, V, or Cr to commercial ZrB_2 powders. All of these TM additions decreased thermal conductivity, with the exceptions of Ti and Y, which were found to have no effect on thermal conductivity (18-19). McClane concluded that the effects of Ti and Y were masked by the presence of the natural abundance of Hf present in ceramics produced from commercial ZrB_2 powders, but provided no experimental verification for that hypothesis.

The purpose of the present study was to investigate the effects of small additions of transition metals on the intrinsic thermal properties of ZrB_2 ceramics (i.e., free of the extrinsic effect of dissolved Hf impurities). This was achieved by comparing the thermal conductivity of ZrB_2 and ZrB_2-TM solid solutions containing low amounts of Hf.

2. EXPERIMENTAL PROCEDURE

Raw materials were batched to minimize the residual oxygen content in the final ceramics according to the method described by Neuman (22). Zirconium hydride (< 45 ppm Hf; CRS Chemicals, Canoga Park, USA) and amorphous boron (Grade SP-95; SB Boron Products, Bellwood, USA) were batched in a molar ratio of 1 to 2.1. In addition to ZrB_2 with no additives (ZB), three compositions were produced containing 3 at% of a single TM diboride additive to produce $(Zr_{0.97},TM_{0.03})B_2$ ceramics. Titanium diboride (HCT-F; Momentive, Strongsville, USA) was added to produce $(Zr,Ti)B_2$ (designated ZTB) while HfB_2(99.5%; H.C. Starck Inc., Newton, USA) was added to produce $(Zr,Hf)B_2$ (designated ZHB). Because YB_2 is not stable, $(Zr,Y)B_2$ (designated ZYB) ceramics were produced by adding Y (99.9%; Alfa Aesar, Ward Hill, USA) and amorphous B in a 1:2 stoichiometric ratio to the 3 at% level. Powders were ball milled for four hours in acetone with ZrO_2 media to mix the powders. Phenolic resin (GP 2074, Georgia Pacific, Atlanta, USA) was added for the last hour of mixing to protect the particle surfaces from oxygen and act as a carbon source to react with and remove surface oxides already on the particles. Slurries were dried by rotary evaporation (Rotovapor R-124; Buchi, Flawil, DEU). The subsequent powder was lightly ground to break agglomerates and passed through a 50 mesh screen. Ceramics were produced by RHP in a 25.4 mm diameter graphite die lined with graphite paper (0.005"; Graftech International, Lakewood, USA) and coated with BN (SP-108; Materion, Milwaukee, USA). The HP (Model HP20-3060-20; Thermal Technology, Santa Rosa, USA) was heated at 5 °C/min to 950 °C under flowing $Ar/10H_2$ with hour holds at 800°C and 950°C. The HP was evacuated to ~10 Pa (~ 100 mTorr) and heated to 1250°C with an hour hold at 1250°C. The HP was heated at 10 °C/min to 1650°C with a 2 hour hold at 1450°C and an hour hold at 1650°C. After the hold at 1650°C, the furnace was backfilled to ~10^5 Pa with flowing Ar and 32 MPa pressure was applied. The HP was heated at 50 °C/min to the final sintering temperature of 2100°C. Specimens were held for 30 minutes at the densification temperature then cooled at 50 °C/min. Upon cooling, pressure was released at 1600°C. Specimens were surface ground to a thickness of 1.8 mm and surface roughness of ~45 μm. Cylindrical thermal diffusivity specimens were cut to 12.7 mm diameter using a wire electrical discharge machine (Agiecut 150 HSS; Agie, Geneva, Switzerland). Bulk density was determined by Archimedes' principle (ASTM B962) with distilled water used as the immersing medium. Billets were crushed and ground to -200 mesh for X-ray diffraction (XRD; X'Pert Pro, PANalytical, Almelo, NLD). Phase analysis of XRD data was performed by Rietveld refinement (RIQAS4, Materials Data Incorporated, Livermore, USA). Phases were modeled using ICSD 030327 for ZrB_2, ICSD 072951 for t-ZrO_2, and ICSD 022264 for ZrC. Lattice parameters determined using Rietveld refinement of XRD data were used to calculate theoretical density. Microstructures were examined by scanning electron microscopy (SEM) and energy dispersive spectroscopy (EDS; Helios NanoLab 600, FEI, Hillsboro, USA). Grain size was determined using computerized image analysis (ImageJ; National Institutes of Health, Bethesda, MD) of a minimum of 250 grains for each specimen. Assuming random grain orientation, the projected area of each grain was measured and the equivalent circular diameter was calculated and used as the average grain size. Thermal diffusivity was measured with a Flashline S2 (Anter Corporation, Pittsburgh, USA) according to the laser flash method as outlined in ASTM E1461. Thermal diffusivity was measured from 25°C to 200°C because this temperature region shows a stronger dependence on impurities than the higher temperature regime that is dominated by electron contribution to thermal conductivity. Additionally, the lower temperature regime was studied to minimize the potential for changes to the specimens during measurements such as grain growth or diffusion of carbon into the ZrB_2 lattice. Reported values are an average of sampling each specimen 5 times at each temperature. The Clark and Taylor method was used to calculate thermal diffusivity (α) according to Equations 1-3).

$$\alpha_{corrected} = \frac{\alpha K_R}{0.13885} \tag{1}$$

$$\alpha = 0.1338\frac{L^2}{t_{0.5}} \tag{2}$$

$$K_R = -0.3461467 + 0.361578\left(\frac{t_{0.75}}{t_{0.25}}\right) - 0.06520543\left(\frac{t_{0.75}}{t_{0.25}}\right)^2 \tag{3}$$

where K_R is the Clark and Taylor correction factor, L is the specimen thickness, and t_n is the time required for the temperature to increase by n of the peak temperature rise. From this, thermal conductivity was calculated by Equation 4).

$$k = \alpha\rho C_p \tag{4}$$

where k is the thermal conductivity (W/m•K), ρ is the bulk density of the specimen, and C_p is the constant pressure heat capacity. The heat capacity of low-Hf ZrB_2 was taken from Lonergan, et al. and the heat capacities of all other phases were taken from the NIST-JANAF tables (23,24).

Electrical resistivity (ρ_e) was measured from 25°C to 200°C on cylindrical specimens of 12.7 mm diameter and 2 mm thickness by the van der Pauw method, as outlined in ASTM F76, and described in more detail with respect to electrical resistivity measurements on diboride ceramics by McClane (19,25).

3. RESULTS AND DISCUSSION

Table 1 summarizes the density, grain size, and impurity phase content for all four compositions. Ceramics produced by RHP had high relative density and exhibited complete dissolution of the transition metal additions. Transition metal additions were homogeneously distributed as shown qualitatively by EDS and dissolution into the ZrB_2 lattice was confirmed by changes to the lattice parameters determined by XRD. Analysis of XRD patterns (Figure 1) revealed that the specimens contained a single diboride phase, ZrB_2 (PDF:01-075-0964), but small amounts of tetragonal ZrO_2 (PDF:01-086-1546) were detected in the ZB, ZYB, and ZHB specimens. Observed peak shifts from nominally pure

Table 1: Density, grain size, and secondary phases of tested compositions

Designation	Theoretical Density (g/cm^3)	Bulk Density (g/cm^3)	Relative Density (%)	Grain Size (μm)	t-ZrO_2 (wt%)	ZrC (wt%)	a-axis$_{measured}$ (Å)	a-axis$_{Vegard's}$ (Å)	% Difference
ZB	6.105	6.045	99.0	5.8 ± 4.4	3.7	--	3.16826	3.16826	0.0000%
ZTB	6.059	6.032	99.6	2.8 ± 2.1	--	--	3.16538	3.16409	-0.0406%
ZYB	6.141	6.052	98.4	2.3 ± 1.5	8.6	9.0	3.16848	3.17218	0.1166%
ZHB	6.290	6.211	98.7	4.9 ± 2.1	3.8	9.8	3.16805	3.16741	-0.0201%

ZrB_2 indicated that TMs were incorporated into solid solution in each of the compositions and the shifts were consistent in magnitude with shifts estimated using Vegard's law for an addition of 3 at% of the respective TM. ZrC (PDF:01-073-0477) was also found in the ZYB and ZHB specimens. ZB contained ~4 wt% t-ZrO_2 based on Rietveld refinement. ZYB contained ~9 wt% of both ZrC and t-ZrO_2. ZHB contained ~10 wt% ZrC and ~4 wt% ZrO_2. Analysis of secondary phases from SEM images assuming that grain areas were equivalent to volume fractions were consistent with XRD results. No secondary phases could be detected in ZTB by XRD (Figure 1) nor were any observed by SEM (Figure 2). For the present study, the effects of second phases on thermal properties were assumed to be insignificant compared to the effects of dissolved transition metals. A systematic study of the effect of ZrO_2 on the thermal properties of ZrB_2 has not been reported, but Andrievskii studied the effect of ZrC on k of ZrB_2, and reported a decrease of ~10 W/m•K for ZrB_2 containing 10 vol% ZrC (26). Similar changes in thermal conductivity are expected for ZrO_2 inclusions. The differences in thermal conductivity values among the materials in the present study ranged from 30 W/m•K to 50 W/m•K, so the effects of second phases should be less than the effects of the solid solution additions. ZB had an average grain size of 5.8 ± 4.4 µm. The other three ceramic had similar grain sizes with ZTB at 2.8 ± 2.1 µm, ZYB at 2.3 ± 1.5 µm, and ZHB at 4.9 ± 2.1 µm. Based on the large standard deviations, the differences are not statistically significant (i.e., the variances overlap). In addition, Lonergan determined that average grain sizes in this range did not have a significant effect on thermal diffusivity of ZrB_2 (27). Bulk density measurements revealed relative densities greater than 98% for all compositions with negligible open porosity, which was consistent with observations by SEM that revealed minimal porosity in all samples with the exception of ZHB. Porosity overestimation by image analysis in ZHB is likely due to grain pull-out that occurred during machining and polishing. The small amount of porosity was not accounted for in analyses of thermal or electrical properties. Lonergan studied the effect of porosity on the thermal conductivity of ZrB_2 and showed that decreasing relative density from 99.7% to 97.3% led to a decrease in k of ~5% (27). As with impurities, this effect was much less than the observed differences in thermal conductivity among the different compositions.

Table 2: Thermal properties of ZrB_2 ceramics at 25°C.

Designation	Thermal Diffusivity (g/cm^3)	Heat Capacity (J/g•K)	Thermal Conductivity (W/m•K)	Electrical Resistivity (μΩ•cm)
ZB	0.475 ± 0.010	0.488	141 ± 3	6.36 ± 0.18
ZTB	0.434 ± 0.004	0.425	112 ± 2	7.73 ± 0.26
ZYB	0.366 ± 0.002	0.443	100 ± 1	8.24 ± 0.08
ZHB	0.307 ± 0.006	0.444	86 ± 1	8.13 ± 0.20

Table 2 summarizes the thermal properties of the ZrB_2 ceramics. The effect of TM additions on the thermal conductivity of ZrB_2 ceramics produced by RHP is summarized in Figure 3. Previously, additions of Ti and Y to ZrB_2 ceramics produced from commercial powders were found to have no effect on

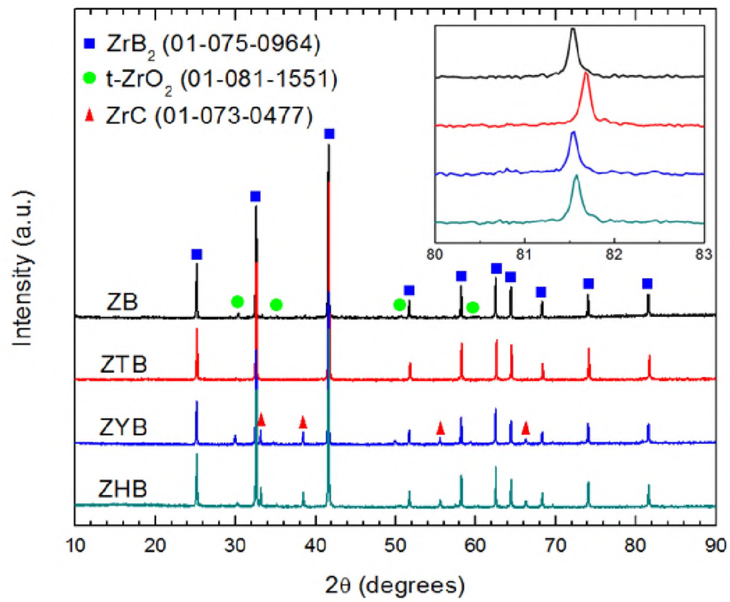

Figure 1: XRD patterns of RHP ZrB_2 specimens with peak shift at high angles (inset).

thermal conductivity (19,20). However, McClane et al. concluded that the effects of Ti and Y additions were masked by other impurities, presumably the natural abundance of Hf present in the commercial powders used to produce the ceramics in those studies (19,20). The thermal conductivity of ZB in the present study was 141 W/m•K at 25°C. This is ~40% greater than the reported thermal conductivity for ceramics produced by hot pressing commercial ZrB_2 (CZB; Grade B; H.C. Starck Inc., Newton, USA), which was 87 W/m•K at 25°C (19). The thermal conductivity of ZB is consistent with values reported by Lonergan and Guo who measured room temperature thermal conductivity values of 141 W/m•K and 133 W/m•K, respectively (4,20). As concluded by Lonergan (24), the increase in thermal conductivity for ceramics produced by RHP compared to those produced from commercial powders is likely due to changes in the phonon contribution to thermal conductivity that result from the lower content of Hf impurities dissolved in the ZrB_2 lattice of ZB compared to CZB. The thermal conductivity of ZB decreased to 124 W/m•K at 200°C, presumably due to an increase in electron and phonon scattering as temperature increased (28).

The addition of TMs decreased thermal conductivity of ZrB_2 ceramics. The addition of 3 at% Hf decreased the room temperature thermal conductivity of ZHB to 86 W/m•K. This value, is comparable to the thermal conductivity of ~87 W/m•K reported for ceramics produced by hot pressing of commercial ZrB_2 powder that contain the natural abundance of Hf. (19). As concluded by Lonergan (20,23), the thermal conductivity values reported for all ZrB_2 ceramics produced using commercial powders are affected by the natural abundance of Hf and are not representative of the intrinsic properties of ZrB_2.

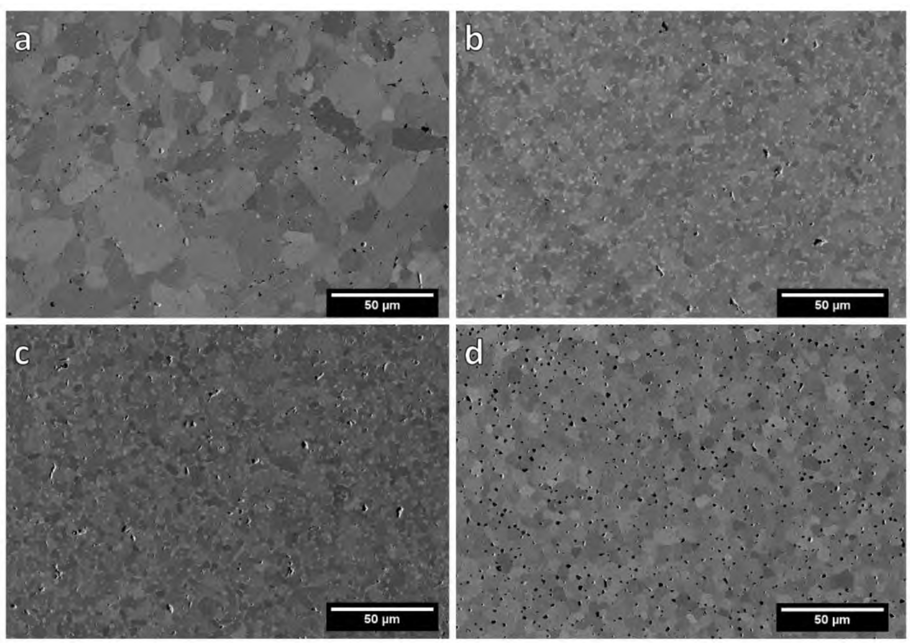

Figure 2: SEM micrographs of RHP ZrB_2 specimens showing a) nominally pure ZrB_2; and ZrB_2 with b) 3 at% TiB_2; c) 3 at% YB_2; and d) 3 at% HfB_2. The dark phase is porosity and void space resulting from grain pull-out during machining.

In the present study, the room temperature thermal conductivity of ZTB was 112 W/m•K, which is ~20% lower than ZB, but ~30% higher than CZB. The thermal conductivity of ZTB did not change as temperature was increased to 200°C. The addition of Y decreased the thermal conductivity of ZYB to 100 W/m•K, a decrease of nearly 30%. This larger decrease may be due to Y being a group III element, whereas the other

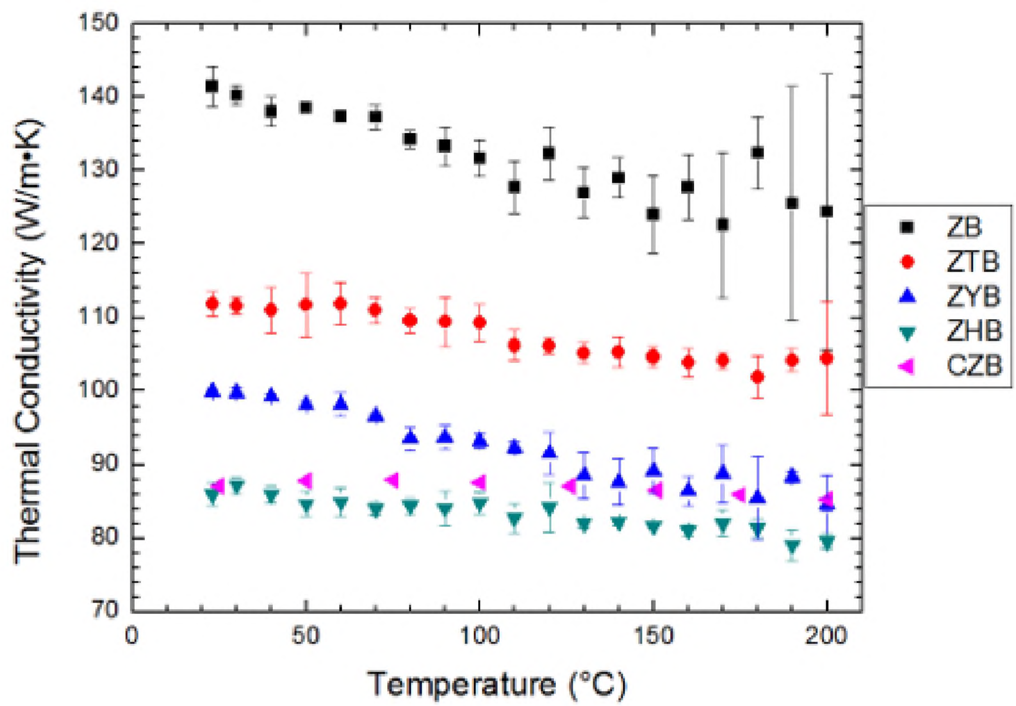

Figure 3: Thermal conductivity of ZrB_2 specimens along with values previously reported for hot pressed commercial ZrB_2 (CZB)(19) for comparison.

TMs studied are group IV elements resulting in a difference in valency, which may affect the resulting bond strength and, therefore, the phonon contribution to thermal conductivity. As with the addition of Ti, the addition of Y to ZrB_2 ceramics produced from commercial powder had no measurable effect on thermal conductivity due to the presence of the natural abundance of Hf (19). The thermal conductivity of ZYB decreased to 85 W/m•K at 200°C. The thermal conductivity decrease in the Y containing material may be due to valency or size differences between the Y and Zr. These differences may affect the resulting bond strength, thereby reducing the phonon contribution to thermal conductivity.

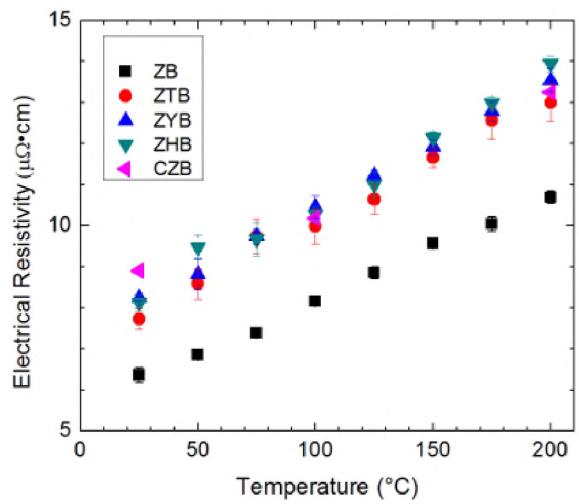

Figure 4: Electrical resistivity of ZrB_2 specimens along with values previously reported for hot pressed commercial ZrB_2 (CZB) (19) for comparison.

The addition of TMs increased the electrical resistivity of ZrB_2 ceramics (Figure 4). The room temperature electrical resistivity of ZB was 6.36 ± 0.18 μΩ•cm. The addition of the TMs increased electrical resistivity to the range of 7.73 to 8.24 μΩ•cm at room temperature. The room temperature electrical resistivity reported for CZB was 8.9 μΩ•cm. The similar values for the TM additions and CZB suggests that the electrical resistivity of ZrB_2 with low addition levels is controlled by the amount of the addition, not necessarily which TM is added. Zhou has shown that the transition metal diborides with the AlB_2 crystal structure share a similar electronic structure, and it is possible that these additions in ZrB_2 serve as electron scattering sites without appreciably altering the charge carrier density or electronic structure (29). The similarity of the electrical resistivity of the ZrB_2 ceramics containing TM additions suggests that the differences in thermal conductivity values for the ceramics containing additives are due to differences in phonon scattering since the electrical resistivities were are all shifted by the same amount compared to nominally pure ZrB_2.

4. SUMMARY

The effects of transition metal additions on the thermal properties of ZrB_2 ceramics were studied. Transition metal additions of 3 at% Ti, Y, or Hf were fully dissolved into the ZrB_2 lattice, forming single diboride phases. The room temperature thermal conductivity of ZB was 141 ± 3 W/m•K, which decreased when any of the TMs were added. The electrical resistivity of ZrB_2 was 6.36 ± 0.18 μΩ•cm at 25°C. Additives consistently increased the electrical resistivity, by about 30%. While previous studies showed that additions of titanium and yttrium had no apparent effect on thermal properties of ZrB_2, the results of the present study provide the first experimental evidence for the hypothesis that the effects of these specific transition metal additions were suppressed by the natural abundance of hafnium impurities in the ZrB_2 ceramics produced from commercial powders. Additionally, the use of reactive hot pressing of high purity starting materials resulted in some of the highest reported thermal conductivities for ZrB_2 ceramics. ZrB_2 based solid solutions offer a method to tailor material properties of boride ceramics in conjunction with or as an alternative to secondary phases.

ACKNOWLEDGEMENTS

This research was funded by the Office of Naval Research on contract N00014-16-1-2303. The authors wish to thank program manager Dr. Eric Wuchina for his guidance. The authors would like to acknowledge the assistance of the staff and use of equipment in the Advanced Materials Characterization Laboratory at Missouri S&T.

REFERENCES

1. Spear KE. Chemical Bonding in AlB_2-Type Borides. Journal of the Less-Common Metals. 1976;47:195-201.

2. Zapata-Solvas E, Jayaseelan D, Lin H-T, Brown P, Lee W. Mechanical properties of ZrB_2-and HfB_2-based ultra-high temperature ceramics fabricated by spark plasma sintering. Journal of the European Ceramic Society. 2013;33(7):1373-86.

3. Fridlender B, Neshpor VS, Ordan'yan SS, Unrod V. Thermal conductivity and thermal diffusivity of binary alloys of the ZrC-ZrB_2 system at high temperatures. Teplofizika Vysokikh Temperatur. 1979;17(6):1210-5.

4. Guo S, Nishimura T, Kagawa Y. Preparation of zirconium diboride ceramics by reactive spark plasma sintering of zirconium hydride–boron powders. Scripta Materialia. 2011;65(11):1018-21.

5. Clougherty EV, Kalish D, Peters ET. Research and developement of refractory oxidation-resistant diboride. Wright Patterson Air Force Base, 1968 1968. Report No.: AFMRL-TR-68-190.

6. Murata Y. Cutting tool tips and ceramics containing hafnium nitride and zirconium diboride. Google Patents; 1970.

7. Stucker B, Bradley W, Eubank P, Norasetthekul S, Bozkurt B. Zirconium diboride/copper EDM electrodes from selective laser sintering. Sol Free Fab Proc. 1997;1:257-66.

8. Kaji N, Shikano H, Tanaka I. Development of ZrB_2-graphite protective sleeve for submerged nozzle. Taikabutsu Overseas. 1994;14(2):39-43.

9. Opeka MM, Talmy IG, Zaykoski JA. Oxidation-based materials selection for 2000°C + hypersonic aerosurfaces: Theoretical considerations and historical experience. Journal of Materials Science. 2004;39(19):5887-904.

10. Glass D, editor Ceramic matrix composite (CMC) thermal protection systems (TPS) and hot structures for hypersonic vehicles. 15th AIAA International Space Planes and Hypersonic Systems and Technologies Conference; 2008.

11. Sonber J, Suri A. Synthesis and consolidation of zirconium diboride. Advances in Applied Ceramics. 2011;110(6):321-34.

12. Jung S-H, Oh H-C, Kim J-H, Choi S-C, Lee S-H, Kim H-D. Pretreatment of zirconium diboride powder to improve densification. Journal of Alloys and Compounds. 2013;548:173-9.

13. Sciti D, Silvestroni L, Medri V, Monteverde F. Sintering and densification mechanisms of ultra-high temperature ceramics. Ultra-High Temperature Ceramics: Materials for Extreme Environment Applications. 2014:112-43.

14. Zhang GJ, Deng ZY, Kondo N, Yang JF, Ohji T. Reactive hot pressing of ZrB_2–SiC composites. Journal of the American Ceramic Society. 2000;83(9):2330-2.

15. Zou J, Zhang GJ, Hu CF, Nishimura T, Sakka Y, Vleugels J, et al. Strong ZrB_2–SiC–WC ceramics at 1600° C. Journal of the American Ceramic Society. 2012;95(3):874-8.

16. Silvestroni L, Sciti D. Effects of MoSi2 additions on the properties of Hf- and Zr-B_2 composites produced by pressureless sintering. Scripta Materialia. 2007;57(2):165-8.

17. Zhang L, Pejaković DA, Marschall J, Gasch M. Thermal and Electrical Transport Properties of Spark Plasma-Sintered HfB_2 and ZrB_2 Ceramics. Journal of the American Ceramic Society. 2011;94(8):2562-70.

18. McClane DL, Fahrenholtz WG, Hilmas GE, Smith D. Thermal Properties of (Zr, TM)B_2 Solid Solutions with TM = Ta, Mo, Re, V, and Cr. Journal of the American Ceramic Society. 2015;98(2):637-44.

19. McClane DL, Fahrenholtz WG, Hilmas GE, Smith D. Thermal Properties of (Zr,TM)B_2 Solid Solutions with TM = Hf, Nb, W, Ti, and Y. Journal of the American Ceramic Society. 2014;97(5):1552-8.

20. Lonergan JM, McClane DL, Fahrenholtz WG, Hilmas GE. Thermal Properties of Hf-Doped ZrB_2 Ceramics. Journal of the American Ceramic Society. 2015;98(9):2689-91.

21. Yokota F, Morikawa H, Ishizuka T. Determination of impurities in zirconium disilicide and zirconium diboride by inductively coupled plasma atomic emission spectrometry. Analyst. 1994;119(5):1023-7.

22. Neuman E, Fahrenholtz W, Hilmas G. Factorial design to minimize residual oxygen in reaction hot-pressed zirconium diboride. International Journal of Applied Ceramic Technology. 2017;14(4):636-43.

23. Lonergan JM, Fahrenholtz WG, Hilmas GE. Zirconium Diboride with High Thermal Conductivity. Journal of the American Ceramic Society. 2014;97(6):1689-91.

24. Chase M. Thermochemical Tables. 4 ed. Woodbury, New York: American Institute of Physics for the National Institute of Standards and Technology; 1998.

25. International A. Standard Test Method for Measuring Resistivity and Hall Coefficient and Determining Hall Mobility in Single-Crystal Semicondcuctors. West Conshohocken, PA: ASTM International; 2016.

26. Andrievskii RA, Korolev LA, Klimenko VV, Lanin AG, Spivak II, Taubin IL. Effect of zirconium carbide and carbon additions on some physicomechanical properties of zirconium diboride. Soviet Powder Metallurgy and Metal Ceramics. 1980;19(2):93-4.

27. Lonergan JM. Thermophysical Properties of Reaction Processed Zirconium Diboride [Publication]: Missouri University of Science and Technology; 2014.

28. Harrington GJK, Hilmas GE. Thermal Conductivity of ZrB_2 and HfB_2. In: Fahrenholtz WG, Wuchina EJ, Lee WE, Zhou W, editors. Ultra-High Temperature Ceramics: Materials for Extreme Environment Applications. 1 ed. Hoboken, New Jersey: John Wiley& Sons; 2014. p. 197-235.

29. Zhou Y, Wang J, Li Z, Zhan X, Wang J. First-Principles Investigation on the chemical bonding and intrinsic elastic properties of transition metal diborides TMB_2 (TM=Zr, Hf, Nb, Ta, and Y). In: Fahrenholtz WG, Wuchina EJ, William E L, Zhou Y, editors. Ultra-High Temperature Ceramics. 1 ed. Hoboken, New Jersey: John Wiley & Sons; 2014. p. 60-82.

II. MEASUREMENT OF THE MELTING TEMPERATURE OF ZrB_2 AS DETERMINED BY LASER HEATING AND SPECTROMETRIC ANALYSIS

Austin D. Stanfield[1], Dario Manara[2,3], Davide Robba[2],

Gregory E. Hilmas[1], William G. Fahrenholtz[1]

[1] Deparment of Materials Science and Engineering, Missouri University of Science and Technology, Rolla, MO 65409

[2] Safety of Nuclear Fuel Unit, European Commission
Joint Research Centre, Karlsruhe, BW D-76125

[3] Sustainable Transport Unit, European Commission
Joint Research Centre, Ispra, VA I-21027

ABSTRACT

The melting temperatures of two different ZrB_2 ceramics were studied using laser induced melting. ZrB_2 having a low Hf content, produced by reaction hot pressing, had a melting temperature of 3546 K and a commercial grade ZrB_2 had a melting temperature of 3553 K. Uncertainty of the temperature measurements was 1% of the absolute temperature, or ~35 K for both materials based upon 2-sigma and a 95% confidence interval. While these values were consistent with the previously reported ZrB_2 melting temperature of 3518 K, this study was able to measure T_m with less uncertainty than previous studies (± 45 K). Furthermore, this study assessed the effect of Hf content on melting temperature, finding that melting temperature did not change significantly for hafnium contents of 1.75 at% to 0.01 at%. This study also measured a normal spectral

emissivity of 0.34 for ZrB_2 at 3000 K. The emissivity decreased to 0.28 at the melting temperature, then stabilized at 0.30 in a liquid phase.

1. INTRODUCTION

Ultra-high temperature ceramics (UHTCs) are candidate materials for use in extreme environments such as those demanded by next generation hypersonic flight vehicles and nuclear reactors (1,2). UHTCs are defined by melting temperatures exceeding 3273 K and are generally comprised of borides, carbides, and nitrides of the transition metals. In particular, ZrB_2 based ceramics are of interest due to their high thermal conductivity (up to ~140 W/m•K)(3), strength at elevated temperatures (675 MPa at 1873 K)(4), and melting temperature (3523 K)(5). ZrB_2 is an important topic of investigation for the detailed analysis of severe accidents in nuclear power plants. In particular, in boiling water reactors moderated with the help of B- rich blades, boron can interact with the Zr-rich liquid coming from the damaged cladding if temperatures beyond 2000 K are produced during an accident (6). Moreover, ZrB_2 has been suggested as a suited material for a moderation layer to improve the safety performance of sodium cooled fast nuclear reactors of the Fourth Generation (7). Knowledge about the refractory properties of zirconium diboride is paramount also in view of this kind of applications. However, the extreme conditions needed to melt UHTCs make it difficult to perform reliable measurements of fusion/solidification temperatures due to problems such as reactivity with containers, heat losses, volatility, decreased strength, and reliable temperature measurements.

One of the first reliable test methods was devised in 1928 by Pirani and Alterthum and was used in 1931 by Agte to measure the melting temperature of ZrB_2 to be 3323 K (8,9). This method heats the material resistively and temperature is read by a pyrometer sighted in a cylindrical hole that is machined into the specimen (i.e., simulating a blackbody cavity). The specimen is then monitored for liquid formation by detecting the time point and temperature at which the hole is filled with liquid mass. Using this method, Rudy published a comprehensive study of the melting temperatures of transition metal borides (5). As part of this study, Rudy measured the melting temperature of ZrB_2 to be 3518 ± 25 K. While early pyrometers had limited time resolution, Rudy was able to achieve a relatively small pyrometer temperature uncertainty of 25 K by calibrating the pyrometers against known standards and generally accepted melting temperatures for several different materials. Unfortunately, compositional purity of Agte and Rudy's specimens are unknown. In fact, Agte only affirms that the studied phase is a zirconium boride of unknown stoichiometry as the compositional analysis was flawed, and Rudy describes generic powder preparation without providing details on any reported compositions (5,9). Some additional sources of error in these types of temperature measurements are discussed in the next sections of this paper.

The present research is focused on the observation of the melting behaviour of two ZrB_2 specimens in which the formation of liquid has been induced by laser heating under a controlled inert atmosphere. In particular, the current experiments are used for the measurement, by multi-channel spectro-pyrometry, of the liquid mass temperature evolution and the determination of its melting and solidification points. Several other refractory systems have been studied by the laser melting technique such as uranium carbides, uranium oxides, plutonium oxides, uranium nitrides, zirconium carbides, as well as the highest known melting temperature materials $(Ta_{1-X}Hf_X)C$ (10-17). The phase transition data collected in these studies were in some cases in agreement with literature values. In other cases, discrepancies were observed (e.g.: CaO, CeO_2, UO_2, PuO_2 and NpO_2) (10,17-19). Such discrepancies were shown to be due to high-temperature contamination and/or incongruent vaporisation occurring in earlier experimental approaches. The laser heating technique used here limits sample-containment interactions and allows for melting of the material under a largely controlled atmosphere, thus circumventing issues that had been encountered with more traditional heating methods. Therefore, this approach has allowed for a reassessment of the melting behaviour of several materials, in some cases by confirming earlier data with a better accuracy, and in other cases by showing that the material's chemical instability had led to large errors, perhaps by hundreds of degrees, in the earlier determination of the melting point, especially in chemically reactive and highly volatile compounds.

The essential goal of the present research study consists of comparing the melting /solidification behaviour observed in laser-heated ZrB_2 samples with earlier data of same basic composition determined with more traditional heating approaches.

Moreover, two types of ZrB_2 are investigated here for the first time at temperatures close to the melting point. The behavior of commercial grade ZrB_2 containing standard Hf-rich zirconium is compared with the behavior of low-Hf ZrB_2 produced by reactive hot pressing of high-purity Zr in the form of ZrH_2 directly with boron. This exercise is useful in determining whether the employment of high-purity, costly zirconium in the compound can have any significant effect on the material stability under the extreme conditions produced around its melting temperature.

2. PROCEDURE

Two different ZrB_2 ceramics were prepared by hot pressing. Commercial ZrB_2 (Grade B; H.C. Starck Inc., Newton, MA, USA) with a Hf content of 1.75 at%, henceforth referred to as CZB, was hot pressed (Model HP20-3060-20; Thermal Technology, Santa Rosa, CA, USA) by a 50 K/min ramp to 2373 K where it was held for 15 minutes. A mild vacuum (~10 Pa) was utilized until 1873 K at which point a flowing Ar atmosphere was used. A high purity ZrB_2 with a Hf content of 0.01 at%, henceforth referred to as ZB, was synthesized by reactive hot pressing ZrH_2 (<45 ppm Hf; CRS Chemicals, Canoga Park, CA, USA) and B (Grade SP-95; SB Boron Products, Bellwood, IL, USA) as described in more detail in Stanfield et al. (20). A 3 wt% super addition of phenolic resin (GP 2074, Georgia Pacific, Atlanta, GA, USA) with a char yield of ~50 wt% carbon, was utilized to react with and remove surface oxides on particles. Several isothermal holds were used to char the phenolic resin, promote the formation of ZrB_2, and reduce surface oxides (21-23). Following a 50 K/min ramp rate, densification occurred at 2373 K under 32 MPa and flowing Ar.

Surface characterization was performed on the unpolished melt surfaces with a TESCAN VEGA (Tescan Orsay Holdings, Kohoutovice, CZE) scanning electron microscope (SEM). Backscatter electron (BSE) micrographs were acquired with a 20 kV accelerating voltage, and electron dispersive spectroscopy (EDS) was performed under the same conditions. Computerized image analysis (ImageJ; National Institutes of Health, Bethesda, MD, USA) was used to calculate minimum and maximum Feret diameter of grains. Oxygen analysis was measured by the inert gas fusion method with a TS500 (LECO, St. Joseph, MI, USA)

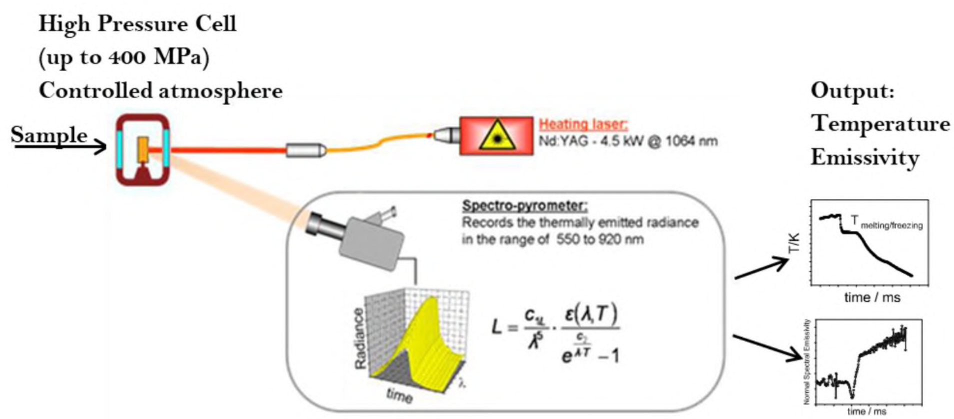

Figure 1: Schematic representation of the FLF-LHASA laser heating facility [after De Bruycker et al. 2011] (9).

The Laser Heating and Spectrometric Analysis (LHASA) technique developed at JRC Karlsruhe (see Figure 1) was used to analyze the melting behavior of ZrB_2 samples. A disk-shaped specimen of about 7 mm in diameter and 3 mm-thick was mounted in a controlled-atmosphere autoclave and heated by a Nd:YAG CW Laser (HLD4506, TRUMPF, Schramberg, DEU) with a 5 mm diameter spot size. Such a continuous-wave laser beam can be chopped into short pulses (up to 1 ms), with a maximum power of 4.5 kW. Pulse durations of approximately 1 s were sufficient to stabilize a large spot of liquid ZrB_2 in these experiments. After the end of each laser pulse, the liquid naturally cooled back to room temperature. Shorter pulses were used in the past for the investigation of nano-structured and ultra-refractory materials with higher volatility, for which it was necessary to limit to a minimum the exposure to extreme temperatures (14-16,18). The current ZrB_2 samples were heated under pressurized Ar at 300 kPa. In this way, the overpressure, inert atmosphere and relatively short exposure to high temperature all contributed to minimizing the non-congruent vaporization and any chemical reaction between the condensed sample and the gas phase.

Thermal radiation pyrometers were used to measure the radiance, L_{ex}, of the specimens. This is the electromagnetic radiation power density per unit surface area, wavelength, and solid angle emitted by the specimen at a given temperature (24). It is related to the specimen surface temperature T through a modified form of Planck's function:

$$L_{ex} = \frac{L_\lambda}{c_1} = \frac{1}{\lambda^5} \cdot \frac{\varepsilon_\lambda(T)}{e^{\frac{c_2}{\lambda \cdot T}} - 1} \tag{1}$$

where L_λ is the thermal radiative power, ε_λ is the temperature dependent spectral emissivity, $c_1 = 2 \cdot h \cdot c_0^2$ is the first radiation constant and $c_2 = h \cdot c_0 \cdot k_B = 14{,}388$ µm K is the second radiation constant, c_0 is the speed of light in vacuum, h is Planck's constant, and k_B is Boltzmann's constant. The spectral emissivity takes into account the fact that a real body will thermally radiate, at a given wavelength and temperature, only a fraction equal to ε_λ of the power emitted by an ideal blackbody at the same temperature. Therefore, ε_λ takes values between 0 and 1, whereby 1 corresponds to the ideal blackbody case for which Planck's law was derived. Since pyrometers in the present work were always set up near normal with respect to the specimen surface, the angle dependence of ε_λ was not considered, and 'emissivity' will always refer to normal spectral emissivity

(NSE). The NSE must be determined in order to convert, through equation (1) and a pyrometer calibration procedure, L_{ex} into absolute temperature T.

The specimen temperature was detected using a fast pyrometer calibrated against standard lamps up to 2500 K at λ = 655 nm. An additional, 256-channel radiance spectro-pyrometer operating between 515 nm and 980 nm was employed to measure the thermal radiation emission of the specimen, which yields essential information on some high-temperature optical properties of the material, and in particular on the normal spectral emissivity and its temperature dependence. Determination of the NSE is possible by doing a non-linear fit of the thermal emission spectrum with Equation 1, T and ε_λ being the only two dependent variables (grey-body approximation). This approach has been demonstrated to be acceptably accurate in insulating refractory materials (25). It is also considered to be a valid approach for conducting and semi-conducting materials (26).

The temperature-time curve of the laser-heated specimen as a function of time, commonly referred to as a ‘thermogram’, is used to perform thermal analysis. Inflections or thermal arrests in the thermograms give information related to phase transitions (e.g., solidus, liquidus and isothermal phase transformations). However, the intense laser irradiation (several kW/cm^2) of the laser pulse induces a rapid temperature increase (several thousand K/s), which complicates detection of phase transitions on the heating leg of the thermograms. Inflections and thermal arrests are more easily detected during natural cooling of the liquid sample surface. The current analysis was, therefore, performed only during the cooling leg of the thermograms.

Besides being necessary to the NSE determination, direct spectral analysis of L_{ex} emitted by the hot specimen also permits an in-situ study of some optical properties. This constitutes a further supporting tool for identification of high-temperature phenomena, such as phase transitions, chemical reactions between condensed material and the gas phase, or segregation effects.

The most significant uncertainty sources related to the laser heating and multi-channel pyrometry have been combined, according to the independent error propagation law (Equation 2) (27), and expanded to yield relative temperature uncertainty bands corresponding to 2 standard deviations (k = 2 coverage factor). These uncertainty components stem from our current temperature scale definition δT (i.e. the uncertainty in the pyrometer calibration), the NSE assessment $\delta T_{\varepsilon\lambda}$ and the experimental data scatter on the current phase transition radiance temperature data $\delta T_{\lambda m}$, the latter being the main source of uncertainty:

$$\delta T_m = \sqrt{\delta T^2 + \delta T_{\varepsilon\lambda}{}^2 + \delta T_{\lambda m}{}^2} \tag{2}$$

The resulting uncertainty is of the order of 30 K at 3000 K with calculated uncertainty values reported for each measurement.

3. RESULTS AND DISCUSSION

Figure 2 shows the as-melted surface of ZB. The fusion zone (FZ) at the center of the micrograph is characterized by a central solidified melt pool surrounded by large ZrB_2 needles. These needles have an aspect ratio of approximately 7:1 with the largest being ~700 μm long. Figure 2B shows details of the FZ where ZrB_2 is the dark phase, and lighter secondary phase is present. Qualitative EDS spot analysis only detected significant amounts of zirconium and oxygen in all light phases. However, due to the small feature size and high accelerating voltage, quantitative analysis is not reported. Trace amounts (<1%) of Ti, W and Sc were also detected. Post-melting oxygen content as measured by the gas fusion method was 1.7 wt% which was similar to the oxygen content of 1 wt% before melting. The similar oxygen contents before and after melting are an indication of the ability of the experimental technique to limit environmental contamination. For concision, the oxygen-containing phase will simply be referred to as an oxide. Two oxide morphologies were present in this region. The first was located at grain boundaries, which was likely the result of preferential exclusion of oxygen from solidifying ZrB_2 grains. Most probably, the oxygen enriched liquid became trapped at the impingement of grains until it solidified at a lower temperature. The second morphology was inclusions within ZrB_2 grains. Figure 2 presents these inclusions in greater detail and shows that the oxide morphology is consistent with nucleation and grain growth behavior. Due to high cooling rates in this region, conditions may not have been favorable for homogeneous nucleation of crystallites, resulting in the formation of oxide crystals at high energy sites such as grain boundaries. The oxide crystals then grew as the temperature decreased. Several oxide crystals were present within the grains, but these crystals likely nucleated at lower temperatures as they are smaller and would have less time to grow before solidification. Voids were also present at triple junctions between needles suggesting that the liquid ZrB_2 was less dense than the crystalline ZrB_2. Rounded pores and surface erosion were present due to the volatilization of material at extreme temperatures.

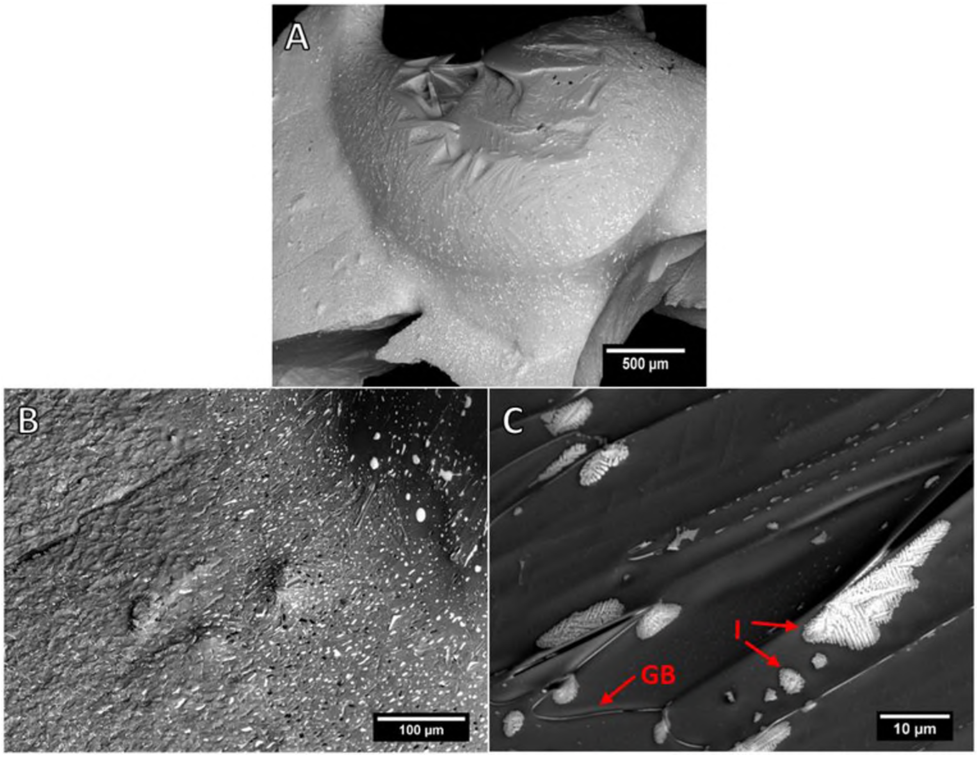

Figure 2: Large grains are visible on the surface of ZB after melting (A). An O rich phase was detected in B and C as inclusions (I) and at grain boundaries (GB).

Moving towards the perimeter of the FZ, ZrB_2 grains were smaller and the oxide inclusions had a spherical morphology. This oxide morphology may have formed while the ZrB_2 was melted, but the oxide may not have been fully melted due to a significantly lower thermal conductivity. These spherical inclusions were primarily found inside the ZrB_2 grains, while an oxygen-rich secondary phase was also found at the grain boundaries. Rounded pores were present in this region and were likely due to the volatilization of material at elevated temperature.

Figure 3 reports the cooling portions of the thermograms where thermal analysis was performed. The highest-temperature part of the thermograms recorded on laser-heated CZB and ZB present important differences, both in terms of the maximum

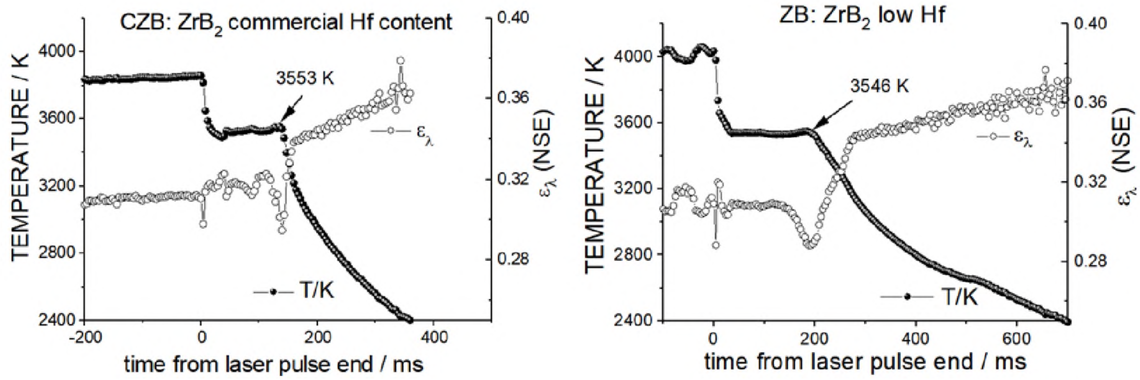

Figure 3: Thermograms (black circles) and normal spectral emissivity (white circles) recorded on laser-heated CZB (left) and ZB (right). Note that ZB was heated to a higher temperature resulting in a larger amount of liquid, hence a longer solidification plateau.

temperature reached and the thermal stability. These discrepancies can be attributed to two main causes. First, the Nd:YAG laser power density is not stable at the peak power (in this case around 8 kW/cm^2) of the pulse, therefore the maximum temperature reached and its stability differ between different experiments. Second, the temperature signals in the highest temperature part of the thermograms were recorded on a liquid surface, in which significant and uncontrolled morphology fluctuations were induced by capillary forces interacting with the random features of the underlying solid. For these reasons, also the maximum temperatures reached in the two cases differ by more than 100 K, as CZB was heated to around 3850 K, whereas liquid ZB reached more than 4000 K. Therefore, a larger liquid mass was also produced in ZB and the correspondingly larger heat content explains the slower cooling of this specimen compared to CZB. Independently, the normal spectral emissivity trends were very close in the two cases, and the solidification temperatures were characterized in both cases by similar thermal arrests where the temperature plateaued. The last remark is of some interest, because it indicates that the previous thermal history of the material has no significant effect on its solidification behaviour. This was expected because the congruent solidification temperature is an invariant point in the Zr-B binary phase diagram (5). Actually, the solidification arrest appears to be isothermal, although the freezing plateau displays, in both cases, some undercooling of the liquid below the equilibrium transition temperature, albeit more marked in CZB. Metastable undercooling of the liquid was expected based on the large cooling rates, as discussed in previous publications using solidification models (18). In such a situation, the equilibrium freezing point can be taken as the highest temperature point at the end of the solidification plateau, indicated by arrows in Figure 3. Because the solidification transition results, with good approximation, in an isothermal temperature plateau and since SEM EDS analysis showed that the re-frozen material composition was globally the same as the initial one, the present results confirm that ZrB_2 melts congruently. This is in agreement with existing thermodynamic optimization of the Zr-B phase diagram, and other reported Zr-B phase diagrams (5,28,29). Hence, the detected solidification temperatures can be considered the same as the melting ones, at least within the instrumental uncertainty. These melting temperatures were 3553 K for CZB and 3546 K for ZB.

Uncertainty in temperature measurements was ~1% of the absolute temperature based upon 2-sigma and a 95% confidence interval. Therefore, the uncertainty of melting temperatures was ~35 K for both compositions. While both melting temperatures agreed with melting temperatures from Rudy and Rogl, the uncertainty in the present technique was greater than the Pirani-Alterthum method used by Rudy (5,30). However, when publishing the updated Zr-B binary phase diagram, Rogl utilized Rudy's ZrB_2 melting study, and in doing so referenced the reproducibility (± 18 K) as the uncertainty in temperature measurement instead of the full uncertainty of ± 25 K stated by Rudy. While Rudy claimed a 95% confidence level, he also suggested that the uncertainty was an estimate and not an exact value. As such, Rudy's uncertainty was recalculated using the same error propagation methodology as the present study (Equation 2) and Rudy's listed sources of error as follows: reproducibility (18 K), visual matching of test and calibration pyrometer (1.7 K), hysteresis of pyrometer (1.8 K), uncertainty in certified pyrometer (maximum of 40 K at 4000 K), uncertainty in tungsten ribbon lamp (2 K at 2300 K), and the limited resolution of the ten-turn pot in the pyrometer (3 K). The corrected uncertainty value for Rudy's measurement was ± 45 K, which makes the measured ZrB_2 melting temperature 3518 ± 45 K. Similarly, the HfB_2 melting temperature, as measured by Rudy, can be corrected to 3653 ± 45 K. Besides the slightly improved accuracy, the present results obtained by laser heating confirm, within the experimental uncertainty, the melting point of ZrB_2 that was measured several decades ago with techniques that today are seen as more traditional. They reinforce the credibility of earlier experimental data. Moreover, the relatively good agreement between the current data and earlier ones confirms that ZrB_2 melts congruently with limited non-congruent vaporization and limited containment-sample chemical interaction. These factors have been observed (8, 9) to cause significant discrepancies between phase transition data measured with laser heating and more traditional techniques.

The Hf contents measured by inductively coupled plasma mass spectroscopy were 0.01 at% for ZB and 1.75 at% for CZB (31). Thermodynamics dictate that the melting temperature of a solution of two components with infinite solid solubility in each other will be between the melting temperatures of the pure compounds (32). While it is difficult to draw statistically significant conclusions from this small range of Hf contents, the melting temperatures follow an expected trend as a simple rule of mixtures would predict a T_m increase of only 3 K. Alternatively, if eutectic behavior were exhibited, it would have resulted in a significant decrease in T_m with increasing Hf content as liquid would form at the eutectic temperature. Because no such decrease was observed, this study is consistent with ideal solid solution between ZrB_2 and HfB_2. It is noteworthy that, according to the present data, the melting point increase due to the presence of abundant Hf impurities in commercial ZrB_2 in the mixed diboride system is limited to a few K, corresponding to the amount predicted by the ideal solution model. Since such a temperature increase is well within the experimental uncertainty, one can infer that negligible improvement in the ZrB_2 structural resistance to elevated temperatures occurs when commercial ZrB_2 is replaced by more expensive ultra-pure ZrB_2.

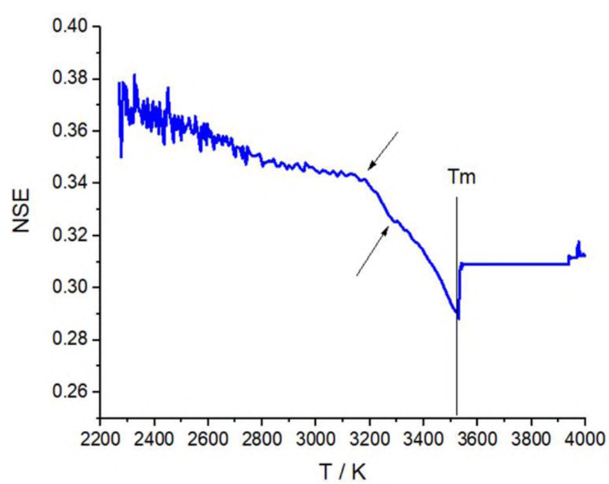

Figure 4: The average normal spectral emissivity (NSE) of ZB and CZB measured in this work as a function of temperature. In high-temperature values of liquid phase NSE large fluctuations are averaged out.

The spectral emissivity data are novel as emissivity has never before been measured near the melting point of ZrB_2, at least not to the authors' knowledge. Both compositions had the same emissivity profile within the experimental uncertainty. An average profile is plotted in Figure 4. After averaging random fluctuations, the NSE measured here in the visible – near infrared range was approximately constant and equal to 0.31 between the melting temperature (in average 3549 K) and the maximum temperature measured, around 4000 K. Upon cooling the liquid, a kink was observed upon freezing, were the NSE decreased to 0.28 and then started increasing again. Discontinuous behavior between the liquid and the solid has been observed for several other materials, and is attributable to the electronic structure of the disordered liquid as opposed to solid crystal's band structure. From the solidification temperature downward, the emissivity increased linearly from 0.28 at to 0.32 at approximately 3200 K, indicated by an arrow in Figure 4. At lower temperatures, the emissivity increased more rapidly with the change in temperature to 0.34 at 3160 K, indicated by another arrow. From this more abrupt NSE change, one can assume the existence of an optical transition in zirconium diboride. This alleged optical transition would certainly be a higher order thermodynamic transition, as no thermal arrests or inflections were seen in the thermograms in the corresponding temperature range. Even optically, the transition was quite soft, as the NSE increase from 0.32 to 0.34 was similar in magnitude to the instrumental uncertainty. The relative uncertainty of the current spectral emissivity values was on the order of ± 5% (19). Nonetheless, this phenomenon was obvious from the data, which merits further investigation. Alternatively, this sudden increase may be due to significant coarsening of grains at this temperature, which increased the specimen surface roughness. Cooling further, emissivity increased linearly with temperature from 0.34 at 3160 K to 0.37 at 2200 K. A further increase up to an NSE value of 0.4 can be supposed by comparing the current data with other literature values. For an opaque material holds the equation (24)

$$\varepsilon_\lambda = 1 - \rho_\lambda \tag{3}$$

where ρ_λ is the normal spectral reflectivity. Obviously, similar equations hold for the total normal and the hemispherical emittances and reflectances. The present data can be compared with other investigations dealing with the normal spectral reflectivity or reflectance. In performing such comparison, the assumption was made that the emittance data from the present study coincide with the real material emissivity insofar as the shallow liquid or rapidly solidifying ZrB_2 layer can be considered as an ideally flat and homogeneous surface as emissivity and emittance in theory coincide in perfectly homogeneous and opaque materials. The only literature data relative to pure ZrB_2 are those measured by Mercatelli et al. (33). Those authors measured the total hemispherical emittance of ZrB_2 up to 1450 K and the total hemispherical reflectance in the ultraviolet–visible–near-infrared range at room temperature. Technically, neither of these datasets can be directly compared with the present NSE results. However, a qualitative comparison can help verify the likelihood of the high-temperature emissivity values observed in this work. Mercatelli et al.'s analysis shows that the total hemispherical emittance of ZrB_2 at 1450 K is around 0.45, whereas a value between 0.5 and 0.6 can be inferred from the total hemispherical reflectance through Equation 3 at room temperature These values seem to be at least compatible with the current data, considering the thermal trend observed in Figure 5.

4. CONCLUSIONS

Laser-induced melting and optical pyrometry were employed to measure the melting temperature and normal spectral emissivity of ZrB_2 ceramics. The investigation led to the following conclusions:

- Specially synthesized ZrB_2 with a Hf content of 0.01 at% had a melting temperature of 3546 K while commercial ZrB_2 with a Hf content of 1.75 at% displayed a melting temperature of 3553 K.
- These results are in line with 3518 K ± 45 K measured in the 1960's with more traditional heating methods, confirming that ZrB_2 melts congruently and with limited non-congruent vaporization and limited containment-sample chemical interaction.
- The uncertainty in both melting temperatures was ± 35 K, which is less than the uncertainty in previous studies.
- The melting/solidification temperature increase with Hf content is consistent with the ideal solution model between ZrB_2 and HfB_2. Since such a temperature increase is well within the experimental uncertainty, no significant increase was present in the ZrB_2 melting temperature when commercial Zr is replaced by rare and expensive ultra-pure Zr.
- The emissivity of ZrB_2 was determined to be ~0.34 at 3000 K, decreasing to 0.28 at the melting temperature, and then stabilizing at 0.30 in the liquid phase.

Besides confirming earlier data and producing new ones, the present study shows that laser melting is a suited method for accurate T_m determination and emissivity measurements at elevated temperatures. It can enable further investigations including studies of phase equilibria and elevated temperature optical properties for materials with melting temperatures above 3000 K.

ACKNOWLEDGMENTS

This research was funded by the Office of Naval Research (N00014-16-1-2303) and the National Science Foundation (CMMI-1902069). The authors wish to thank ONR program manager Dr. Eric Wuchina for his guidance. They acknowledge prof. R. Konings (JRC Karlsruhe) for his advice.

REFERENCES

1. Opeka MM, Talmy IG, Zaykoski JA. Oxidation-based materials selection for 2000°C + hypersonic aerosurfaces: Theoretical considerations and historical experience. J Mater Sci [Internet]. 2004;39(19):5887–904. Available from: http://dx.doi.org/10.1023/B:JMSC.0000041686.21788.77

2. Evitts LJ, Middleburgh SC, Kardoulaki E, Ipatova I, Rushton MJD, Lee WE. Influence of boron isotope ratio on the thermal conductivity of uranium diboride (UB_2) and zirconium diboride (ZrB_2). J Nucl Mater [Internet]. 2020;528:151892. Available from: http://www.sciencedirect.com/science/article/pii/S0022311519307093

3. Lonergan JM, Fahrenholtz WG, Hilmas GE. Zirconium Diboride with High Thermal Conductivity. J Am Ceram Soc [Internet]. 2014;97(6):1689–91. Available from: http://dx.doi.org/10.1111/jace.12950

4. Zou J, Zhang G, Hu C, Nishimura T, Sakka Y, Vleugels J, et al. Strong ZrB_2–SiC–WC ceramics at 1600° C. J Am Ceram Soc. 2012;95(3):874–8.

5. Rudy E, Windisch S. Ternary Phase Equilibria in Transition Metal-Boron-Carbon-Silicon Systems Part I. Binary Phase Systems. AFML-TR-65-2. 1966;VIII:34.

6. Pshenichnikov A, Yamazaki S, Bottomley D, Nagae Y, Kurata M. Features of a control blade degradation observed in situ during severe accident conditions in boiling water reactors. J Nucl Sci Technol. 2019;56(5):440–53.

7. Merk B, Weiß FP. A moderation layer to improve the safety behavior of sodium cooled fast reactors.

8. Pirani M, Alterthum H. Method for the determination of the melting point of metals which fuse at high temperatures. Z Elektrochem Angew Phys Chem. 1923;29:5–8.

9. Agte C, Moers K. Methoden zur reindarstellung hochschmelzender Carbide, Nitride und Boride und beschreibung einiger ihrer eigenschaften. Zeitschrift für Anorg und Allg Chemie. 1931;198(1):233–75.

10. Utton CA, De Bruycker F, Boboridis K, Jardin R, Noel H, Guéneau C, et al. Laser melting of uranium carbides. J Nucl Mater. 2009;385(2):443–8.

11. Manara D, Ronchi C, Sheindlin M, Lewis M, Brykin M. Melting of stoichiometric and hyperstoichiometric uranium dioxide. J Nucl Mater. 2005;342(1–3):148–63.

12. De Bruycker F, Boboridis K, Manara D, Pöml P, Rini M, Konings RJM. Reassessing the melting temperature of PuO_2. Mater today. 2010;13(11):52–5.

13. De Bruycker F, Boboridis K, Pöml P, Eloirdi R, Konings RJM, Manara D. The melting behaviour of plutonium dioxide: A laser-heating study. J Nucl Mater. 2011;416(1–2):166–72.

14. Nunez UC, Prieur D, Bohler R, Manara D. Melting point determination of uranium nitride and uranium plutonium nitride: A laser heating study. J Nucl Mater. 2014;449(1–3):1–8.

15. Jackson HF, Jayaseelan DD, Lee WE, Reece MJ, Inam F, Manara D, et al. Laser melting of spark plasma-sintered zirconium carbide: thermophysical properties of a generation IV very high-temperature reactor material. Int J Appl Ceram Technol. 2010;7(3):316–26.

16. Cedillos-Barraza O, Grasso S, Al Nasiri N, Jayaseelan DD, Reece MJ, Lee WE. Sintering behaviour, solid solution formation and characterisation of TaC, HfC and TaC–HfC fabricated by spark plasma sintering. J Eur Ceram Soc. 2016;36(7):1539–48.

17. Cedillos-Barraza O, Manara D, Boboridis K, Watkins T, Grasso S, Jayaseelan DD, et al. Investigating the highest melting temperature materials: A laser melting study of the TaC-HfC system. Sci Rep [Internet]. 2016;6(1):37962. Available from: https://doi.org/10.1038/srep37962

18. Manara D, Böhler R, Boboridis K, Capriotti L, Quaini A, Luzzi L, et al. The melting behaviour of oxide nuclear fuels: effects of the oxygen potential studied by laser heating. Procedia Chem. 2012;7:505–12.

19. Manara D, Böhler R, Capriotti L, Quaini A, Bao Z, Boboridis K, et al. On the melting behaviour of calcium monoxide under different atmospheres: A laser heating study. J Eur Ceram Soc [Internet]. 2014;34(6):1623–36. Available from: https://www.scopus.com/inward/record.uri?eid=2-s2.0-84894906725&doi=10.1016%2Fj.jeurceramsoc.2013.12.018&partnerID=40&md5=7c4afced7776e742160e5363ff252fbd

20. Stanfield AD, Hilmas GE, Fahrenholtz WG. Effects of Ti, Y, and Hf additions on the thermal properties of ZrB_2. J Eur Ceram Soc [Internet]. 2020; Available from: https://www.scopus.com/inward/record.uri?eid=2-s2.0-85085092015&doi=10.1016%2Fj.jeurceramsoc.2020.04.011&partnerID=40&md5=0312c793c57d6e7402a378ed3cc49c81

21. Chamberlain AL, Fahrenholtz WG, Hilmas GE. Reactive hot pressing of zirconium diboride. J Eur Ceram Soc. 2009;29(16):3401–8.

22. Zhu S, Fahrenholtz WG, Hilmas GE, Zhang SC. Pressureless sintering of carbon-coated zirconium diboride powders. Mater Sci Eng A [Internet]. 2007;459(1–2):167–71. Available from: http://www.sciencedirect.com/science/article/pii/S0921509307004480

23. Zhang X, Hilmas GE, Fahrenholtz WG. Synthesis, densification, and mechanical properties of TaB_2. Mater Lett [Internet]. 2008;62(27):4251–3. Available from: http://www.sciencedirect.com/science/article/pii/S0167577X08005880

24. DeWitt DP, Nutter GD. Theory and practice of radiation thermometry. John Wiley & Sons; 1988.

25. Böhler R, Welland MJ, Prieur D, Cakir P, Vitova T, Pruessmann T, et al. Recent advances in the study of the UO_2–PuO_2 phase diagram at high temperatures. J Nucl Mater. 2014;448(1–3):330–9.

26. Neuer G, Fiessler L, Groll M, Schreiber E. Critical analysis of the different methods of multiwavelength pyrometry. Temp its Meas Control Sci Ind. 1992;6(1):787–9.

27. Manara D, Sheindlin M, Heinz W, Ronchi C. New techniques for high-temperature melting measurements in volatile refractory materials via laser surface heating. Rev Sci Instrum. 2008;79(11):113901.

28. Portnoi KI, Romashov VM, Vyroshina LI. Phase diagram of the zirconium-boron system. Poroshkoviaia Met. 1970;10(7):68–71.

29. Fischer E. NUCLEA Thermodynamic Database [Internet]. Saint-Paul-lès-Durance: Institut de Radioprotection et Sûreté Nucléaire; Available from: http://thermodata.online.fr/nuclea

30. Rogl P, Potter PE. A critical review and thermodynamic calculation of the binary system: Hafnium-Boron. Calphad [Internet]. 1988;12(3):207–18. Available from: http://www.sciencedirect.com/science/article/pii/0364591688900016

31. Lonergan JM, McClane DL, Fahrenholtz WG, Hilmas GE. Thermal Properties of Hf-Doped ZrB_2 Ceramics. J Am Ceram Soc [Internet]. 2015;98(9):2689–91. Available from: http://dx.doi.org/10.1111/jace.13717

32. Gaskell DR. Introduction to the thermodynamics of materials. 5th ed. New York: Taylor & Francis; 2008. xv, 618 p.

33. Mercatelli L, Sani E, Jafrancesco D, Sansoni P, Fontani D, Meucci M, et al. Ultra-refractory diboride ceramics for solar plant receivers. Energy Procedia. 2014;49:468–77.

III. FINAL STAGE DENSIFICATION KINETICS OF DIRECT CURRENT SINTERED ZrB_2

Austin D. Stanfield[1], Nina N. Obradović[2], Vladimir V. Bulljak[3],
Gregory E. Hilmas[1], William G. Fahrenholtz[1]

[1] Deparment of Materials Science and Engineering, Missouri University of Science and Technology, Rolla, MO 65409

[2] Institute of Technical Sciences of the Serbian Academy of Science and Arts, Belgrade, SRB

[3] Strength of Materials Department, University of Belgrade, Belgrade, SRB

ABSTRACT

Final stage sintering ($\rho_{relative} > 0.9$) was analyzed for nominally phase pure zirconium diboride using the Nabarro-Herring stress directed vacancy diffusion model. Temperatures greater than 1850°C and an applied uniaxial pressure of 50 MPa were required to fully densify ZrB_2 ceramics by direct current sintering. Ram travel data were collected and used to determine the bulk density of the specimens during sintering. Specimens sintered between 1900 and 2100°C achieved relative densities greater than 97% while specimens sintered below 1900°C failed to reach the final stage of sintering. The average grain size ranged from 1.0 µm to 10.9 µm. The activation energy was calculated from the slope of an Arrhenius plot that utilized the Kalish equation. The activation energy was 162 ± 34 kJ/mol, which is consistent with the activation energy for dislocation movement in ZrB_2. The diffusion coefficients were 5.1 x 10^{-6} cm^2/s at 1900°C and 5.1 x 10^{-5} cm^2/s at 2100°C as calculated from activation energy and grain sizes.

Phenomenological modeling was used to simulate the sintering process and was in good agreement with experimental results. This study provides evidence that the dominant mechanism for final stage sintering of ZrB_2 ceramics is dislocation motion.

1. INTRODUCTION

Zirconium diboride (ZrB_2) is classified as an ultra-high temperature ceramic (UHTC) due to its melting temperature of 3250°C. In addition to its high melting temperature, interest in ZrB_2 is driven by properties such as strength (>500 MPa), hardness (>30 GPa), thermal conductivity (as high as 140 W/m·K), and chemical inertness making ZrB_2 a candidate material for applications such as leading edges for hypersonic aerospace vehicles, refractory linings, high temperature electrodes, and high speed cutting tools (1-10). These properties are due, in part, to the complex combination of different types of bonding. ZrB_2 has a hexagonal crystal structure with alternating layers of metallically bonded, close-packed zirconium atoms and covalently bonded boron rings. The bonding between the two types of layers is iono-covalent (11).

Densifying phase pure ZrB_2 is difficult due to strong covalent bonding and low self-diffusion coefficients. Sintering to full density generally requires temperatures above 1900°C and applied pressures greater than 32 MPa (12). For these reasons, hot pressing (HP), direct current sintering (DCS), and variants of both employing *in situ* reactions have become the favored sintering method for producing UHTCs with high relative density (13-17). For the intermediate stage of sintering ($0.65<\rho_{relative}<0.90$) of the Group IV diborides, activation energies that have been reported range from 140 to 695 kJ/mol for ZrB_2, 56 to 774 kJ/mol of TiB_2, and 96 kJ/mol for HfB_2(5,18-21). In general, studies have concluded that finer initial particle size and increased pressures reduced activation energies, even though the value of activation energy should only depend on the densification mechanism. For the intermediate stage of sintering, Lonergan reported that grain boundary diffusion was the dominant mechanism in reactively hot pressed ZrB_2 below 2000°C with an activation energy of 241 kJ/mol, but lattice diffusion became the dominant mechanism above 2000°C with an activation energy of 695 kJ/mol (19). Kalish studied the kinetics of the final stage of densification under extreme pressures (800 MPa) for HfB_2 and reported an activation energy of 96 kJ/mol. Kalish suggested that the mechanism could be dislocation flow because the activation energy was sufficiently low, but no other evidence of the mechanism was provided. Kalish ultimately concluded that interstitial diffusion of B or grain boundary diffusion of Hf was the predominant mechanism in the final stage of densification of HfB_2 (5). Since then, several studies have reported dislocation motion in the borides (22-27). Koval'chenko studied densification kinetics of molybdenum and tungsten borides, and reported that activation energies were independent of pressure, which is indicative of the dislocation glide process. Koval'chenko concluded that dislocation movement was limited by the self-diffusion of the metallic species in the metallic sublattice (26). Bahkri estimated an activation energy for dislocation movement in ZrB_2 of 154 ± 96 kJ/mol using indentation experiments and assuming the Burgers vector to be along any <1000> direction (22).

This study investigates the mechanism of the final stage of sintering for nominally phase pure ZrB_2.

2. DENSIFICATION MODEL

The final stage of densification was analyzed by the Nabarro-Herring stress-directed vacancy diffusion model (28,29). This model evaluates the movement of vacancies from crystal faces under tension to crystal faces under compression and the subsequent transfer of atoms from a crystal face under compression to a crystal face under tension. This model is also known as vacancy creep, and was used by Kalish to describe final stage densification of HfB_2 during hot pressing (30). Because both hot pressing and direct current sintering rely on pressure-assisted densification, Equation 1 can be used (30).

$$\ln\left[\ln\left(\frac{1-f_p}{1-f_{p_0}}\right)\right]-\ln\left[\exp\left(\frac{\sigma\Omega}{kT}\right)-\exp\left(-\frac{\sigma\Omega}{kT}\right)\right]=\ln\frac{Dt}{d^2}-\frac{Q}{RT} \tag{1}$$

where f_p is pore fraction, σ is stress corrected for the effect of porosity by the Sprigg's correction factor (Equation 2), σ_a is the uniaxially applied stress during DCS (31),

$$\sigma=\frac{\sigma_a}{1-f_p^{2/3}} \tag{2}$$

Ω is atomic volume, k is the Boltzmann constant, T is absolute temperature, D is the diffusion coefficient, t is time, d is grain size, Q is activation energy for diffusion, and R is the universal gas constant. A value of 15.4 $Å^3$ was used for the atomic volume (Ω) (32).

$$G=\ln\left(\frac{\ln\frac{1-f_{p_0}}{1-f_p}}{e^{\frac{\sigma\Omega_B}{kT}}-e^{\frac{-\sigma\Omega_B}{kT}}}\right) \tag{3}$$

$$G=\ln\frac{Dt}{d^2}-\frac{Q}{RT} \tag{4}$$

To determine the activation energy, the left side of Equation 1 can be rewritten as Equation 3 and plotted as a function of inverse temperature with the resulting linear trend having a slope of Q/R. The right hand side of Equation 1 can also be rewritten as Equation 4 and used to calculate the diffusion coefficient.

3. FINITE ELEMENT MODEL

A numerical model was used to analyze the sintering as transient process using the finite element method (FEM) with a combination of applied pressure and temperature within an uncoupled thermo-mechanical simulation. The inputs to the numerical model were the temperature and the applied pressure profiles. The phenomenological approach of Olevsky (36) was adopted whereby the material was treated as a continuum, i.e. porosity was not modeled directly, but averaged in the sense that it was included into the analysis through relative density. The relative density was related to the volumetric strain by Equation 7 with ρ_0 being the initial relative density.

$$\rho = \rho_0 e^{-(\varepsilon_{xx}+\varepsilon_{yy}+\varepsilon_{zz})} \tag{7}$$

The constitutive equation was a nonlinear viscous incompressible model in which the total strain rate was decomposed into three parts: thermal, elastic and viscous strain.

$$\dot{\boldsymbol{\varepsilon}} = \dot{\boldsymbol{\varepsilon}}^{th} + \dot{\boldsymbol{\varepsilon}}^{el} + \dot{\boldsymbol{\varepsilon}}^{vs} \tag{8}$$

The constitutive equation was thus of the following form:

$$\dot{\boldsymbol{\sigma}} = \boldsymbol{C}(\dot{\boldsymbol{\varepsilon}} - \dot{\boldsymbol{\varepsilon}}^{th} - \dot{\boldsymbol{\varepsilon}}^{vs}) \tag{9}$$

where $\dot{\sigma}$ is the applied stress, and $\boldsymbol{C}$ is the elasticity tensor. For this study, isotropic elastic behavior was assumed. This assumption allowed $\boldsymbol{C}$ to be defined using two independent constants, here specifically selected as the Young's modulus being equal to 440 GPa, and Poisson's ratio equal to 0.2. Isotropic behavior was also assumed for thermal expansion. Hence, only one thermal expansion coefficient was needed, while for the calculation of the viscous part of the strain rate, four additional constants were needed (36).

The constitutive model was implemented through a user subroutine within commercial finite element software (ABAQUS). Parameters entered into the governing equations of the model were quantified to match the curves of averaged relative density as a function of time collected during densification. For assessment of the parameters, an inverse analysis was used (37,38). The procedure is not detailed here for brevity, but was based on minimization of the discrepancy function between measured and computed curves. An uncoupled heat transfer simulation was first performed to obtain temperature fields as a function of time, which were then used as the thermal conditions in the sintering simulations.

4. PROCEDURE

ZrB_2 was synthesized by boro-carbothermal reduction of ZrO_2 (Reactor Grade, 99.7%, Hf< 75ppm, Materion, Mayfield Heights, OH, USA) according to Equation 5. ZrO_2 and carbon black (BP1100, Cabot, Alpharetta, GA, USA) were combined by high energy ball milling for 2 hours in a WC jar with WC media. The level of WC contamination was determined to be 0.02 wt% based on mass measurements of the jar and media before and after milling. The milled powder was then mixed with B_4C (H.S., H.C. Starck, Newton, MA, USA) by ball milling in acetone for 4 hours with zirconia media in an HDPE jar. To account for B loss in B_2O_3 volatilization during reaction, 13 wt% excess B_4C was added during milling.

$$2ZrO_{2(s)} + B_4C_{(s)} + 3C_{(s)} \rightarrow 2ZrB_{2(s)} + 4CO_{(s)} \qquad (5)$$

The mixture was dried by rotary evaporation, lightly ground with an alumina mortar and pestle to break agglomerates and pressed into 50 g pellets. Pellets were reacted in a resistively heated graphite element furnace (HP50-7010G, Thermal Technology, Santa Rosa, CA, USA) under mild vacuum (~3 Pa) with a 10°C/min heating rate with a 4 hour hold at 1650°C. The oxygen content of the resulting powder was measured by the inert gas fusion method (TS500, LECO, St. Joseph, MI, USA). Before densification, phenolic resin (GP 2074, Georgia Pacific, Atlanta, GA, USA) was added as a carbon source by ball milling in acetone for 4 hours. Dried powder was then densified by direct current sintering (DCS; DSC10 Thermal Technology) under mild vacuum (~2 Pa) in a 20 mm diameter graphite die. Specimens were heated at 100°C/min under 15 MPa applied pressure from room temperature to 1650°C. Specimens were held at that temperature for 5 min to promote removal of oxygen impurities from particle surfaces (33,34). After the hold, pressure was increased to 50 MPa, and specimens were heated at 100°C/min to the final densification temperature where temperature was held for 15 min. The furnace was then cooled at a rate of 100°C/min, and the pressure was released at 1500°C. X-ray diffraction (XRD; PANalytical X-Pert Pro, Malvern Panalytical Ltd., Royston, UK) analysis was used to identify phases present in the as-reacted powders and after final densification. Lattice parameters were determined using Rietveld refinement (RIQAS4, Materials Data Incorporated, Livermore, CA, USA) of XRD data, which were then used to calculate crystallographic density. Bulk density of the final specimens was determined by Archimedes' principle. Time-dependent relative density (ρ_t) was calculated from the final bulk densities of the specimens and ram travel data collected during DCS according to Equation 6

$$\rho_t = \frac{\rho}{\left(1+\frac{L_t}{L_f}\right)} \tag{6}$$

where L_t is specimen length at time t, and L_f is final length.

Scanning electron microscopy (SEM; TM-1000, Hitachi, Schaumberg, IL, USA) was performed utilizing a 15kV accelerating voltage and a current of 34.5 mA in backscattered electron mode. Grain size was determined by measuring the Feret diameter from SEM micrographs in a digital image processing software (ImageJ, National Institute of Health, Bethesda, MD, USA). A minimum of 200 grains were measured for each reported value. Micro-Raman spectroscopy (LabRam Aramis, HORIBA Jobin Yvon, Edison, NJ, USA) was used to identify secondary phases.

5. RESULTS

ZrB_2 was the only phase detected by XRD in all specimens. A representative XRD pattern is shown in Figure 1. The lattice parameters as calculated by Rietveld refinement were a = 3.1685 ± 0.0004 Å and c = 3.5309 ± 0.0002 Å with the variabilities being error from the Rietveld fit. Using the lattice parameters, a crystallographic density was 6.103 ± 0.001 g/cm^3 was calculated. Due to the low Hf content (<75 ppm) of the starting ZrO_2 precursor, the Hf content was assumed to be negligible in the calculation of theoretical density of the final ZrB_2.

Microstructure analysis revealed that the ceramics contained small volume fractions of porosity and a secondary phase (Figure 2). The predominant phase was ZrB_2, which appears as the gray phase in the micrographs. A small volume fraction of two types of inclusions was noted. First, the black circular inclusions with charging around the perimeter are porosity. Note that some additional angular voids were also present. The angular voids are consistent with grain pull-out that occurred during polishing and were not considered further. The circular black inclusions that do not have charging around the perimeter were residual B_4C that was not consumed in the reaction process. The composition of the B_4C inclusions was verified by Raman spectroscopy (not shown). A summary of the grain sizes and densities for all of the sintered specimens is provided in Table 1 along with specimen identification and densification temperatures. Among the ceramics produced, DCS_2100 had the largest average grain size at 10.9 ± 7.4 µm.

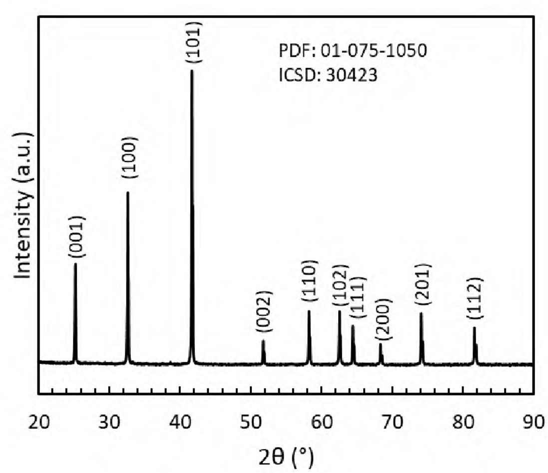

Figure 1: XRD pattern of ZrB_2 densified at 2100°C.

Table 1: Summary of densification temperature, density, and grain size for sintered specimens.

Specimen ID	Temperature (°C)	ρ_{bulk} (g/cm^3)	$\rho_{relative}$	Grain Size (µm)		
DCS_1800	1800	5.47	89.6%	1.0	±	0.5
DCS_1850	1850	5.54	90.8%	1.2	±	0.6
DCS_1900	1900	5.94	97.3%	2.4	±	1.9
DCS_1950	1950	6.02	98.7%	3.0	±	2.2
DCS_2000	2000	5.98	98.0%	7.6	±	5.2
DCS_2050	2050	6.06	99.2%		-	
DCS_2100	2100	5.94	97.4%	10.9	±	7.4

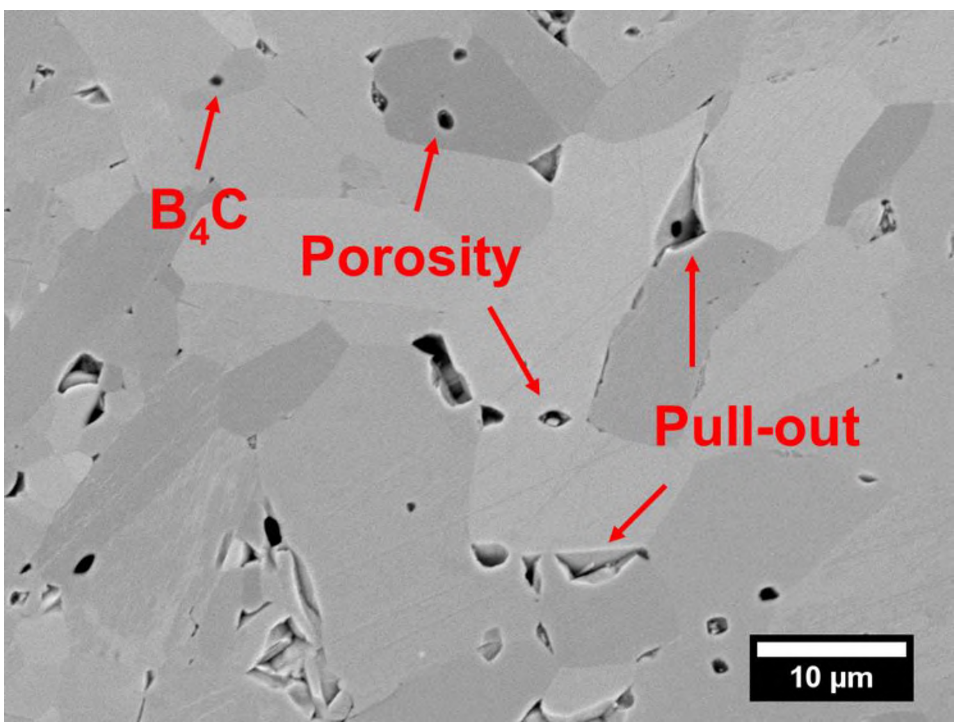

Figure 2: Cross section of DCS2000 showing porosity, secondary phases and grain pull-out.

Figure 3 shows the relative density as a function of time for different sintering temperatures. Densification data were collected from 1800 to 2100°C, but a distinct difference was noted in the densification rate and final density between specimens sintered above 1900°C compared to those sintered below that temperature. Results from DCS_1800 and DCS_1850 were not included in the final analysis of the mechanism(s) because the relative densities were too low and the specimens did not exhibit sufficient final stage sintering behavior for analysis. Specimens sintered at 1900°C and above achieved relative densities of 97% or higher and had a significant portion of their densification curves above 90%, which indicated that they had reached the final stage of densification. Figure 4 shows the value of G calculated using Equation 3 as a function of time for specimens sintered at and above 1900°C. The activation energy was calculated from the slope of the plot of G as a function of inverse temperature (Figure 5). Using four different densities ranging from 0.950 to 0.973, the average activation energy was determined to be 168 ± 24 kJ/mol. This value is in good agreement with the activation energy estimated for dislocation movement reported by Bahkhri (22).

The dislocation diffusion coefficient was calculated from the activation energy and grain size for 1900°C and 2100°C according to Equation 3. Final grain sizes were used as it was assumed that no significant grain growth occurred upon cooling from the sintering temperature. The diffusion coefficient was 5.1×10^{-6} cm^2/s at 1900°C and 5.1×10^{-5} cm^2/s at 2100°C. The 1900°C diffusion coefficient is similar to the values of 2.4×10^{-6} cm^2/s calculated by Kalish for HfB_2. The dislocation diffusion coefficients are also consistent with self-diffusion in Zr which validates Koval'chenko's conclusion that

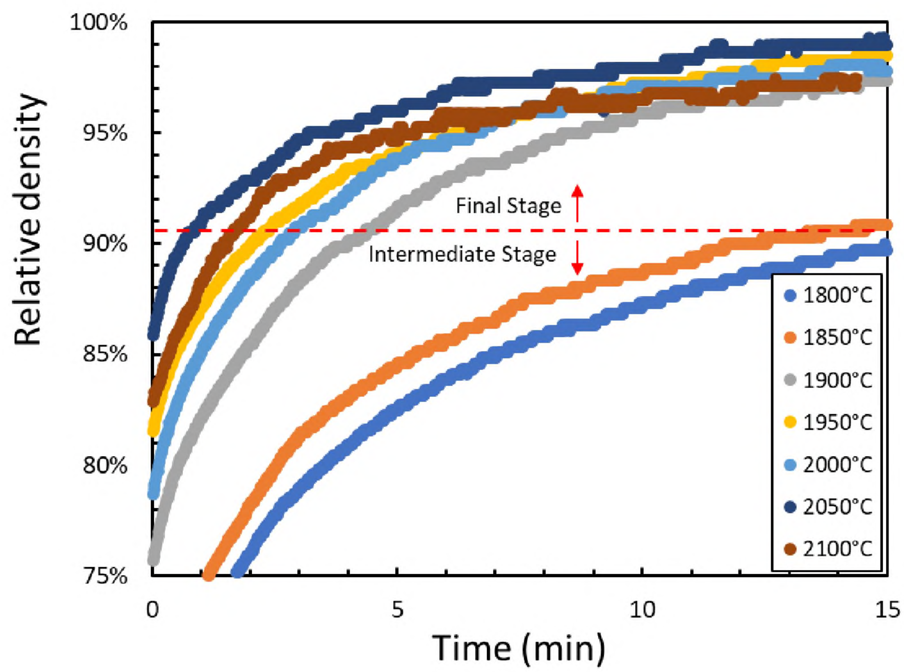

Figure 3: Relative densities as a function of sintering time.

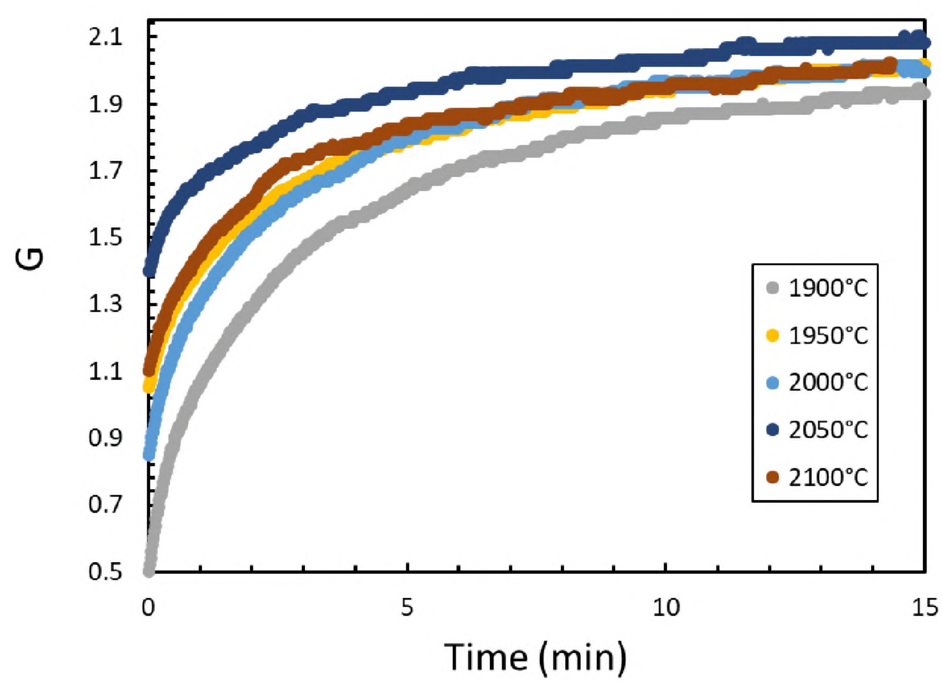

Figure 4: Time dependent densification data plotted as G calculated using Equation 3.

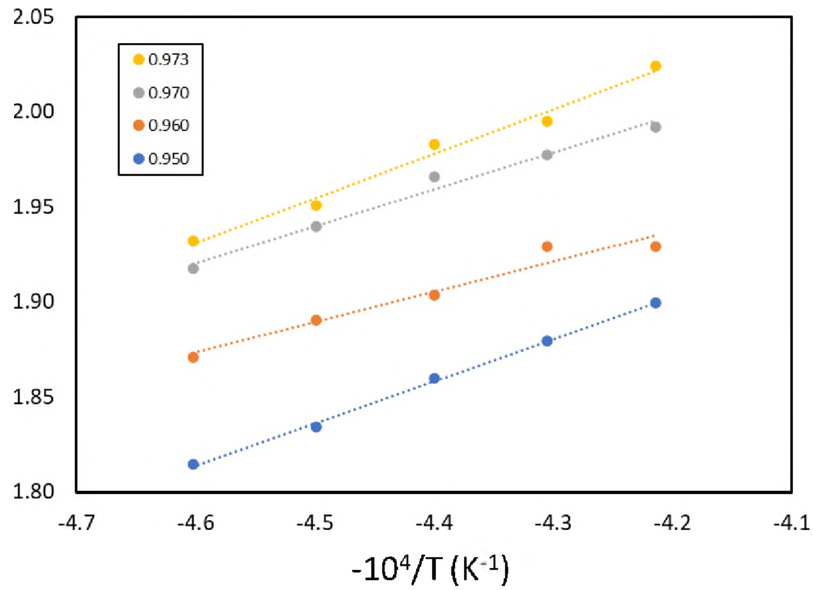

Figure 5: Temperature dependence of the G function for relative densities in the range of 0.950 to 0.973.

dislocation movement is limited by the self-diffusion of the metallic species in the metallic sublattice (26,35).

Figure 6 compares the computed and experimental averaged relative densities as a function of sintering time for densification at 1900°C. The two curves matched reasonably well. Aside from the overall global response of the material in terms of the change in averaged relative density with sintering time, the numerical model also provides insight into local distribution of relative density as well as the local stresses and strains during the sintering process. The model indicates thermal strain starts to rise during initial densification, which, in turn, triggers the elastic strain to generate stresses to satisfy the equilibrium. As deformation continues, the viscous component of the strain starts to grow and becomes dominant in the later stages of the sintering process, which is consistent with the dislocation creep mechanism determined from the analysis of experimental results. In addition, the transition from one mechanism to another one is described by the model parameters and can be quantified from the distribution of internal stresses and/or relative densities throughout the specimen by examining microstructures at intermediate times during sintering.

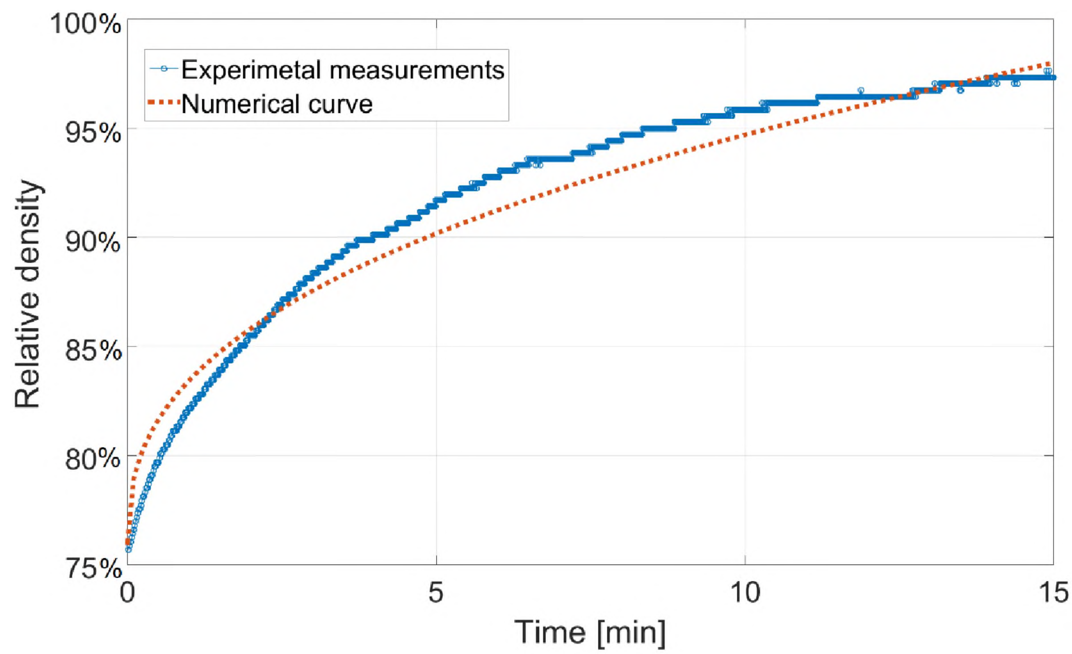

Figure 6: Relative density as a function of time curves for sintering at 1900°C comparing results from experiments and the numerical simulation.

6. CONCLUSIONS

Final stage densification kinetics were studied in nominally phase pure ZrB_2. Temperatures above 1850°C were needed to reach the final stage of densification. Relative densities of >97% were achieved for sintering temperatures of 1900°C and above with an applied stress of 50 MPa. The activation energy was determined to be 168

± 24 kJ/mol, which was consistent with the activation energy of dislocation movement as calculated from indentation experiments. The diffusion coefficient ranged from 5.1×10^{-6} at 1900°C to 5.1×10^{-5} cm^2/s at 2100°C. A numerical model used experimental data to show that the mechanism active during the final stage of sintering was consistent with the dislocation motion mechanism proposed herein. While grain boundary and lattice diffusion have previously been identified as controlling mechanisms for the intermediate stage of densification in ZrB_2, this study provides evidence that dislocation motion is critical for ZrB_2 ceramics to reach full density during final stage sintering.

ACKNOWLEDGEMENTS

This research was funded by the National Science Foundation (CMMI-1902069). The authors would like to thank the advanced materials characterization laboratory at Missouri S&T.

REFERENCES

1. Zapata-Solvas E, Jayaseelan DD, Lin H-T, Brown P, Lee WE. Mechanical properties of ZrB_2-and HfB_2-based ultra-high temperature ceramics fabricated by spark plasma sintering. J Eur Ceram Soc. 2013;33(7):1373–86.

2. Fridlender BA, Neshpor VS, Ordan'yan SS, Unrod VI. Thermal conductivity and thermal diffusivity of binary alloys of the ZrC-ZrB_2 system at high temperatures. Teplofiz Vysok Temp. 1979;17(6):1210–5.

3. Stanfield AD, Hilmas GE, Fahrenholtz WG. Effects of Ti, Y, and Hf additions on the thermal properties of ZrB_2. J Eur Ceram Soc [Internet]. 2020; Available from: https://www.scopus.com/inward/record.uri?eid=2-s2.0-85085092015&doi=10.1016%2Fj.jeurceramsoc.2020.04.011&partnerID=40&md5=0312c793c57d6e7402a378ed3cc49c81

4. Guo S, Nishimura T, Kagawa Y. Preparation of zirconium diboride ceramics by reactive spark plasma sintering of zirconium hydride–boron powders. Scr Mater [Internet]. 2011;65(11):1018–21. Available from: http://www.sciencedirect.com/science/article/pii/S1359646211005331

5. Clougherty E V, Kalish D, Peters ET. Research and developement of refractory oxidation-resistant diboride. Wright Patterson Air Force Base; 1968.

6. Csanádi T, Grasso S, Kovalčíková A, Dusza J, Reece M. Nanohardness and elastic anisotropy of ZrB_2 crystals. J Eur Ceram Soc. 2016;36(1):239–42.

7. Opeka MM, Talmy IG, Zaykoski JA. Oxidation-based materials selection for 2000°C + hypersonic aerosurfaces: Theoretical considerations and historical experience. J Mater Sci [Internet]. 2004;39(19):5887–904. Available from: http://dx.doi.org/10.1023/B:JMSC.0000041686.21788.77

8. Kaji N, Shikano H, Tanaka I. Development of ZrB_2-graphite protective sleeve for submerged nozzle. Taikabutsu Overseas. 1994;14(2):39–43.

9. Stucker BE, Bradley WL. Rapid prototyping of zirconium diboride/copper electrical discharge machining electrodes [Internet]. Vol. 9800816. [Ann Arbor]: Texas A&M University; 1997. Available from: http://libproxy.mst.edu:2048/login?url=http://search.proquest.com/docview/304406135?accountid=14594

10. Murata Y. Cutting tool tips and ceramics containing hafnium nitride and zirconium diboride. Google Patents; 1970.

11. Spear KE. Chemical Bonding in AlB_2-Type Borides. J Less-Common Met. 1976;47:195–201.

12. Sonber JK, Suri AK. Synthesis and consolidation of zirconium diboride. Adv Appl Ceram. 2011;110(6):321–34.

13. Zou J, Zhang GJ, Vleugels J, Van der Biest O. High temperature strength of hot pressed ZrB_2-20vol% SiC ceramics based on ZrB_2 starting powders prepared by different carbo/boro-thermal reduction routes. J Eur Ceram Soc [Internet]. 2013;33(10):1609–14. Available from: http://dx.doi.org/10.1016/j.jeurceramsoc.2013.03.001

14. Guo W-M, Zhang G-J. Reaction Processes and Characterization of ZrB_2 Powder Prepared by Boro/Carbothermal Reduction of ZrO2in Vacuum. J Am Ceram Soc. 2009;92(1):264–7.

15. Chamberlain AL, Fahrenholtz WG, Hilmas GE. Reactive hot pressing of zirconium diboride. J Eur Ceram Soc. 2009;29(16):3401–8.

16. Venugopal S, Paul A, Vaidhyanathan B, Binner JGP, Heaton A, Brown PM. Synthesis and spark plasma sintering of sub-micron HfB_2: Effect of various carbon sources. J Eur Ceram Soc [Internet]. 2014;34(6):1471–9.

17. Fahrenholtz WG, Hilmas GE, Li R. Densification of Ultra-Refractory Transition Metal Diboride Ceramics. Sci Sinter [Internet]. 2020;52(1):1–14.

18. Karthiselva NS, Kashyap S, Yadav D, Murty BS, Bakshi SR. Densification mechanisms during reactive spark plasma sintering of Titanium diboride and Zirconium diboride. Philos Mag. 2017;97(19):1588–609.

19. Lonergan JM, Fahrenholtz WG, Hilmas GE. Sintering Mechanisms and Kinetics for Reaction Hot-Pressed ZrB_2. J Am Ceram Soc [Internet]. 2015;98(8):2344–51. Available from: http://dx.doi.org/10.1111/jace.13544

20. Khanra AK, Godkhindi MM, Pathak LC. Sintering behaviour of ultra-fine titanium diboride powder prepared by self-propagating high-temperature synthesis (SHS) technique. Mater Sci Eng A. 2007;454:281–7.

21. Ouabdesselam M, Munir ZA. The sintering of combustion-synthesized titanium diboride. J Mater Sci. 1987;22(5):1799–807.

22. Bhakhri V, Wang J, Ur-Rehman N, Ciurea C, Giuliani F, Vandeperre LJ. Instrumented nanoindentation investigation into the mechanical behavior of ceramics at moderately elevated temperatures. J Mater Res. 2012;27(1):65–75.

23. Haggerty JS, Lee DW. Plastic deformation of ZrB_2 single crystals. J Am Ceram Soc. 1971;54(11):572–6.

24. Ghosh D, Subhash G, Bourne GR. Room-temperature dislocation activity during mechanical deformation of polycrystalline ultra-high-temperature ceramics. Scr Mater. 2009;61(11):1075–8.

25. Sekido N, Ohmura T, Perepezko JH. Mechanical properties and dislocation character of YB_4 and YB_6. Intermetallics [Internet]. 2017;89:86–91. Available from: http://www.sciencedirect.com/science/article/pii/S0966979517301292

26. Koval'chenko MS, Bodrova LG. Densification kinetics of higher molybdenum and tungsten borides in hot pressing. Sov Powder Metall Met Ceram. 1975;14(6):469–73.

27. Patel M, Singh V, Reddy JJ, Prasad VVB, Jayaram V. Densification mechanisms during hot pressing of ZrB_2–20 vol.% SiC composite. Scr Mater. 2013;69(5):370–3.

28. Mott NF, Nabarro FRN. Conference on strength of solids. In: Phys Soc, London. 1948. p. 1.

29. Herring C. Diffusional viscosity of a polycrystalline solid. J Appl Phys. 1950;21(5):437–45.

30. Kalish D, Clougherty E V. Densification mechanisms in high-pressure hot-pressing of HfB_2. J Am Ceram Soc. 1969;52(1):26–30.

31. Spriggs RM, Vasilos T. Functional relation between creep rate and porosity for polycrystalline ceramics. J Am Ceram Soc. 1964;47(1):47–8.

32. Wang J. Processing and deformation of ZrB_2. Imperial College London; 2013.

33. Fahrenholtz WG, Hilmas GE, Zhang SC, Zhu S. Pressureless Sintering of Zirconium Diboride: Particle Size and Additive Effects. J Am Ceram Soc [Internet]. 2008;91(5):1398–404.

34. Neuman EW, Hilmas GE, Fahrenholtz WG. Strength of Zirconium Diboride to 2300°C. J Am Ceram Soc [Internet]. 2013;96(1):47–50. Available from: http://dx.doi.org/10.1111/jace.12114

35. Naik MC, Agarwala RP. Self and impurity diffusion in alpha-zirconium. Acta Metall [Internet]. 1967;15(9):1521–5. Available from: http://www.sciencedirect.com/science/article/pii/0001616067901836

36. Olevsky EA. Theory of sintering: from discrete to continuum. Mater Sci Eng R Reports. 1998;23(2):41–100.

37. Buljak V, Maier G. Proper orthogonal decomposition and radial basis functions in material characterization based on instrumented indentation. Eng Struct. 2011;33(2):492–501.

38. Buljak V. Inverse analyses with model reduction: proper orthogonal decomposition in structural mechanics. Springer Science & Business Media; 2011.

39. Obradović N, Fahrenholtz WG, Filipović S, Corlett C, Đorđević P, Rogan J, et al. Characterization of $MgAl_2O_4$ sintered ceramics. Sci Sinter. 2019;51(4).

IV. YTTRIUM SOLUBILITY IN HIGH ENTROPY BORIDE CERAMICS

Austin D. Stanfield, Gregory E. Hilmas, William G. Fahrenholtz

Deparment of Materials Science and Engineering, Missouri University of Science and Technology, Rolla, MO 65409

ABSTRACT

The effect of entropy stabilization on the solubility of Y in transition metal boride ceramics was assessed at 1700°C. Although YB_2 is not thermodynamically stable, Y dissolves into the AlB_2 structure in small quantities. For this study, ZrB_2 was chosen as the base AlB_2-type material and configurational entropy was incrementally increased by increasing the number of transition metal species present in single phase boride ceramics. The Y solubility was evaluated in four different compositions, specifically ZrB_2, $(Zr_{0.5}Ti_{0.5})B_2$, $(Zr_{0.33},Ti_{0.33},Hf_{0.33})B_2$, and $(Zr_{0.25}, Ti_{0.25}, Hf_{0.25}, Nb_{0.25})B_2$. Each of the boride powders was synthesized by boro-carbothermal reduction of the corresponding oxides and then mixed with YB_4 in a 1:1 weight ratio. The mixtures were spark plasma sintered at 1700°C for 60 minutes to promote dissolution of Y into the boride structure without forming liquid phases. A modified form of Vegard's law was used to estimate lattice parameters of the base boride compositions and estimate the dissolved Y content in each composition. The solubility was determined to be 0.05± 0.05 mol% in ZrB_2, 2.4 ± 0.8 mol% in $(Zr_{0.5}Ti_{0.5})B_2$, 2.8 ± 1.6 mol% in $(Zr_{0.33},Ti_{0.33},Hf_{0.33})B_2$, and 1.4 ± 1.4 mol% in $(Zr_{0.25}, Ti_{0.25}, Hf_{0.25}, Nb_{0.25})B_2$. The Y contents were also assessed by energy dispersive spectroscopy to corroborate amounts estimated from lattice parameter changes.

This work demonstrated that changes in lattice parameter can be used to estimate compositions of high entropy boride ceramics, and that configurational entropy alone did not control the solubility of Y in high entropy boride ceramics.

1. INTRODUCTION

High entropy boride (HEB) ceramics have recently attracted attention as a new class of ultra-high temperature ceramics (UHTCs) due to their potential for improved thermal stability, mechanical properties, oxidation resistance, radiation damage tolerance, and a generally broadened material design space compared to boride ceramics containing a single transition metal (1-9). In particular, one potential benefit of the entropy stabilization/high entropy approach is the stabilization of elements in a structure in which they are not thermodynamically stable in a conventional binary compound due to the increased configurational entropy (10). While several solid solutions and high entropy boride ceramics have been produced containing group IV-VI transition metals, no research to date has focused on the effect of entropy stabilization on the solubility of specific species in the boride lattice (9,11-14).

The species of interest in the present study was Y due to its potential to improve thermal shock resistance of borides compared to single element diborides (15). In addition, Y has a lower number of valence electrons compared to Zr, which can be used to tailor the valence electron count of the resulting solid solutions and thereby affect properties such as melting temperature, hardness, and elastic modulus (16-17). Liao used computational methods to construct a phase diagram of the Y-B system, which included a stable YB_2 phase (18). While this phase was also reported by Lundin and confirmed by Spear, more recent experimental studies have not been able to produce stable YB_2 (19-21). Additionally, the synthesis of phase-pure YB_2 has not, to the best of the authors' knowledge, been reported. Some studies have reported limited solubility of Y in ZrB_2. For example, McClane reported that 3 at% YB_2 dissolved into ZrB_2 that was hot pressed at 2100°C (12). Additionally, the Hume-Rothery rules of solid solutions suggest that YB_2 and ZrB_2 may exhibit solid solubility since the metallic radii vary by 12% (1.62 Å for Y and 1.45 Å for Zr) which is within the critical size factor limit of 15% (22-24).

Vegard's law (Equation 1) states that the lattice parameter (a) of a binary solid solution of components A and B is given by the weighted averages based upon their molar fraction (x) (25). While deviation from Vegard's law is observed when non-ideal solution behavior is exhibited, it is generally considered a good approximation in isostructural binary systems. Table 1 summarizes the lattice parameters used in this study

$$a_{A_{(1-x)}B_x} = (1-x)a_A + x\, a_B \tag{1}$$

The present study investigated the role of configurational entropy on the solubility of YB_2 in boride ceramics by incrementally increasing the number of constituent transition metal species.

Table 1: Reported lattice parameters of single-phase borides.

TMB_2	a (Å)	c (Å)	Source
TiB_2	3.03034	3.22953	(131)
YB_2	3.326	3.923	(33)
ZrB_2	3.116870	3.53002	(30)
NbB_2	3.107	3.340	(33)
HfB_2	3.14245	3.47602	(132)

2. PROCEDURE

Diboride powders were synthesized by the boro-carbothermal reduction of transition metal (TM) oxides (29). Four different compositions were produced as described by Reactions 2-5. The four compositions were ZrB_2, $(Zr_{0.5}Ti_{0.5})B_2$, $(Zr_{0.33},Ti_{0.33},Hf_{0.33})B_2$, and $(Zr_{0.25}, Ti_{0.25}, Hf_{0.25}, Nb_{0.25})B_2$, which are denoted as 1HEB, 2HEB, 3HEB, and 4HEB, respectively, throughout this manuscript. Oxide precursors (ZrO_2, Reactor Grade, 99.7%, Hf< 75ppm, Materion, Mayfield Heights, OH, USA; TiO_2, 99.9%, Alfa Aesar, Tewksbury, MA, USA; HfO_2,99%, Alfa Aesar; Nb_2O_5, 99.5%, Alfa Aesar) were mixed with carbon black (BP1100, Cabot, Alpharetta, GA, USA) by high energy ball milled for 2 hours in a WC jar with WC media. This method resulted in WC contamination of ~0.02 wt% in each batch as determined by weighing the milling jar and media before and after each milling run. The milled powders were then mixed with B_4C (H.S., H.C. Starck, Newton, MA, USA) by ball milling in acetone for 4 hours with zirconia media in an HDPE jar. To account for B loss by volatilization of B-O species during reaction, 13 wt% excess B_4C was incorporated. The mixture was dried by rotary evaporation, lightly ground with an alumina mortar and pestle to break agglomerates and pressed into 50 g pellets. Pellets were reacted in a resistively heated graphite element furnace (HP50-7010G, Thermal Technology, Santa Rosa, CA, USA) under mild vacuum (~3 Pa) with a 10°C/min heating rate with a 4 hour hold at 1650°C to evaporate excess B_2O_3 before a 10°C/min ramp to a 4 hour 2100°C isothermal hold to fully dissolve the high entropy boride according to Reaction 6 (29).

$$2HfO_{2(s)} + B_4C_{(s)} + 3C_{(s)} \rightarrow 2HfB_{2(s)} + 4CO_{(s)} \quad (2)$$

$$2ZrO_{2(s)} + B_4C_{(s)} + 3C_{(s)} \rightarrow 2ZrB_{2(s)} + 4CO_{(s)} \quad (3)$$

$$2TiO_{2(s)} + B_4C_{(s)} + 3C_{(s)} \rightarrow 2TiB_{2(s)} + 4CO_{(s)} \quad (4)$$

$$2Nb_2O_{5(s)} + B_4C_{(s)} + 4C_{(s)} \rightarrow 4NbB_{2(s)} + 5CO_{(s)} \quad (5)$$

$$0.2HfB_{2(s)} + 0.2ZrB_{2(s)} + 0.2TiB_{2(s)} + 0.2NbB_{2(s)} \rightarrow (Hf_{0.25},Zr_{0.25},Ti_{0.25},Nb_{0.25})B_{2(s)} \quad (6)$$

Yttrium was added in the form of YB_4 that was synthesized by the boro-carbothermal reduction of Y_2O_3 (99.99%, Rhône-Poulenc, Collegeville, PA, USA) according to Reaction 7. Y_2O_3, B_4C, and C were milled by the same process as the TMB_2 powders. A 10 wt% addition of excess B_4C was included to account for B loss in this composition. The mixture was dried and pressed into 50 g pellets that were reacted at 1650°C for 4 hours under mild vacuum (~3 Pa) and a 10°C/min heating rate. The treatment at 2100°C to promote solid solution formation was not necessary in this powder since it was single phase

$$Y_2O_{3(s)} + 2B_4C_{(s)} + C_{(s)} \rightarrow 2YB_{4(s)} + 3CO_{(g)} \quad (7)$$

The various boride powders were mixed with YB_4 in a 1:1 ratio by weight to provide a large excess of Y for dissolution. Powders were mixed by ball milling in HDPE jars with acetone and ZrO_2 media for 4 hours. Samples with YB_4 additions are denoted by the suffix "Y" such as 1HEBY. The presumed dissolution process is described by Reaction 8.

$$ZrB_{2(s)} + 2YB_{4(s)} \rightarrow 2(Zr_{0.5},Y_{0.5})B_{2(s)} + YB_{6(s)} \quad (8)$$

Mixed powders were then reacted by direct current sintering (DCS;DSC10 Thermal Technology, Santa Rosa, CA) under mild vacuum (2 Pa) in a 20 mm graphite die. A ramp rate of 100°C/min under 15 MPa applied pressure was used on heating to a 5 minute isothermal hold at 1650°C. After the hold the pressure was increased to 50 MPa, and a ramp rate of 100°C/min was used to reach the 60 minute, 1700°C isothermal hold. This was the highest temperature that could be used for solution treatments due to a eutectic reaction between YB_4 and the boride powders. The furnace was then cooled at 100°C/min, and pressure was released at 1500°C. Consolidated specimens were then annealed in a resistively heated graphite element furnace for 12 and 24 hours at 1700°C to promote further dissolution and attempt to reach thermodynamic equilibrium without forming a liquid phase.

X-ray diffraction (XRD; PANalytical X-Pert Pro, Malvern Panalytical Ltd., Royston, UK) was used for phase analysis of the high entropy boride powders before and after YB_4 additions. An anatase internal standard and scan range of $20° < 2\theta < 138°$ was used to determine lattice parameters. Rietveld refinement (RIQAS4, Materials Data Incorporated, Livermore, USA) was used to calculate lattice parameters from XRD patterns. Scanning electron microscopy (SEM; Helios NanoLab 600, FEI, Hillsboro, USA) was performed utilizing secondary electron (SE) mode with an accelerating voltage of 18 kV and emission current of 1.4 nA. Energy dispersive spectroscopy (EDS; AZtec, Oxford Instruments, Concord, MA, USA) was used for quantitative chemical elemental analysis. A minimum of 7 areas were analyzed per sample with selected areas in the center of the HEB phase and at least 1 μm from the YB_4 phase or other features.

$$a_{nHEB} = \sum_{i=1}^{n} x_i a_i \tag{9}$$

Equation 9 is a modified form Vegard's law (Equation 1) that was used to estimate the lattice parameter *a* (or *c*) for *n* number of species in solid solution based upon their corresponding molar fraction *x*.

3. RESULTS AND DISCUSSION

All of the HEB compositions formed a single diboride phase with no indication of secondary phases by XRD. Figure 1 shows the XRD patterns of the as-reacted HEB powders prior to reaction with YB_4. The positions of the peaks were expected to be shifted compared to nominally pure ZrB_2 due to the additions of the other transition metals and as predicted by Vegard's laws. Table 2 summarizes the lattice parameters of the HEB materials produced in the present study as calculated by Vegard's law and as determined from Rietveld refinement of XRD data. The difference between predicted and measured lattice parameters was less than 0.1% for all a-axes and less than 1% for all c-axes for all compositions. Reported error is due to discrepancies between modelled and measured peak profiles during Rietveld refinement. Residual error in the refinement process is also reported. Composition 2HEB had the largest difference between the measured lattice parameters and those predicted from Vegard's law with a 0.08% difference in the a-axis and 0.68% in the c-axis. All of the differences between predictions and measured lattice parameters are small, which indicates that Vegard's law is an appropriate method for relating composition to lattice parameters for this series of compositions. Hence, the same methodology was then used to estimate the Y content of HEBY compositions from measured lattice parameters. Using both the a and c-axes provided a range of possible dissolved YB_2 contents that was used to estimate the variability of the process. The differences in lattice parameters between the HEB compositions and the corresponding HEBY compositions are presented in Figure 2 and summarized in Table 2. For the analysis that follows, the average change in the a and c-axis calculations is used with the deviation corresponding to the bounds set by the difference between the two calculations.

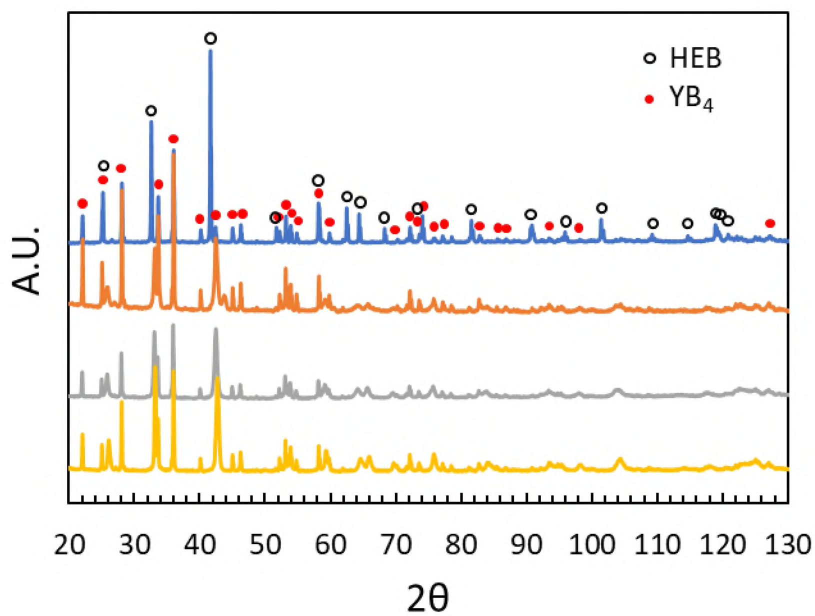

Figure 1: XRD patterns of HEBY compositions after the 24 hour annealing.

Yttrium solubility was relatively low in all compositions. Based on Vegard's law calculations, the YB_2 content dissolved into 1HEBY was 0.05 ± 0.05 mol%. The dissolved Y contents were higher for some of the other compositions at 2.4 ± 0.8 mol% for 2HEBY and 2.8 ± 1.6 mol% for 3HEBY. As with HEBY, the Y content o

Table 2: Predicted and Measured Lattice Parameters for HEB phase.

Sample ID	Compositions	predicted a (Å)	predicted c (Å)	measured a (Å)	measured c (Å)	% Difference a	% Difference c	$\rho_{xtal,\ rietveld}$ (g/cm^3)	$error_{residual}$ (%)
1HEB	ZrB_2	3.1700	3.5300	3.16812 ± 0.00002	3.53112 ± 0.00006	-0.06%	0.03%	6.100	7.00
2HEB	$(Zr_{0.5},Ti_{0.5})B_2$	3.1002	3.3798	3.10274 ± 0.00005	3.40289 ± 0.00013	0.08%	0.68%	5.258	5.56
3HEB	$(Zr_{0.33},Ti_{0.33},Hf_{0.33})B_2$	3.1138	3.4098	3.10844 ± 0.00011	3.39189 ± 0.00025	-0.17%	-0.53%	7.394	7.67
4HEB	$Zr_{0.25},Ti_{0.25},Hf_{0.25},Nb_{0.25})B_2$	3.1103	3.3869	3.10856 ± 0.00050	3.39079 ± 0.00079	-0.06%	0.12%	7.271	8.51
1HEBY	$ZrB_2 + YB_4$	--	--	3.16904 ± 0.00002	3.53042 ± 0.00006	--	--	--	6.45
2HEBY	$(Zr_{0.5},Ti_{0.5})B_2 + YB_4$	--	--	3.11753 ± 0.00006	3.43166 ± 0.00014	--	--	--	6.32
3HEBY	$(Zr_{0.33},Ti_{0.33},Hf_{0.33})B_2 + YB_4$	--	--	3.11504 ± 0.00028	3.43557 ± 0.00077	--	--	--	7.09
4HEBY	$Zr_{0.25},Ti_{0.25},Hf_{0.25},Nb_{0.25})B_2 + YB_4$	--	--	3.10755 ± 0.00049	3.40667 ± 0.00076	--	--	--	8.51

4HEBY was lower with a value of 1.4 ± 1.4 mol%. Based on this analysis, the YB_2 content of 1HEBY and 4HEBY was 0% according to a-axis calculations with dissolved YB_2 contents of less than 3 mol% for all compositions.

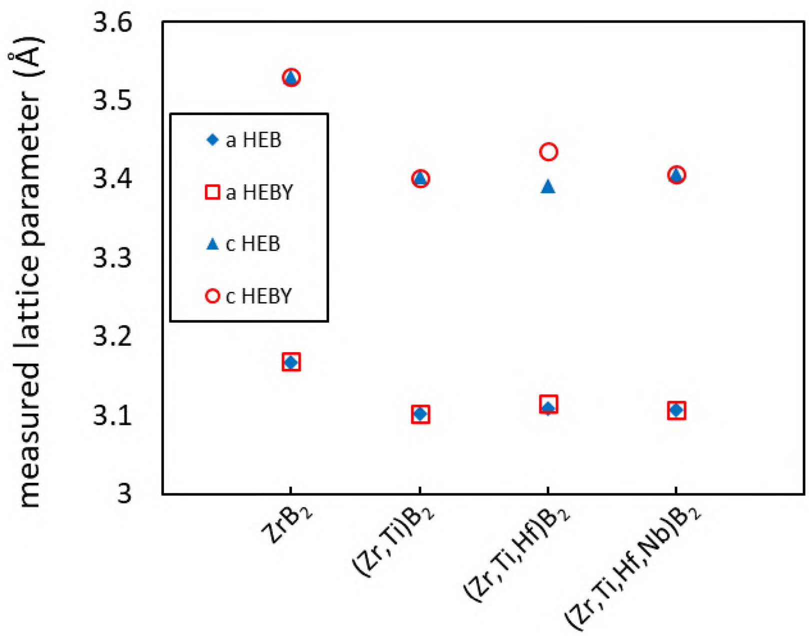

Figure 2: a and c lattice parameters for the HEB and corresponding HEBY compositions.

EDS was used to analyze the dissolved yttrium contents and support estimations from Vegard's law. Distributions of Y are shown visually in EDS maps shown in Figure 3 and measured Y contents are summarized Table 3. Yttrium content is reported on a metals basis for direct comparison between elemental analysis and dissolved YB_2 content in the HEBY compositions. The highest dissolved Y contents were measured in 2HEBY with a Y content of 3.5 ±3.0 mol% and 3HEBY with a dissolved Y content of 5.4 ± 2.4 mol%. The average of 2HEBY is within the range of Y contents estimated by Vegard's law. While the average of 3HEBY is 0.4 mol% greater than the Vegard's law calculation, the 2 values are within one standard deviation of each other and are considered in agreeance. The Y content of 4HEBY was within Vegard's law estimation at 1.3 mol%. Yttrium was not detected by EDS in 1HEBY, which agrees with the lower bounds for Y content indicated by the lack of change in the a-axis lattice parameters for that composition. In addition, this is consistent with the 0.10 mol% upper bound predicted for 1HEBY.

Table 3: Dissolved YB_2 in HEB sintered at 1700°C as calculated by Vegard's law and measured by EDS.

	Vegard's Law				
Sample ID	a (mol%)	c (mol%)	EDS (mol%)		
1HEBY	0.00	0.10	0.0	±	0.0
2HEBY	0.80	4.00	3.5	±	3.0
3HEBY	0.60	5.00	5.4	±	2.4
4HEBY	0.00	2.70	1.3	±	1.3

The EDS analysis could underestimate the Y content in the HEBY ceramics. One potential issue is that the characteristic X-ray peaks of Y Lα (1.92 keV) and Zr Lα (2.04 keV) overlap due to the line width in EDS spectra. This can be seen visually in Figure 3 as it appears Zr is present in YB_4 with an estimated content of 1.3 mol%. Another source of error may be the assumption that HEBY samples obey Vegard's law. However, this seems unlikely because the base HEBs appeared to obey Vegard's law and the size of the Y atoms was within 12% of Zr. In addition, the YB_2 contents determined by all methods

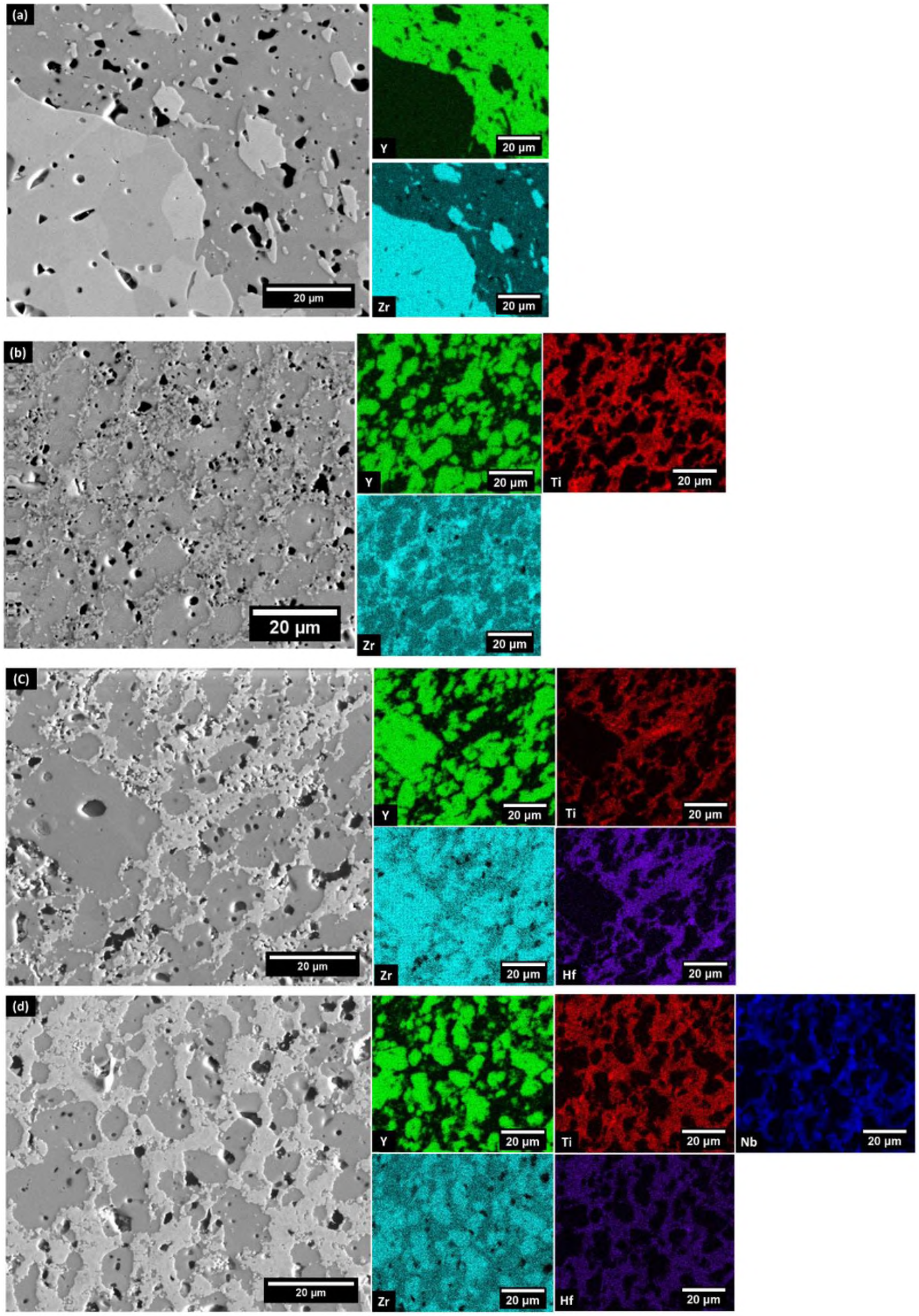

Figure 3: SEM and EDS analysis of (a) 1HEBY, (b) 2HEBY, (c) 3HEBY, and (d) 4HEBY.

were small enough that any deviations from the predictions should be small. Based on this analysis, the solubility of Y into ZrB_2 appears to be less than 0.1 mol% at 1700°C. The other 2 and 3 component HEB compositions have small solubilities for Y, indicating that the presence of additional transition metal species enhances the solubility of Y in the boride lattice. However, the content of Y in the four component HEB was smaller than the 2 and 3 component HEBs, which indicates that the entropy stabilization effect did not enhance Y solubility in this system.

4. CONCLUSION

The solubility of Y in transition metal boride ceramics was determined at 1700°C. The effect of configurat entropy on solubility was studied by increasing the number of constituents in the borides from ZrB_2 containing a single transition metal up to four constituents in $(Zr_{0.25},Ti_{0.25},Hf_{0.25},Nb_{0.25})B_2$. Lattice parameters of the base boride compositions were calculated within 0.7% of measured lattice parameters using Vegard's law. This same principle was used to estimate the dissolved Y content in samples reacted with YB_4 at 1700°C for 24 hours. The solubilities were determined to be 0.05± 0.05 mol% in ZrB_2, 2.4 ± 0.8 mol% in $(Zr_{0.5},Ti_{0.5})B_2$, 2.8 ± 1.6 mol% in $(Zr_{0.33},Ti_{0.33},Hf_{0.33})B_2$, and 1.4 ± 1.4 mol% in $(Zr_{0.25},Ti_{0.25},Hf_{0.25},Nb_{0.25})B_2$. Elemental analysis by EDS agreed with YB_2 contents calculated by lattice parameters. This work provides evidence that Vegard's law is a viable technique to estimate high entropy boride lattice parameters, and increasing the entropy of mixing does not necessarily increase the solubility limit of Y in HEBs at 1700°C.

ACKNOWLEDGEMENTS

This work was funded by the National Science Foundation through grant CMMI-1902069. The authors thank the advanced materials characterization laboratory at Missouri University of Science and Technology.

REFERENCES

1. Zhang Y, Stocks GM, Jin K, Lu C, Bei H, Sales BC. Influence of chemical disorder on energy dissipation and defect evolution in concentrated solid solution alloys. Nat Commun. 2015;6.

2. Backman L, Gild J, Luo J, Opila EJ. Part II: Experimental verification of computationally predicted preferential oxidation of refractory high entropy ultra-high temperature ceramics. Acta Mater [Internet]. 2020;197:81–90. Available from: http://www.sciencedirect.com/science/article/pii/S1359645420305024

3. Butler TM, Chaput KJ, Dietrich JR, Senkov ON. High temperature oxidation behaviors of equimolar NbTiZrV and NbTiZrCr refractory complex concentrated alloys (RCCAs). J Alloys Compd. 2017;729:1004–19.

4. Müller F, Gorr B, Christ H-J, Müller J, Butz B, Chen H. On the oxidation mechanism of refractory high entropy alloys. Corros Sci. 2019;159.

5. Dai F-Z, Sun Y, Wen B, Xiang H, Zhou Y. Temperature Dependent Thermal and Elastic Properties of High Entropy $(Ti_{0.2}Zr_{0.2}Hf_{0.2}Nb_{0.2}Ta_{0.2})B_2$: Molecular Dynamics Simulation by Deep Learning Potential. J Mater Sci Technol [Internet]. 2021;72:8–15. Available from: https://www.scopus.com/inward/record.uri?eid=2-s2.0-85092074105&doi=10.1016%2Fj.jmst.2020.07.014&partnerID=40&md5=8bc704aa9a46404f25777e643658a69d

6. Gild J, Wright A, Quiambao-Tomko K, Qin M, Tomko JA, Shafkat bin Hoque M. Thermal conductivity and hardness of three single-phase high-entropy metal diborides fabricated by borocarbothermal reduction and spark plasma sintering. Ceram Int. 2020;46(5):6906–13.

7. Liu J-X, Shen X-Q, Wu Y, Li F, Liang Y, Zhang G-J. Mechanical properties of hot-pressed high-entropy diboride-based ceramics. J Adv Ceram. 2020;9(4):503–10.

8. Chen H, Xiang H, Dai F-Z, Liu J, Zhou Y. Porous high entropy $(Zr_{0.2}Hf_{0.2}Ti_{0.2}Nb_{0.2}Ta_{0.2})B_2$: A novel strategy towards making ultrahigh temperature ceramics thermal insulating. J Mater Sci Technol. 2019;35(10):2404–8.

9. Gild J, Zhang Y, Harrington T, Jiang S, Hu T, Quinn MC, et al. High-Entropy Metal Diborides: A New Class of High-Entropy Materials and a New Type of Ultrahigh Temperature Ceramics. Sci Rep [Internet]. 2016;6. Available from: https://www.scopus.com/inward/record.uri?eid=2-s2.0-84999836701&doi=10.1038%2Fsrep37946&partnerID=40&md5=594ea6a70e3c75ddaabdb07b37fffb6e

10. Rost CM, Sachet E, Borman T, Moballegh A, Dickey EC, Hou D. Entropy-stabilized oxides. Nat Commun [Internet]. 2015;6. Available from: https://www.scopus.com/inward/record.uri?eid=2-s2.0-84942894980&doi=10.1038%2Fncomms9485&partnerID=40&md5=08474f5f1d2352ac18010927d3e222ba

11. McClane DL, Fahrenholtz WG, Hilmas GE. Thermal Properties of $(Zr,TM)B_2$ Solid Solutions with TM = Ta, Mo, Re, V, and Cr. J Am Ceram Soc [Internet]. 2015 Feb [cited 2016 Jun 13];98(2):637–44. Available from: http://doi.wiley.com/10.1111/jace.13341

12. McClane DL, Fahrenholtz WG, Hilmas GE. Thermal properties of $(Zr,TM)B_2$ solid solutions with TM = Hf, Nb, W, Ti, and y. J Am Ceram Soc. 2014;97(5):1552–8.

13. Lonergan JM, McClane DL, Fahrenholtz WG, Hilmas GE. Thermal Properties of Hf-Doped ZrB_2 Ceramics. J Am Ceram Soc [Internet]. 2015;98(9):2689–91. Available from: http://dx.doi.org/10.1111/jace.13717

14. Dorner AN, Barton DJ, Zhou Y, Thompson GB, Hilmas GE, Fahrenholtz WG. Solute distributions in tantalum-containing zirconium diboride ceramics. J Am Ceram Soc. 2020;103(4):2880–90.

15. Zhou Y, Wang J, Li Z, Zhan X, Wang J. First-Principles Investigation on the chemical bonding and intrinsic elastic properties of transition metal diborides TMB_2 (TM=Zr, Hf, Nb, Ta, and Y). In: Fahrenholtz WG, Wuchina EJ, Lee WE, Zhou Y, editors. Ultra-High Temperature Ceramics. 1st ed. Hoboken, New Jersey: John Wiley & Sons; 2014. p. 60–82.

16. Grimvall G, Fernández Guillermet A. Phase stability properties of transition metal diborides. In: AIP Conference Proceedings. American Institute of Physics; 1991. p. 423–30.

17. Yeung MT, Lei J, Mohammadi R, Turner CL, Wang Y, Tolbert SH, et al. Superhard monoborides: hardness enhancement through alloying in $W_{1-x}Ta_xB$. Adv Mater. 2016;28(32):6993–8.

18. Liao PK, Spear KE. The BY (boron-yttrium) system. J phase equilibria. 1995;16(6):521–4.

19. Lundin CE. Rare earth metal phase diagrams. In: Rare Earth Symposium, Annual Meeting. 1959.

20. Spear KE. Rare earth-boron phase equilibria. In: Boron and Refractory Borides. Springer; 1977. p. 439–56.

21. Post B. Refractory binary borides. POLYTECHNIC INST OF BROOKLYN NY; 1962.

22. Hume-Rothery W, Coles BR. The transition metals and their alloys. Adv Phys [Internet]. 1954;3(10):149–242.

23. Hume-Rothery W. Atomic diameters, atomic volumes and solid solubility relations in alloys. Acta Metall [Internet]. 1966;14(1):17–20. Available from: http://www.sciencedirect.com/science/article/pii/0001616066902677

24. Pauling L. Atomic Radii and Interatomic Distances in Metals. J Am Chem Soc [Internet]. 1947;69(3):542–53. Available from: http://dx.doi.org/10.1021/ja01195a024

25. Vegard L. Die Konstitution der Mischkristalle und die Raumfüllung der Atome. Zeitschrift für Phys [Internet]. 1921;5(1):17–26.

26. Norton JT, Blumenthal H, Sindeband SJ. Structure of diborides of titanium, zirconium, columbium, tantalum and vanadium. JOM. 1949;1(10):749–51.

27. Post B, Glaser FW, Moskowitz D. Transition metal diborides. Acta Metall [Internet]. 1954;2(1):20–5. Available from: http://www.sciencedirect.com/science/article/pii/0001616054900905

28. Wong-Ng W, McMurdie HF, Paretzkin B, Zhang Y, Hubbard CR, Dragoo AL. Standard x-ray diffraction powder patterns of fifteen ceramic phases. Powder Diffr. 1988;3(1):47–56.

29. Feng L, Fahrenholtz WG, Hilmas GE. Two-step synthesis process for high-entropy diboride powders. J Am Ceram Soc [Internet]. 2020;103(2):724–30. Available from: https://www.scopus.com/inward/record.uri?eid=2-s2.0-85073917803&doi=10.1111%2Fjace.16801&partnerID=40&md5=7500fdb91aa8d4d4d604a5d6611d1a7b

SECTION

3. CONCLUSIONS AND RECOMMENDATIONS

3.1. CONCLUSIONS

This research expanded the fundamental knowledge of UHTCs by investigating the thermophysical properties of nominally phase pure boride ceramics by answering the questions posed in Section I.

- Do transition metal additions effect thermal properties of nominally phase pure ZrB_2?

While previous work had demonstrated that transition metal additions affect thermal properties of commercially available ZrB_2, the present research utilized RHP to produce low-Hf ZrB_2 and demonstrate that additions of Y and Ti altered thermal conductivity. Ti and Y additions decreased the thermal conductivity compared to nominally pure, low-Hf ZrB_2, in contrast to results from previous studies using commercial powders with the natural abundance of Hf. To further demonstrate the impact of purity, Hf additions decreased thermal conductivity from ~141 W/m•K for low-Hf ZrB_2 to values similar to those commonly reported for commercial grades of ZrB_2 with the natural abundance of Hf. This study concluded that all transition metal additions decrease the phonon contribution to total thermal conductivity, possibly due to increasing point defects that serve as phonon scattering sites. However, not all transition metals appreciably alter the electronic structure. Therefore, the electron contribution to thermal conductivity may not decrease significantly. The study also provided evidence that the natural abundance of Hf in ZrB_2 partially masks the effects of some other solid solution additions such as Ti and Y, when their effect on thermal conductivity is small.

- What is the melting temperature of high purity ZrB_2?

To answer this question, the melting temperatures of two different types of ZrB_2 were evaluated by the laser heating and spectrometric analysis method. The first grade was a commercially available ZrB_2 containing 1.75 at% Hf. The second was a nominally phase pure ZrB_2 synthesized from a reactor grade ZrH_2 with a Hf content of 0.01 at% (100 ppm). The laser heating method successfully and repeatedly melted the specimens without altering their chemistry (i.e., melting was congruent with little or no vaporization). The melting temperatures of the commercial grade was 3280 ± 35°C and the reactor grade was 3273 ± 35°C. Additionally, an optical transition was detected in both materials near their melting temperatures which has not previously been reported. There was a measurable 7°C difference in the melting temperatures of the ZrB_2 grades, but the difference was within the uncertainty of the technique. While reducing Hf does elicit a measurable difference in melting temperature, it is a small and perhaps insignificant amount.

- What is the mechanism of final stage sintering in phase-pure ZrB_2?

The kinetics of the final stage of densification were investigated in low-Hf ZrB_2. This was possible because the absence of secondary phases and solute impurity atoms allowed for the study without competing extrinsic effects such as grain pinning and solute drag masking intrinsic densification kinetics. The dominant mechanism in the final stage of densification was determined to be dislocation motion with an activation energy of 162 kJ/mol. This work was significant because it elucidated the mechanism by which ZrB_2 and likely most TMB_2s achieve full density

- How does entropy stabilization affect solubility of yttrium in boride ceramics?

A study was performed that systematically increased the number of components in solution in a transition metal diboride phase to increase the configurational entropy. Components were chosen that followed the Hume-Rothery rules and the four base compositions formed single phases with nominal compositions: ZrB_2, $(Zr_{0.5}Ti_{0.5})B_2$, $(Zr_{0.33},Ti_{0.33},Hf_{0.33})B_2$, and $(Zr_{0.25}, Ti_{0.25}, Hf_{0.25}, Nb_{0.25})B_2$. Vegard's law was able to predict lattice parameters for the four compositions with a maximum difference of 0.7% compared to measured parameters. The solubility limit of yttrium diboride was measured in each composition to test if increasing configurational energy stabilized the HEB phase. YB_2 was chosen as it exhibited limited solubility in ZrB_2 and there is little experimental data verifying YB_2 as a stable phase. No statistically significant difference was detected in the solubility limit with increasing entropy and therefore the study provided no evidence of the entropy stabilization effect. With the study of high entropy materials growing, it is important to understand the fundamental limitations of entropy stabilization to aid the composition selection process.

The work contained in this document builds upon efforts that began roughly 70 years ago when NACA and the U.S. Air Force began their search for materials to enable operations in the extreme environments produced during hypersonic flight and atmospheric reentry. While diboride ceramics, among other UHTCs, were considered as candidate materials, these materials are still not used as hypersonic wing leading edges and rocket nozzles. This work adds new insight into the intrinsic properties (e.g., thermal conductivity and melting temperature), densification behavior, and solubility characteristics of boride ceramics.

3.2. RECOMMENDATIONS

While there is much work to be done in this field, the following 4 areas have been specifically identified for future work.

Single crystal property measurements of low-Hf ZrB_2. Single crystal properties should be greater than properties measured from polycrystalline ceramics. Furthermore, higher order properties of ZrB_2 are anisotropic due to its hexagonal crystal structure, and direct measurements will expand the body of knowledge of transition metal borides. Due to extreme processing temperatures, synthesizing a single crystal large enough for significant measurements will be a substantial achievement in itself.

While no evidence of entropy stabilization in HEBs was present in the work presented in this document, efforts should continue to study this effect. If present in HEB systems, entropy stabilization will increase the possible compositional space and end uses. The study in this document may have been limited by chosen processing techniques. Further studies should explore processing techiniques that mitigate container interactions at intermediate temperatures. Arc-melting is one suggested technique.

Configurational entropy benefits from disorder in the lattice produced by increasing the number of components in the system. HEBs thus far have focused on increasing the number of components in the transition metal sublattice. However, entropy stabilization may also benefit from increasing the components in the boron sublattice. C may be a candidate, but other elements that form impurities in B such as Mg and Fe should not be ruled out.

There is a lack of property measurements for HEBs. Notably, few thermal properteis have been measured, and thermal conductivity values reported were calculated using modelled heat capacity. As such, heat capacity should be measured to confirm or reject the validity of using rule of mixtures for calculated heat capacities. Additionally, electrical properties of HEBs should be studied as electrons are responsible for a significant portion fo thermal conductivity in single component diborides.

BIBLIOGRAPHY

1. Agte C, Moers K. Methoden zur reindarstellung hochschmelzender Carbide, Nitride und Boride und beschreibung einiger ihrer eigenschaften. Zeitschrift für Anorg und Allg Chemie. 1931;198(1):233–75.

2. Rudy E, Windisch S. Ternary Phase Equilibria in Transition Metal-Boron-Carbon-Silicon Systems Part I. Binary Phase Systems. AFML-TR-65-2. 1966;VIII:34.

3. Fahrenholtz WG, Wuchina EJ, Lee WE, Zhou Y. Ultra-High Temperature Ceramics: Materials for Extreme Environment Applications. Ultra-High Temperature Ceramics: Materials for Extreme Environment Applications. 2014. 1–441 p.

4. Lonergan JM, McClane DL, Fahrenholtz WG, Hilmas GE. Thermal Properties of Hf-Doped ZrB_2 Ceramics. J Am Ceram Soc [Internet]. 2015;98(9):2689–91. Available from: http://dx.doi.org/10.1111/jace.13717

5. Neuman EW, Hilmas GE, Fahrenholtz WG. Strength of Zirconium Diboride to 2300°C. J Am Ceram Soc [Internet]. 2013;96(1):47–50. Available from: http://dx.doi.org/10.1111/jace.12114

6. Opeka MM, Talmy IG, Zaykoski JA. Oxidation-based materials selection for 2000°C + hypersonic aerosurfaces: Theoretical considerations and historical experience. J Mater Sci [Internet]. 2004;39(19):5887–904. Available from: http://dx.doi.org/10.1023/B:JMSC.0000041686.21788.77

7. Murata Y. Cutting tool tips and ceramics containing hafnium nitride and zirconium diboride [Internet]. Google Patents; 1970. Available from: http://www.google.com/patents/US3487594

8. Ivanovskii AL. Mechanical and electronic properties of diborides of transition 3d-5d metals from first principles: Toward search of novel ultra-incompressible and superhard materials. Prog Mater Sci [Internet]. 2012;57(1):184–228. Available from: http://dx.doi.org/10.1016/j.pmatsci.2011.05.004

9. Stucker B, Bradley W, Eubank PT, Norasetthekul S, Bozkurt B. Zirconium diboride/copper EDM electrodes from selective laser sintering. Sol Free Fab Proc. 1997;1:257–66.

10. Stucker BE, Bradley WL. Rapid prototyping of zirconium diboride/copper electrical discharge machining electrodes [Internet]. Vol. 9800816. [Ann Arbor]: Texas A&M University; 1997. Available from: http://libproxy.mst.edu:2048/login?url=http://search.proquest.com/docview/304406135?accountid=14594

11. Freeman JW, Cross HC. NOTES ON HEAT-RESISTANT MATERIALS IN BRITAIN FROM TECHNICAL MISSION, OCTOBER 13, TO NOVEMBER 30, 1950. Michigan. Univ., Ann Arbor; Battelle Memorial Inst., Columbus, Ohio; 1951.

12. Mathauser EE. Materials for application to manned reentry vehicles. 1960;

13. Uher C. Thermal conductivity of metals. In: Thermal Conductivity. Springer; 2004. p. 21–91.

14. Chamberlain AL, Fahrenholtz WG, Hilmas GE. Reactive hot pressing of zirconium diboride. J Eur Ceram Soc. 2009;29(16):3401–8.

15. Lonergan JM, Fahrenholtz WG, Hilmas GE. Zirconium Diboride with High Thermal Conductivity. J Am Ceram Soc [Internet]. 2014;97(6):1689–91. Available from: http://dx.doi.org/10.1111/jace.12950

16. McClane DL, Fahrenholtz WG, Hilmas GE, Smith D. Thermal Properties of $(Zr,TM)B_2$ Solid Solutions with TM = Hf, Nb, W, Ti, and Y. J Am Ceram Soc. 2014;97(5):1552–8.

17. McClane DL, Fahrenholtz WG, Hilmas GE. Thermal Properties of $(Zr, TM)B_2$ Solid Solutions with TM = Ta, Mo, Re, V, and Cr. Smith D, editor. J Am Ceram Soc [Internet]. 2015 Feb [cited 2016 Jun 13];98(2):637–44. Available from: http://doi.wiley.com/10.1111/jace.13341

18. Mughabghab SF. Thermal neutron capture cross sections resonance integrals and g-factors. 2003;

19. Mishra B. Review of Extraction, Processing, Properties, and Applications of Reactive Metals: 1999 TMS Annual Meeting, San Diego, CA, February 28-March 15, 1999. John Wiley & Sons; 2013.

20. Backman L, Gild J, Luo J, Opila EJ. Part II: Experimental verification of computationally predicted preferential oxidation of refractory high entropy ultra-high temperature ceramics. Acta Mater [Internet]. 2020;197:81–90.

21. Gild J, Zhang Y, Harrington T, Jiang S, Hu T, Quinn MC, et al. High-Entropy Metal Diborides: A New Class of High-Entropy Materials and a New Type of Ultrahigh Temperature Ceramics. Sci Rep [Internet]. 2016;6.

22. Fahrenholtz Eric J.; Lee William E.; Zhou Yanchu WG. W. Ultra-High Temperature Ceramics: Materials for Extreme Environment Applications. The American Ceramic Society; 2014.

23. Tucker S, Moody H. The preparation of a new metal Boride. Proc Chem Soc L. 1901;17(238):129–30.

24. Pirani M, Alterthum H. Method for the determination of the melting point of metals which fuse at high temperatures. Z Elektrochem Angew Phys Chem. 1923;29:5–8.

25. Xu L, Xiao Y, van Sandwijk A, Xu Q, Yang Y. Production of nuclear grade zirconium: A review. J Nucl Mater [Internet]. 2015;466:21–8. Available from: http://www.sciencedirect.com/science/article/pii/S0022311515300969

26. Standard Specification for Zirconium Sponge and Other Forms of Virgin Metal for Nuclear Application.

27. Zelikman AN, Kreĭn OE, Samsonov GV. Metallurgy of rare metals. SNOVA; 2018.

28. Branken DJ, Lachmann G, Krieg HM, Bruinsma DSL. Influence of KF and HF on the Selectivity of Zr and Hf Separation by Fractional Crystallization of $K_2Zr(Hf)F_6$. Ind Eng Chem Res [Internet]. 2010 Jan 20;49(2):797–808. Available from: https://doi.org/10.1021/ie900747k

29. H. Nielsen R, H. Schlewitz J, Nielsen H, Staff U by. Zirconium and zirconium compounds. Kirk-Othmer Encycl Chem Technol. 2000;1–46.

30. Post B, Glaser FW, Moskowitz D. Transition metal diborides. Acta Metall [Internet]. 1954;2(1):20–5. Available from: http://www.sciencedirect.com/science/article/pii/0001616054900905

31. Gall D. Electron mean free path in elemental metals. J Appl Phys. 2016;119(8):85101.

32. Kaufman L, Clougherty E V. Boride compounds for very high temperature applications. Report RTD-TDR-63-4096, US Atomic Energy Commission, Washington, DC, USA; 1963.

33. Zhou Y, Wang J, Li Z, Zhan X, Wang J. First-Principles Investigation on the chemical bonding and intrinsic elastic properties of transition metal diborides TMB_2 (TM=Zr, Hf, Nb, Ta, and Y). In: Fahrenholtz WG, Wuchina EJ, William E L, Zhou Y, editors. Ultra-High Temperature Ceramics. 1st ed. Hoboken, New Jersey: John Wiley & Sons; 2014. p. 60–82.

34. Wang P, Kumar R, Sankaran EM, Qi X, Zhang X, Popov D, et al. Vanadium Diboride (VB_2) Synthesized at High Pressure: Elastic, Mechanical, Electronic, and Magnetic Properties and Thermal Stability. Inorg Chem [Internet]. 2018 Feb 5;57(3):1096–105. Available from: https://doi.org/10.1021/acs.inorgchem.7b02550

35. Shein IR, Ivanovskii AL. Elastic properties of mono-and polycrystalline hexagonal AlB2-like diborides of s, p and d metals from first-principles calculations. J Phys Condens Matter. 2008;20(41):415218.

36. Kingery WD, Bowen HK, Uhlmann DR (Donald R. Introduction to ceramics [Internet]. Wiley; 1976 [cited 2018 Nov 16]. 1032 p. Available from: https://books.google.com/books/about/Introduction_to_ceramics.html?id=Pd90vVkyTPcC

37. Carter CB, Norton MG. Ceramic materials : science and engineering. Second edition. New York: Springer; 2013. xxxiii, 766 pages.

38. Rahaman MN. Ceramic Processing. Taylor & Francis Group; 2007.

39. Herring C. Diffusional viscosity of a polycrystalline solid. J Appl Phys. 1950;21(5):437–45.

40. Mott NF, Nabarro FRN. Conference on strength of solids. In: Phys Soc, London. 1948. p. 1.

41. Kalish D, Clougherty E V. Densification mechanisms in high-pressure hot-pressing of HfB_2. J Am Ceram Soc. 1969;52(1):26–30.

42. Lonergan JM, Fahrenholtz WG. Thermophysical Properties of Reaction Processed Zirconium Diboride. Vol. Ph.D, Materials Science and Engineering. Missouri University of Science and Technology; 2014.

43. Akin I, Hotta M, Sahin FC, Yucel O, Goller G, Goto T. Microstructure and densification of ZrB_2–SiC composites prepared by spark plasma sintering. J Eur Ceram Soc [Internet]. 2009;29(11):2379–85. Available from: http://www.sciencedirect.com/science/article/pii/S0955221909000302

44. Coble RL. A model for boundary diffusion controlled creep in polycrystalline materials. J Appl Phys. 1963;34(6):1679–82.

45. Coble RL. Sintering crystalline solids. II. Experimental test of diffusion models in powder compacts. J Appl Phys. 1961;32(5):793–9.

46. Karthiselva NS, Kashyap S, Yadav D, Murty BS, Bakshi SR. Densification mechanisms during reactive spark plasma sintering of Titanium diboride and Zirconium diboride. Philos Mag. 2017;97(19):1588–609.

47. Lonergan JM, Fahrenholtz WG, Hilmas GE. Sintering Mechanisms and Kinetics for Reaction Hot-Pressed ZrB_2. J Am Ceram Soc [Internet]. 2015;98(8):2344–51. Available from: http://dx.doi.org/10.1111/jace.13544

48. Qiu H-Y, Guo W-M, Zou J, Zhang G-J. ZrB_2 powders prepared by boro/carbothermal reduction of ZrO_2: The effects of carbon source and reaction atmosphere. Powder Technol [Internet]. 2012;217:462–6. Available from: http://dx.doi.org/10.1016/j.powtec.2011.11.002

49. Sciti D, Silvestroni L, Medri V, Monteverde F. Sintering and densification mechanisms of ultra-high temperature ceramics. Ultra-High Temp Ceram Mater Extrem Environ Appl. 2014;112–43.

50. Guo S, Nishimura T, Kagawa Y. Preparation of zirconium diboride ceramics by reactive spark plasma sintering of zirconium hydride–boron powders. Scr Mater [Internet]. 2011;65(11):1018–21. Available from: http://www.sciencedirect.com/science/article/pii/S1359646211005331

51. Locci AM, Licheri R, Orrù R, Cao G. Reactive Spark Plasma Sintering of rhenium diboride. Ceram Int [Internet]. 2009;35(1):397–400. Available from: http://www.sciencedirect.com/science/article/pii/S0272884208000382

52. Venugopal S, Paul A, Vaidhyanathan B, Binner JGP, Heaton A, Brown PM. Synthesis and spark plasma sintering of sub-micron HfB_2: Effect of various carbon sources. J Eur Ceram Soc [Internet]. 2014;34(6):1471–9. Available from: http://www.sciencedirect.com/science/article/pii/S0955221913005980

53. Lee S-H, Feng L, Bae CJ. Densification of ZrB_2-SiC nanocomposites prepared using ZrSi2, B4C, and C additives. J Mater Res [Internet]. 2017;32(17):3302–8.

54. Grohsmeyer R, Hilmas G, Monteverde F, Fahrenholtz W. ZrB_2-$MoSi_2$ Ceramics with Varying $MoSi_2$ Content and ZrB_2 Powder Particle Size: Densification Process and Core-Shell Formation. 2017;

55. Kim J-S, Lee SJ, Feng L, Silvestroni L, Sciti D, Lee S-H. Effect of residual excess carbon on the densification of ultra-fine HfC powder. J Eur Ceram Soc [Internet]. 2020;40(5):1801–10.

56. Silvestroni L, Kleebe H-J, Lauterbach S, Müller M, Sciti D. Transmission electron microscopy on Zr- and Hf-borides with $MoSi_2$ addition: Densification mechanisms. J Mater Res [Internet]. 2010;25(05):828–34.

57. Guo W-M, Zhang G-J. Reaction Processes and Characterization of ZrB_2 Powder Prepared by Boro/Carbothermal Reduction of ZrO_2 in Vacuum. J Am Ceram Soc [Internet]. 2009;92(1):264–7.

58. Grimvall G. Thermophysical Properties of Materials. Amsterdam, Netherlands: Elsevier; 1999.

59. International A. Standard Test Method for Thermal Conductivity of Solids Using the Guarded-Comparative-Longitudinal Heat Flow Technique. Vol. ASTM E1225-13. WEst Conshohocken, PA: ASTM International; 2013.

60. International A. Standard Test Method for Thermal Conductivity of Refractories by Hot Wire (Platinum Resistance Thermometer Technique). Vol. ASTM C1113/C1113M-09. West Conshohocken, PA: ASTM International; 2019.

61. International A. Standard Test Method for Steady-State Thermal Transmission Properties by Means of the Heat Flow Meter Apparatus. Vol. ASTM C518-17. West Conshohocken, PA: ASTM Internarional; 2017.

62. Clougherty E V, Kalish D, Peters ET. Research and developement of refractory oxidation-resistant diboride. Wright Patterson Air Force Base; 1968.

63. Samsonov G V, Kovenskaya BA, Serebryakova TI, Tel'nikov EY. Thermal conductivity of diborides of group IV-VI transition metals. Institute of Problems in Materials Science, Academy of Sciences of the USSR; 1973.

64. Branscomb TM, Hunter Jr O. Improved Thermal Diffusivity Method Applied to TiB_2, ZrB_2, and HfB_2 from 200°–1300°C. J Appl Phys. 1971;42(6):2309–15.

65. Andrievskii RA, Korolev LA, Klimenko V V, Lanin AG, Spivak II, Taubin IL. Effect of zirconium carbide and carbon additions on some physicomechanical properties of zirconium diboride. Sov Powder Metall Met Ceram [Internet]. 1980;19(2):93–4. Available from: https://doi.org/10.1007/BF00792032

66. Fridlender BA, Neshpor VS, Ordan'yan SS, Unrod VI. Thermal conductivity and thermal diffusivity of binary alloys of the ZrC-ZrB_2 system at high temperatures. Teplofiz Vysok Temp. 1979;17(6):1210–5.

67. McClane DL, Fahrenholtz WG, Hilmas GE. Thermal Properties of $(Zr,TM)B_2$ Solid Solutions with TM = Hf, Nb, W, Ti, and Y. J Am Ceram Soc [Internet]. 2014. Available from: http://dx.doi.org/10.1111/jace.12893

68. Harrington G, Hilmas GE. Effect of Solid Solutions and Second Phases on the Thermal Conductivity of Zirconium Diboride Ceramics. Vol. Ph.D, Material Science and Engineering. University of Missouri Science and Technology; 2014.

69. Harrington GJK, Hilmas GE. Thermal Conductivity of ZrB_2 and HfB_2. In: Fahrenholtz WG, Wuchina EJ, Lee WE, Zhou Wy, editors. Ultra-High Temperature Ceramics: Materials for Extreme Environment Applications. 1st ed. Hoboken, New Jersey: John Wiley& Sons; 2014. p. 197–235.

70. Neuman EW, Hilmas GE, Fahrenholtz WG. Strength of Zirconium Diboride to 2300°C. J Am Ceram Soc [Internet]. 2013;96(1):47–50. Available from: http://dx.doi.org/10.1111/jace.12114

71. Chamberlain AL, Fahrenholtz WG, Hilmas GE. Pressureless Sintering of Zirconium Diboride. J Am Ceram Soc [Internet]. 2006;89(2):450–6. Available from: http://dx.doi.org/10.1111/j.1551-2916.2005.00739.x

72. McClane DL, Fahrenholtz WG, Hilmas GE, Smith D. Thermal Properties of (Zr, TM)B_2 Solid Solutions with TM = Ta, Mo, Re, V, and Cr. J Am Ceram Soc. 2015;98(2):637–44.

73. Sinnot MJ. The solid state for engineers Wiley. & Sons. New York. 1963;

74. Simon SH. The Oxford solid state basics. OUP Oxford; 2013.

75. Kittel C. Introduction to solid state physics. 8th ed. Hoboken, NJ: Wiley; 2005. xix, 680 p.

76. Lawson JW, Daw MS, Bauschlicher Jr CW. Lattice thermal conductivity of ultra high temperature ceramics ZrB2 and HfB2 from atomistic simulations. J Appl Phys. 2011;110(8):83507.

77. Lee DW, Kingery WD. Radiation Energy Transfer and Thermal Conductivity of Ceramic Oxides. J Am Ceram Soc [Internet]. 1960;43(11):594–607. Available from: http://dx.doi.org/10.1111/j.1151-2916.1960.tb13623.x

78. Sindeband SJ, Schwarzkopf P. The metallic nature of metal borides. Powder Metall Bull. 1950;5(3):42–3.

79. Zimmermann JW, Hilmas GE, Fahrenholtz WG, Dinwiddie RB, Porter WD, Wang H. Thermophysical Properties of ZrB_2 and ZrB_2–SiC Ceramics. J Am Ceram Soc [Internet]. 2008;91(5):1405–11. Available from: http://dx.doi.org/10.1111/j.1551-2916.2008.02268.x

80. Zhang L, Pejaković DA, Marschall J, Gasch M. Thermal and Electrical Transport Properties of Spark Plasma-Sintered HfB_2 and ZrB_2 Ceramics. J Am Ceram Soc. 2011;94(8):2562–70.

81. Thompson MJ, Fahrenholtz WG, Hilmas GE, padture N. Elevated Temperature Thermal Properties of ZrB2 with Carbon Additions. J Am Ceram Soc. 2012;95(3):1077–85.

82. Thompson MJ. Densification and Thermal Properties of Zirconium Diboride Based Ceramics. Missouri University of Science and Technology; 2012.

83. Neel DS, Pears CD, Oglesby JR. The Thermal Properties of Thirteen Solid Materials to 5000 Degrees F for their Destruction Tempaeratures. Souther Research Inst Birmingham, AL, United States; 1962.

84. International A. Standard Test Method for Thermal Diffusivity by the Flash Method. Vol. ASTM E1461-13. West Conshohocken, PA: ASTM International; 2013.

85. Thompson MJ, Fahrenholtz WG, Hilmas GE. Elevated Temperature Thermal Properties of ZrB_2 with Carbon Additions. J Am Ceram Soc [Internet]. 2012;95(3):1077–85. Available from: http://dx.doi.org/10.1111/j.1551-2916.2011.05034.x

86. McClane DL, Fahrenholtz WG, Hilmas GE. Thermal properties of $(Zr,TM)B_2$ solid solutions with TM = Hf, Nb, W, Ti, and y. J Am Ceram Soc. 2014;97(5):1552–8.

87. Zhang Y, Stocks GM, Jin K, Lu C, Bei H, Sales BC, et al. Influence of chemical disorder on energy dissipation and defect evolution in concentrated solid solution alloys. Nat Commun. 2015;6.

88. Butler TM, Chaput KJ, Dietrich JR, Senkov ON. High temperature oxidation behaviors of equimolar NbTiZrV and NbTiZrCr refractory complex concentrated alloys (RCCAs). J Alloys Compd. 2017;729:1004–19.

89. Müller F, Gorr B, Christ H-J, Müller J, Butz B, Chen H, et al. On the oxidation mechanism of refractory high entropy alloys. Corros Sci. 2019;159.

90. Dai F-Z, Sun Y, Wen B, Xiang H, Zhou Y. Temperature Dependent Thermal and Elastic Properties of High Entropy $(Ti_{0.2}Zr_{0.2}Hf_{0.2}Nb_{0.2}Ta_{0.2})B_2$: Molecular Dynamics Simulation by Deep Learning Potential. J Mater Sci Technol [Internet]. 2021;72:8–15. Available from: https://www.scopus.com/inward/record.uri?eid=2-s2.0-85092074105&doi=10.1016%2Fj.jmst.2020.07.014&partnerID=40&md5=8bc704aa9a46404f25777e643658a69d

91. Gild J, Wright A, Quiambao-Tomko K, Qin M, Tomko JA, Shafkat bin Hoque M, et al. Thermal conductivity and hardness of three single-phase high-entropy metal diborides fabricated by borocarbothermal reduction and spark plasma sintering. Ceram Int. 2020;46(5):6906–13.

92. Liu J-X, Shen X-Q, Wu Y, Li F, Liang Y, Zhang G-J. Mechanical properties of hot-pressed high-entropy diboride-based ceramics. J Adv Ceram. 2020;9(4):503–10.

93. Chen H, Xiang H, Dai F-Z, Liu J, Zhou Y. Porous high entropy $(Zr_{0.2}Hf_{0.2}Ti_{0.2}Nb_{0.2}Ta_{0.2})B_2$: A novel strategy towards making ultrahigh temperature ceramics thermal insulating. J Mater Sci Technol. 2019;35(10):2404–8.

94. Rost CM, Sachet E, Borman T, Moballegh A, Dickey EC, Hou D, et al. Entropy-stabilized oxides. Nat Commun [Internet]. 2015;6. Available from: https://www.scopus.com/inward/record.uri?eid=2-s2.0-84942894980&doi=10.1038%2Fncomms9485&partnerID=40&md5=08474f5f1d2352ac18010927d3e222ba

95. Dorner AN, Barton DJ, Zhou Y, Thompson GB, Hilmas GE, Fahrenholtz WG. Solute distributions in tantalum-containing zirconium diboride ceramics. J Am Ceram Soc. 2020;103(4):2880–90.

96. Tsai M-H, Yeh J-W. High-entropy alloys: a critical review. Mater Res Lett. 2014;2(3):107–23.

97. Zhang Y, Zuo TT, Tang Z, Gao MC, Dahmen KA, Liaw PK, et al. Microstructures and properties of high-entropy alloys. Prog Mater Sci. 2014;61:1–93.

98. Chou H-P, Chang Y-S, Chen S-K, Yeh J-W. Microstructure, thermophysical and electrical properties in $Al_xCoCrFeNi$ ($0\leq x\leq 2$) high-entropy alloys. Mater Sci Eng B. 2009;163(3):184–9.

99. Feng L, Fahrenholtz WG, Hilmas GE, Zhou Y. Synthesis of single-phase high-entropy carbide powders. Scr Mater [Internet]. 2019;162:90–3. Available from: https://www.scopus.com/inward/record.uri?eid=2-s2.0-85056208567&doi=10.1016%2Fj.scriptamat.2018.10.049&partnerID=40&md5=fbf40c03a78a8f42bdc26507299f9b1a

100. Jiang S, Hu T, Gild J, Zhou N, Nie J, Qin M, et al. A new class of high-entropy perovskite oxides. Scr Mater [Internet]. 2018;142:116–20. Available from: https://www.scopus.com/inward/record.uri?eid=2-s2.0-85028717255&doi=10.1016%2Fj.scriptamat.2017.08.040&partnerID=40&md5=570c9cb8dfe39b8df0ba40020998dcc1

101. Jones NG, Aveson JW, Bhowmik A, Conduit BD, Stone HJ. On the entropic stabilisation of an Al0. 5CrFeCoNiCu high entropy alloy. Intermetallics. 2014;54:148–53.

102. Otto F, Yang Y, Bei H, George EP. Relative effects of enthalpy and entropy on the phase stability of equiatomic high-entropy alloys. Acta Mater. 2013;61(7):2628–38.

103. Wu Z, Bei H, Otto F, Pharr GM, George EP. Recovery, recrystallization, grain growth and phase stability of a family of FCC-structured multi-component equiatomic solid solution alloys. Intermetallics. 2014;46:131–40.

104. Zhang F, Zhang C, Chen S-L, Zhu J, Cao W-S, Kattner UR. An understanding of high entropy alloys from phase diagram calculations. Calphad. 2014;45:1–10.

105. Hume-Rothery W. Atomic diameters, atomic volumes and solid solubility relations in alloys. Acta Metall [Internet]. 1966;14(1):17–20. Available from: http://www.sciencedirect.com/science/article/pii/0001616066902677

106. Hume-Rothery W, Coles BR. The transition metals and their alloys. Adv Phys [Internet]. 1954;3(10):149–242. Available from: https://www.scopus.com/inward/record.uri?eid=2-s2.0-84913498572&doi=10.1080%2F00018735400101193&partnerID=40&md5=b331627dd50da01e486188c672e3b876

107. Pauling L. Atomic Radii and Interatomic Distances in Metals. J Am Chem Soc [Internet]. 1947;69(3):542–53. Available from: http://dx.doi.org/10.1021/ja01195a024

108. Vegard L. Die Konstitution der Mischkristalle und die Raumfüllung der Atome. Zeitschrift für Phys [Internet]. 1921;5(1):17–26. Available from: https://www.scopus.com/inward/record.uri?eid=2-s2.0-27844583800&doi=10.1007%2FBF01349680&partnerID=40&md5=0b0a662356a19a7ee299cba4b1a79def

109. Jacob KT, Raj S, Rannesh L. Vegard's law: A fundamental relation or an approximation? Int J Mater Res [Internet]. 2007;98(9):776–9. Available from: https://www.scopus.com/inward/record.uri?eid=2-s2.0-35348859472&doi=10.3139%2F146.101545&partnerID=40&md5=2ef6e4b0ecb0c078453c8c49e46e4c35

110. Zhang Y, Jiang Z-B, Sun S-K, Guo W-M, Chen Q-S, Qiu J-X, et al. Microstructure and mechanical properties of high-entropy borides derived from boro/carbothermal reduction. J Eur Ceram Soc [Internet]. 2019;39(13):3920–4. Available from: https://www.scopus.com/inward/record.uri?eid=2-s2.0-85066263397&doi=10.1016%2Fj.jeurceramsoc.2019.05.017&partnerID=40&md5=745cd50421de2963905eb48271f70424

111. Qin M, Gild J, Hu C, Wang H, Hoque MSB, Braun JL, et al. Dual-phase high-entropy ultra-high temperature ceramics. J Eur Ceram Soc [Internet]. 2020;40(15):5037–50. Available from: https://www.scopus.com/inward/record.uri?eid=2-s2.0-85087117104&doi=10.1016%2Fj.jeurceramsoc.2020.05.040&partnerID=40&md5=30ca09b579c3d2ab5329bc866b06028b

112. Feng L, Fahrenholtz WG, Hilmas GE. Processing of dense high-entropy boride ceramics. J Eur Ceram Soc [Internet]. 2020;40(12):3815–23. Available from: https://www.scopus.com/inward/record.uri?eid=2-s2.0-85083487184&doi=10.1016%2Fj.jeurceramsoc.2020.03.065&partnerID=40&md5=3463aab35f58502980c3f5cb75e4df6e

113. Monteverde F, Saraga F, Gaboardi M. Compositional disorder and sintering of entropy stabilized (Hf,Nb,Ta,Ti,Zr)B_2 solid solution powders. J Eur Ceram Soc [Internet]. 2020;40(12):3807–14. Available from: https://www.scopus.com/inward/record.uri?eid=2-s2.0-85083831513&doi=10.1016%2Fj.jeurceramsoc.2020.04.026&partnerID=40&md5=5395ac4fc23592c15525409f4443c98a

114. Feng L, Fahrenholtz WG, Hilmas GE. Two-step synthesis process for high-entropy diboride powders. J Am Ceram Soc [Internet]. 2020;103(2):724–30. Available from: https://www.scopus.com/inward/record.uri?eid=2-s2.0-85073917803&doi=10.1111%2Fjace.16801&partnerID=40&md5=7500fdb91aa8d4d4d604a5d6611d1a7b

115. Barbarossa S, Orrù R, Garroni S, Licheri R, Cao G. Ultra high temperature high-entropy borides: Effect of graphite addition on oxides removal and densification behaviour. Ceram Int [Internet]. 2020; Available from: https://www.scopus.com/inward/record.uri?eid=2-s2.0-85094587842&doi=10.1016%2Fj.ceramint.2020.10.200&partnerID=40&md5=c158ecf45ccf628db5dcbdf0d82959cb

116. Tallarita G, Licheri R, Garroni S, Orrù R, Cao G. Novel processing route for the fabrication of bulk high-entropy metal diborides. Scr Mater [Internet]. 2019;158:100–4. Available from: https://www.scopus.com/inward/record.uri?eid=2-s2.0-85052640241&doi=10.1016%2Fj.scriptamat.2018.08.039&partnerID=40&md5=c7f540d6200c149736c58aab27f5a0cd

117. Zhang Y, Guo W-M, Jiang Z-B, Zhu Q-Q, Sun S-K, You Y, et al. Dense high-entropy boride ceramics with ultra-high hardness. Scr Mater. 2019;164:135–9.

118. Feng L, Fahrenholtz WG, Hilmas GE, Monteverde F. Effect of Nb content on the phase composition, densification, microstructure, and mechanical properties of high-entropy boride ceramics. J Eur Ceram Soc [Internet]. 2020;

119. Qin M, Gild J, Wang H, Harrington T, Vecchio KS, Luo J. Dissolving and stabilizing soft WB_2 and MoB_2 phases into high-entropy borides via boron-metals reactive sintering to attain higher hardness. J Eur Ceram Soc [Internet]. 2020;40(12):4348–53. Available from: http://www.sciencedirect.com/science/article/pii/S0955221920302442

120. Gu J, Zou J, Sun S-K, Wang H, Yu S-Y, Zhang J, et al. Dense and pure high-entropy metal diboride ceramics sintered from self-synthesized powders via boro/carbothermal reduction approach. Sci China Mater. 2019;62(12):1898–909.

121. Neuman EW, Fahrenholtz WG, Hilmas GE. Microstructure and mechanical properties of reaction-hot-pressed zirconium diboride based ceramics. Int J Appl Ceram Technol [Internet]. 2019;16(5):1715–22.

122. Senkov ON, Senkova S V, Woodward C, Miracle DB. Low-density, refractory multi-principal element alloys of the Cr–Nb–Ti–V–Zr system: Microstructure and phase analysis. Acta Mater. 2013;61(5):1545–57.

123. Stanfield AD, Hilmas GE, Fahrenholtz WG. Effects of Ti, Y, and Hf additions on the thermal properties of ZrB_2. J Eur Ceram Soc [Internet]. 2020; Available from: https://www.scopus.com/inward/record.uri?eid=2-s2.0-85085092015&doi=10.1016%2Fj.jeurceramsoc.2020.04.011&partnerID=40&md5=0312c793c57d6e7402a378ed3cc49c81

124. Chamberlain AL, Fahrenholtz WG, Hilmas GE. Reactive hot pressing of zirconium diboride. J Eur Ceram Soc. 2009;29(16):3401–8.

125. Zhu S, Fahrenholtz WG, Hilmas GE, Zhang SC. Pressureless sintering of carbon-coated zirconium diboride powders. Mater Sci Eng A [Internet]. 2007;459(1–2):167–71. Available from: http://www.sciencedirect.com/science/article/pii/S0921509307004480

126. Zhang X, Hilmas GE, Fahrenholtz WG. Synthesis, densification, and mechanical properties of TaB_2. Mater Lett [Internet]. 2008;62(27):4251–3.

127. Jackson HF, Jayaseelan DD, Lee WE, Reece MJ, Inam F, Manara D. Laser melting of spark plasma-sintered zirconium carbide: thermophysical properties of a generation IV very high temperature reactor material. Int J Appl Ceram Technol. 2010; 7(3): 316–326.

128. Manara D, Böhler R, Boboridis K, Capriotti L, Quaini A, Luzzi L, et al. The melting behaviour of oxide nuclear fuels: effects of the oxygen potential studied by laser heating. Procedia Chem. 2012;7:505–12.

129. Nunez UC, Prieur D, Bohler R, Manara D. Melting point determination of uranium nitride and uranium plutonium nitride: A laser heating study. J Nucl Mater. 2014;449(1–3):1–8.

130. Cedillos-Barraza O, Grasso S, Al Nasiri N, Jayaseelan DD, Reece MJ, Lee WE. Sintering behaviour, solid solution formation and characterisation of TaC, HfC and TaC–HfC fabricated by spark plasma sintering. J Eur Ceram Soc. 2016;36(7):1539–48.

131. Norton JT, Blumenthal H, Sindeband SJ. Structure of diborides of titanium, zirconium, columbium, tantalum and vanadium. JOM. 1949;1(10):749–51.

132. Wong-Ng W, McMurdie HF, Paretzkin B, Zhang Y, Hubbard CR, Dragoo AL, et al. Standard x-ray diffraction powder patterns of fifteen ceramic phases. Powder Diffr. 1988;3(1):47–56.

VITA

Austin David Stanfield was born and raised in Kansas City, Missouri. Growing up and through high school he participated and competed in a wide range of extracurricular activities including ballet, horseback riding and cross country, but was especially active in the Boy Scouts of America, eventually serving as a Ranger at Philmont Scout Ranch for a summer.

After graduating from Rockhurst High School, Austin pursued a degree in Ceramic Engineering at the Missouri University of Science and Technology. During his time there he was active in his fraternity, Sigma Tau Gamma, ultimately serving as President. Austin was active in the campus community and served on the executive board of several student organizations including the Interfraternity Council, Keramos, and Material Advantage. He also held an undergraduate research assistant position with the glass research group.

Upon graduating with his Bachelor's degree, Austin was invited to pursue a Ph.D. in the ultra-high temperature ceramics group by Dr. Bill Fahrenholtz and Dr. Greg Hilmas at Missouri S&T. There his work focused on the thermophysical properties nominally phase pure diboride ceramics. Upon completion of his degree, Austin had eleven conference presentations, two papers published, and two papers submitted for publication.

In May 2021 he received his Ph.D. in Materials Science and Engineering from Missouri University of Science and Technology.